UNIVERSITE JOSEPH KI-ZERBO

ECOLE DOCTORALE INFORMATIQUE ET CHANGEMENTS CLIMATIQUES

BURKINA FASO

Unité-Progrès-Justic

MASTER RESEARCH PROGRAM

SPECIALITY: INFORMATICS FOR CLIMATE CHANGE (ICC)

MASTER THESIS

Subject:

ARTIFICIAL INTELLIGENCE-BASED SPATIOTEMPORAL ASSESSMENT OF HISTORICAL AND FUTURE SHORELINE DYNAMICS: Case study of Benin Republic

Presented on July, 12th 2022 by:

Codjo David DEGBEY

Jury members:

President: Dr Lassane YAMEOGO

Reviewer: Dr Benewende ZOUNGRANA

Supervisor: Dr Kwame HACKMAN

Major Supervisor:

Prof. Julien ADOUNKPE

Co-Supervisor:

Dr. Kwame O. HACKMAN

Academic year 2021-2022

Dedication

- ✓ To GOD, the Almighty, the omniscient, the omnipresent and the omnipotent.

- ✓ To my father Léon K. DEGBEY, who supports and inspires me during all my cursus. Thank you for all the sacrifices; may GOD bless you.

- ✓ To my mother Ruth T. BEMOU, my first fan, whose prayers, supports and encouragements bring me daily motivation for my work. All my gratitude and may GOD bless you a hundredfold.

Epigraph

"We see incredible opportunity to solve some of the biggest social challenges we have by combining high-performance computing and **Artificial Intelligence** – such as **Climate Change** and more."

Lisa Su, CEO of Advanced Micro Devices.

Acknowledgements

My deep and warm thanks go towards the German Federal Ministry of Education and Research (BMBF) for funding this program, and to the West African Science Service Center on Climate Change and Adapted Land use (WASCAL) for giving me this scholarship opportunity to complete my Master thesis in Informatics for Climate Change.

I would like to extend also my profound gratitude to all the Management and Staff of WASCAL Graduate Study Program (GSP) Burkina Faso, for their hospitality, guidance, and kindness. Special thanks to Prof. Tanga Pierre ZOUNGRANA, Director of "Ecole Doctorale Informatique et Changement Climatique" (ED-ICC) for his wise counsels, to Dr Ousmane COULIBALY, Deputy Director of ED-ICC, for his endless efforts and his noticeable contribution to our academic performance, to Dr Jean Bosco Benewende ZOUNGRANA, the Scientific Coordinator of ED-ICC, for his meticulous scientific guidance.

I am particularly grateful to my supervisors; my Major Supervisor Prof. Julien ADOUNKPE, Director of WASCAL GSP Benin, for his monitoring and mentorship all along this work; my Co-supervisor Dr Kwame Oppong HACKMAN, Responsible of the GIS and Remote Sensing Lab in WASCAL Competence Center (CoC), for scrutinizing my work daily and for constantly bringing both critical and constructive feedback.

My profound acknowledgements to Prof. Kehinde OGUNDJOBI, Director of the CoC for his warm welcome in the institution he runs, all my lecturers during this program for the quality of their lectures, especially Prof. Boniface K. ALESE, Prof. Harouna NAROUA, Dr Belko A. DIALLO, Dr Ulrich DIASSO and Dr Seyni SALACK.

I would like to thank specifically Dr Felicien CHEDE, Director of the National Meteorology Agency of Benin, and all my colleagues in the Agency, for allowing me to serenely pursue my Master thesis out of the country.

I also want to thank Prof. Ernest AMOUSSOU, Dr Georges DEGBE, Dr Frédéric BONOU, Dr Emile EDEA and Dr Charles HOUNTON, for bringing their scientific knowledge to improve the quality of this work despite the fact that I contacted them late.

My thanks also go out to all my west African fellow students (in my program) and other interns in CoC for being available, and maintaining a friendly work environment during all my internship. May GOD bless all of you.

Abstract

Global Sea Level Rise (SLR), especially caused by global warming, highly threatens the coastal countries by causing coastal erosions, biodiversity loss, coastal flooding, etc. The study of shoreline dynamics is a key aspect of coastal area management, and is useful for reducing risk and vulnerability to climate change within coastal ecosystems. Artificial Intelligence (AI) is an efficient approach to this type of problem because of its advanced multidimensional data extraction and computational tools. This study uses AI methodologies combined with Remote Sensing (RS) and Geographic Information Systems (GIS) tools to perform a spatiotemporal analysis of the shoreline dynamics of the Republic of Benin from 2001 to 2021. Preprocessed multispectral and multitemporal Landsat 5, 7 and 8 surface reflectance images as well as the NASA Shuttle Radar Topography Mission (SRTM) digital elevation data were extracted from the Data Catalog of Google Earth Engine (GEE). Then, the cloud computing platform of GEE was used to perform binary (Sea Water / Non-Sea Water) supervised image classification. The Machine Learning algorithms used were Support Vector Machines (SVM) and Random Forest (RF). QGIS was used to extract historical shorelines from the respective classified images in 5-year intervals. Net Shoreline Movement (NSM), End Point Rate (EPR), Linear Regression Rate (LRR) and Weighted Linear regression Rate (WLR) were the shoreline change statistics derived from Digital Shoreline Analysis System (DSAS), a plugin of ArcGIS. Then, the Kalman Filter model, implemented in the DSAS plugin, was used to provide a "beta" forecast of the shoreline shape respectively for the years 2031 and 2041, with a confidence interval of 90%. A geostatistical analysis of the results mainly showed, for the study period, a clear coastal erosion trend at average rates of -2.17 ± 0.28 m (EPR), -1.51 ± 1.68 m (LRR). A sectorial and deeper analysis revealed that, in terms of NSM, the West side of the Port infrastructure underwent more accretion (41.67% against 25.71% at the East) while the East side experienced more erosion (74.29% against 58.33% at the West). Assuming a Business-as-Usual (BaU) scenario, the projected highest erosion values were found to be -226.42 m (2031) and -146.14 m (2041) in the locality of Avloh plage (Grand-Popo), -68.11 m (2031) and -182.55 m (2041) in the locality of Hillacondji (Grand-Popo), -146.14 m (2031) and -307.30 m (2041) in the locality of Agblangandan (Cotonou). Finally, a web application was designed and implemented to facilitate an easy data access and visualization of results by non-experts and decision makers.

Key words: Erosion; Machine Learning; Shoreline; Remote Sensing; Kalman Filter; Benin.

Acronyms and Abbreviations

ANN: Artificial Neural Network

AR: Assessment Report

AWEInsh: Automated Water Extraction Index non-shadow

BaU: Business-as-Usual

CBD: Color Band Divergence

DEM: Digital Elevation Map

EPR: End Point Rate

EWS: Early Warning System

GDP: Gross Domestic Product

GEE: Google Earth Engine

GIZC: Gestion intégrée de la Zone Côtière

GMSL: Global Mean Sea Level

ICC: Informatics for Climate Change

INSAE: Institut National de la Statistique et de l'Analyse Economique

IPCC: Intergovernmental Panel on Climate Change

IR: Infra Red

ITCZ: Inter Tropical Convergence Zone

LIDAR: Laser Imaging Detection And Ranging

LRR: Linear Regression Rate

ML: Machine Learning

NASA: National Aeronautics and Space Administration

NDBI: Normalized Difference Built-up Index

NDVI: Normalized Difference Vegetation Index

NDWI: Normalized Difference Water Index

NOAA: National Oceanic and Atmospheric Administration

PAC: Port Autonome de Cotonou

RCP: Representative Concentration Pathways

RF: Random Forest

RGB: Red Green Blue

RMSE: Root Mean Square Error

SDG: Sustainable Development Goal

SLR: Sea Level Rise

SRTM: Shuttle Radar Topography Mission

SVM: Support Vector Machines

USA: United States of America

USGS: USA Geological Survey Group

UV: Ultra Violet

WLR: Weighted Linear regression Rate

List of tables

List of figures

Introduction

Climate change – the change in the state of the climate that can be identified (e.g., by using statistical tests) by changes in the mean and/or the variability of its properties and that persists for an extended period, typically decades or longer (IPCC, 2018) – is one of the major planetary threats identified in the 21st century. There are many ways to characterize this phenomenon. Global warming, the most known characterization of climate change, is due to the increase of the concentration of atmospheric Green House Gases (GHG), mainly driven by anthropogenic forces. Global warming results in phenomena such as ocean warming, land ice melting, increase of climate extreme events occurrences, etc. Both ocean warming and land ice melting combined, result in Sea Level Rise (SLR) (Cazenave & Le Cozannet, 2013). SLR occurs in two (02) ways: thermal expansion that causes water to expand as it warms (Church, 2001), and land ice melting that causes to the retreat of glacier and thinning of ice at the poles (McGuire, 2017). This dilatation of the water induced by the rise in its temperature, is one of the major drivers of the coastal erosion (Leatherman et al., 2000). Concretely, climate change was reported to accelerate the global SLR at a rate of 0.084 ± 0.025 mm / year within the 25 years preceding 2017 (Nerem et al., 2018). Researchers have projected that half of the global sandy beaches are likely to disappear by the end of the 21st century (Vousdoukas et al., 2020). Indeed, as the most settled parts of the world, coastal zones frequently experience hazards directly or indirectly linked to SLR. As a result, there is an increase in the frequency of occurrences of coastal disasters such as floods, erosion, cyclones, typhoons, tsunamis, etc. African coasts are not exempted from these phenomena.

According to Croitoru et al. (2019), coastal zone degradation in Benin Republic, Cote d'Ivoire, Senegal and Togo, costs USD 3.8 billion / year, an equivalent of 5.3% of their Gross Domestic Product (GDP). It is estimated that approximately 500,000 people are affected annually by the impact of flooding and coastal erosion in West Africa (World Bank, 2022). Thus, Benin Republic subject to these coastal hazards, has been experiencing shoreline spatiotemporal fluctuation under the influence of climate change during the last decades (Degbe, 2017). For a better management of Benin Republic's coastal areas, there is the need to monitor the shoreline dynamics and to forecast its future behavior. The current study aims to help in the management of climate change impacts on Benin Republic coastal areas. This will be done by using Artificial Intelligence (AI) tools to assess and predict shoreline dynamics. The study is articulated around 3 main points. First, the spatiotemporal shoreline dynamics of Benin

Republic from 2001 to 2021 will be evaluated in terms of magnitude and direction. Second, assuming a Business-as-Usual (BaU) scenario, an AI-based prediction model will be used to forecast the next shoreline shape, for 10 and then 20 years. Third, a web application was built to show the different results, in order to improve decision making.

Problem statement

At the state of the art, there is actually no open access African historical shoreline data portal as in the case of the USA with the USA Geological Survey Group **(**USGS) Coastal Change Hazards Portal and National Oceanic and Atmospheric Administration (NOOA) Digital Coast**.** This is due to the lack of data in this region of the planet. The existing data sources are private raw satellite images database and usually not for free. These images are not processed to the level of a shoreline data portal.

Additionally, few authors integrated up to 6 additional computed bands to perform binary (Sea water / Non - Sea water) image classification (Abdelhady et al., 2022; Alicandro et al., 2019, Casse et al., 2012). Most of them limited the work to maximum 02 computed bands additionally to the raw ones (Toure et al., 2019).

In the literature, Remote Sensing (RS) and AI-based historical shoreline spatiotemporal change assessment is also poorly documented, especially in Africa. Many authors worked on shoreline change assessment but most of them manually digitized the shorelines and the baseline for the work. In other cases, they used semi-automatic embed Geographic Information System (GIS) classification tools (Assogba, 2018; Degbe, 2017). This kind of methodology highly affect negatively the accuracy of the binary classification, and thus, the final change rates accuracy.

To fill up the previous highlighted gaps, a methodology was proposed in this study to reconstitute the historical changes of shoreline over Benin Republic coast since 2001, and to attempt its horizon 2031-2041 forecast, using high resolution RS images and AI approach.

Research questions

In the scope of this study, the main research question that will be addressed is: How has the Benin Republic shoreline shape changed over the last 20 years in terms of magnitude and rate? From this major research question, it can be derived the following specific ones:

- **Specific Research Question 1:** What is the general trend in the evolution of Benin Republic shoreline dynamics during the past 20 years?

- **Specific Research Question 2**: Assuming a Business-as-Usual scenario, what will be the shoreline shape at horizons 2031 and 2041?
- **Specific research question 3**: How to better communicate historical and forecast shoreline positions to non-expert targets?

Research hypotheses

The main hypothesis related to the main research question is that: Over the last 20 years, Benin Republic shoreline has undergone complex dynamics. Regarding the three (03) previous specific research questions, here are the specific hypotheses to be confirmed:

- **Specific Research Hypothesis 1**: During the last 20 years, Benin Republic shoreline has undergone significant variations in terms of magnitude and direction.
- **Specific Research Hypothesis 2**: Assuming a Business as Usual scenario, Benin Republic shoreline projected at horizons 2031 and 2041, is such a way that there is erosion in some places and accretion in other.
- **Specific Research Hypothesis 3**: Historical and forecast shoreline positions in Benin Republic, can be communicated to non-expert targets via an open-access web application.

Research objectives

Our main objective in this study, is to analyze historical and projected shoreline dynamics along Benin Republic coast over the years**.** This objective can be broken down into the 3 following specific objectives corresponding to each research question:

- **Specific research objective 1**: Evaluate Benin Republic shoreline dynamics over the last 20 years.
- **Specific research objective 2**: Forecast Benin Republic shoreline position at horizon 2031 and horizon 2041, assuming a Business as Usual scenario.
- **Specific research objective 3**: Build a web application to communicate historical and forecasted shoreline positions in Benin Republic to non-experts.

Chapter 1: Literature review

In this chapter, an overview of the concepts and taxonomy used in this thesis, has been described. This chapter starts with a section about concepts and generalities on shoreline, proceeds with an overview of AI and RS and ends with the state of the art concerning the topic of this study.

1.1. Shoreline Concepts

1.1.1. Generalities and data sources overview

Ideally, shoreline is the imaginary line that coincides with the physical interface of land and water (Dolan et al., 1980). In spite of this simple definition, in practice it is a challenge to clearly identify this line. In reality, the shoreline position is in continuous change over the time, because of cross-shore and alongshore sediment movement in the littoral zone and especially because of the dynamic nature of water levels at the coastal boundary (e.g., waves, tides, groundwater, storm surge, setup, runup, etc.) (Boak & Turner, 2005). There are many data sources for shorelines. The main ones are: Historical Land-Based Photographs, Coastal Maps and Charts, and Remote Sensing (RS). Since RS is the data source used in this study, its main types were highlighted:

1.1.1.1. Multispectral/Hyperspectral Imaging

Satellites now provide near-continuous monitoring of many of the world's shorelines (Morton, 1991). Traditional multispectral satellite-flown instruments, such as Landsat, SPOT, etc., generate a discrete signal in a limited number of broadbands (Cracknell, 1999). Hyperspectral imaging provides wide and continuous spectral coverage (Richards & Jia, 1999). The advantages of multispectral/hyperspectral imagery are the large areas that can be covered and the detailed spectral information provided. Shorelines may be derived from visibly discernible coastal features (using true- or false-color imagery) or by the application of digital image-processing techniques. This data source is the one used in the scope of the present study.

1.1.1.2. Microwave Sensors and Video Imaging

Data from the microwave range of wavelengths can be collected using airborne side-looking airborne radar or spaceborne synthetic aperture radar (Cracknell, 1999). Information about the point on the ground is calculated based on the return period of the signal and signal strength (Richards & Jia, 1999). Large spatial areas can be covered using radar technology, but the cost is high (Richards & Jia, 1999).

The advent of digital imaging technology has enabled higher-frequency and continuous images of the coast to be collected in the visible wavelengths. These systems have the capability to monitor detailed changes in the coastal system, as well as providing long-term shoreline change information (at a given time).

1.1.2. Shoreline indicators overview

Because of the dynamic nature of the idealized shoreline boundary, for practical purposes coastal investigators have typically adopted the use of shoreline indicators. A shoreline indicator is a feature that is used as a proxy to represent the ‘‘exact’’ shoreline position. Individual shoreline indicators generally fall into one of two categories. Classifications in the first group are based on a visually discernible coastal feature, whereas classifications in the second group are based on a specific tidal datum. The most common shoreline indicators used have been reported by Boak & Turner (2005). Among these indicators, the chosen one for this study, is the Color Band Divergence (CBD) shoreline**.** Used by Aarninkhof (2003), it differentiates pixels based on the reflectance properties of ‘‘wet’’ and ‘‘dry’’ regions based on a divergence of the relative intensity in the Red Green Blue (RGB) spectrum. Its advantages are that it determines an objective shoreline, repeatable (scientifically valid) and automated (Boak & Turner, 2005).

1.1.3. Shoreline detection techniques

To each shoreline detection technique, commonly two steps are required to identify a shoreline. The first is to select and define a shoreline indicator as a proxy for the land-water interface. The second step of shoreline identification involves the detection of the chosen shoreline indicator within the available data source (Boak & Turner, 2005). Both steps 1 and 2 can induce errors (Stockdon et al., 2002). All of the shoreline detection techniques depend on the chosen data sources. An overview of the main techniques is provided below.

1.1.3.1. Aerial photography, LIDAR aerial beach surveys and video imaging

Today, drones are most commonly used for this purpose. Software is available for georectification of the images and extraction of the shoreline. Digital Elevation Maps (DEMs) of the beach can be obtained by airborne Laser Imaging Detection And Ranging (LIDAR) at low water. High costs are an impediment for frequent surveys. The video cameras are installed at a fixed location at sufficient height for covering a coastal stretch of up to 2 km length. Argus video monitoring technique enables the detection of shoreline evolution and beach width, erosional and accretional sediment volumes of the intertidal beach, subtidal beach bathymetry

and wave run-up (Holman et al., 1993).

1.1.3.2. Satellite images

Publicly available optical satellite images have a progressive increasing resolution and decreasing revisit period which make them suitable for shoreline detection. A refined version of the sub-pixel resolution shoreline detection technique has been developed by Liu et al. (2017) and later augmented with the addition of an image classification component to refine the detection of the sand/water interface. In this way the horizontal Root Mean Square Error (RMSE) can be reduced to less than about 10 m. Satellite images constitute the chosen detection technique in this study. That is why it is important to have an overview of RS and AI for the image classification component stated a few lines above.

1.1.4. Shoreline prediction methods

Modeling shoreline position, shape and geomorphology is quiet challenging because of the numerous complex drivers needed to consider (waves, tides, wind, water heights, etc.). This is why, there are not too many methods to forecast them. In this study, two interesting ones are presented:

1.1.4.1. The Bruun's rule

The Bruun's rule gives a linear relationship between SLR and shoreline recession based on equilibrium profile theory, which asserts that shore face profile maintains an equilibrium shape, and as sea level rises the increasing accommodation space forces this equilibrium profile landward and upward to preserve its shape related to the new sea level. It predicts coastal recession to be as much as 10 to 50 times SLR, depending on the slope of the beach. This method is empirical but in a context of climate change, it is the ideal one to use. The mathematical formula of the Bruun's rule is:

$$R = \frac{SL}{h + B} = \frac{S}{tan\beta} \quad (1)$$

Where, R[m] is shoreline recession; S[m] is sea level rise; L[m] is the horizontal length of the bottom affected by the sea level rise, h[m] is the depth of closure, B[m] is the dune height above sea level, β[rad] is the average slope of the active profile.

But the disadvantage of this method is the data availability constraints. Actually, to compute reliable value of S it must have been installed a set of highly accurate instruments for in situ data collection for many years. Even with RS, S value accurate measurement is still

difficult since the high-resolution sensors images are available not too long ago and are still not available in some areas in Africa. This is the reason why the Kalman Filter method was chosen.

1.1.4.2. The Kalman Filter

Proposed by Rudolf E. Kálmán in 1960, Kalman filtering, is an algorithm that uses time series measurements, including statistical noise and other inaccuracies, to produce estimates of unknown variables that tend to be more accurate than those based on a single measurement alone, by estimating a joint probability distribution over the variables for each timeframe (Figure 1). It is a statistical and iterative method in comparison to the Bruun's rule.

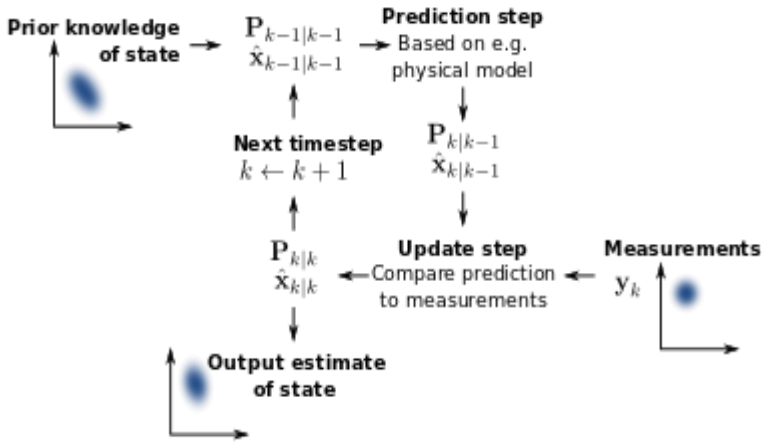

Figure 1: Kalman Filter algorithm flowchart

In our case, the shoreline forecasting calculation is done by using the Kalman Filter, as developed by Long & Plant (2012), to forecast future shoreline positions by combining observed shoreline positions with model-derived positions. The Digital Shoreline Analysis System (DSAS) Kalman Filter approach is initialized with the Linear Regression Rate (LRR) calculated by DSAS (Figure 2), it then estimates the shoreline position and change rate for every 10th month of a year and provides an estimate of positional uncertainty at each time step.

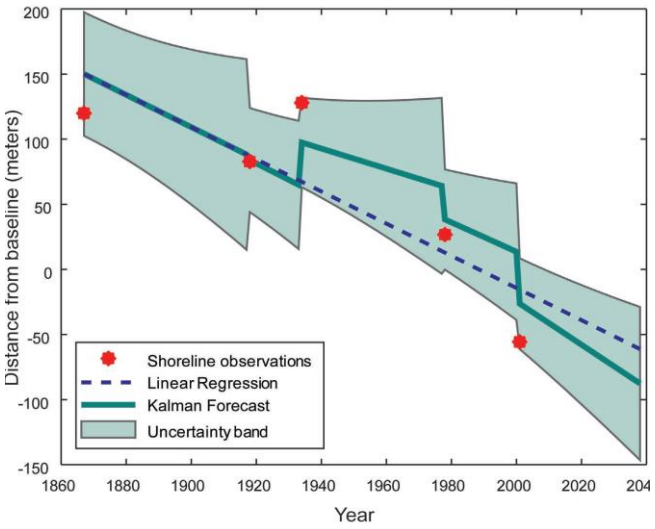

Figure 2: Comparison between Kalman Filter forecast and LRR
Source: (Himmelstoss et al., 2021)

The model begins at the first timestep (the date of the earliest survey) and estimates the shoreline position for each successive time step until another shoreline observation is encountered. Whenever a shoreline observation is encountered, the Kalman Filter performs an analysis to minimize the error between the modeled and observed shoreline positions to improve the forecast, including updating the rate and uncertainties (Long & Plant, 2012). The updated rate is then used to predict the shoreline position for each successive time step until another survey date is reached and again the new data are assimilated into the model. This process is repeated until the desired forecast date is reached. The measurement error is estimated by using the shoreline positional uncertainty associated with each shoreline used in the analysis.

1.1.5. Shoreline change and sea level rise

As stated, waves and tides are part of the numerous drivers of shoreline change. SLR (derived from these drivers) is one of the most significant effects of climate change. High projected rates of future SLR have captured the attention of the scientists. A projected SLR of 18-59 cm by 2100, which was given by the Intergovernmental Panel on Climate Change (IPCC) Assessment Report Four (AR4), can be understood as the lower limit of the possible increase. Figure 3 shows the projected rate of Global Mean Sea Level (GMSL) rise and its contributions as a function of time for the four Representative Concentration Pathways (RCP) scenarios.

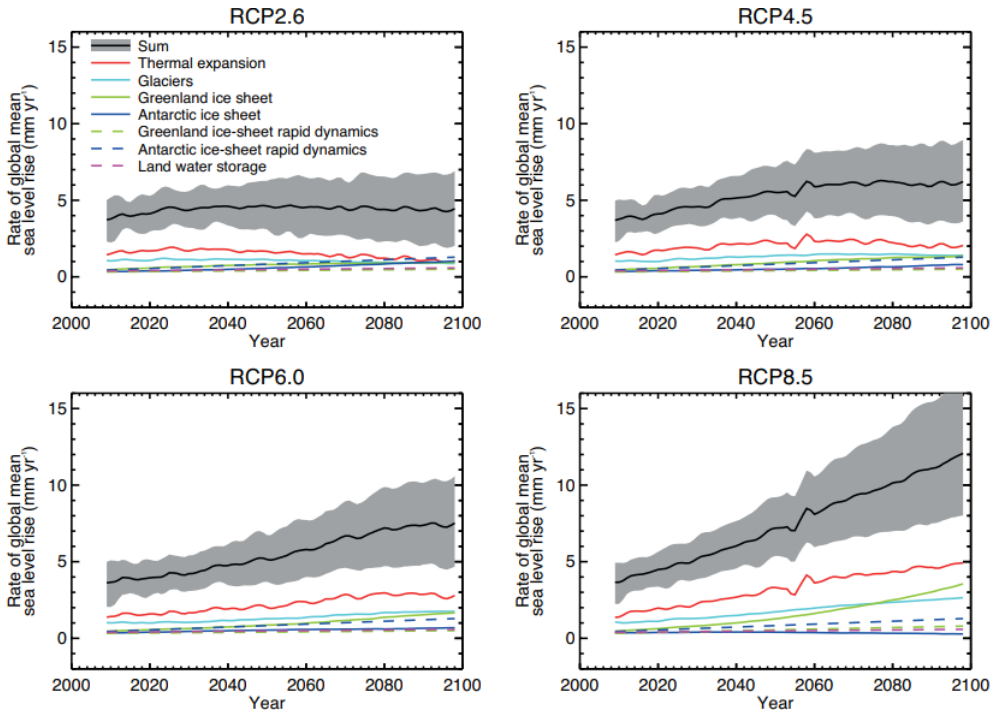

Figure 3: Projected sea level rise for the 21st century
Source: (Church & Gregory, 2019)

The primary direct physical consequence of SLR, among others, is inundation. Inundation increases the rate of shoreline recession or retreat by raising the mean water level upon which the tides, waves and storm surges can attack the beaches, bluffs, embayments and barrier islands of the world's coastlines. As global projections of inundation and recession, it is estimated that the total shoreline length which would be inundated or otherwise affected by a rise in sea-level is 1 m (Tsyban et al., 1990).

1.2. The use of Artificial Intelligence in Remote sensing

1.2.1. Overview of the Artificial Intelligence

A branch of Computer Science named Artificial Intelligence (AI) pursues creating the computers or machines as intelligent as human beings. AI is “The science and engineering of making intelligent machines, especially intelligent computer programs” (McCarthy, 1989). AI is a way of making a computer, a computer-controlled robot, or a software think intelligently, in the similar manner the intelligent humans think.

AI is currently in a new hype phase because of Machine Learning (ML), a technology that helps computers learn from data. Having a computer learn from data means not depending on a human programmer to set operations (tasks), but rather deriving them directly from examples that show how the computer should behave. ML builds its cognitive capabilities by

creating a mathematical formulation that includes all the given features in a way that creates a function that can distinguish one class from another. Artificial Neural Networks (ANNs) are the most popular ML algorithms today. The invention of (A)NN took place in the 1970s but they have achieved huge popularity due to the recent increase in computation power.

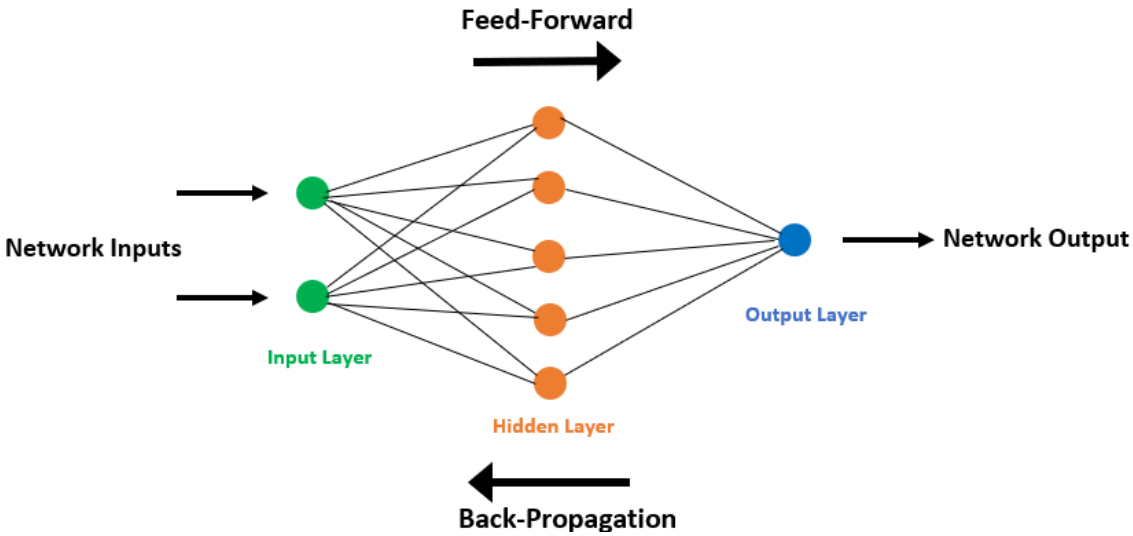

Figure 4: Simple Artificial Neural Network illustration

ANNs are capable of (machine) learning and they need to be trained. There are globally 3 ways to train ANNs machines to learn: Supervised Learning (detailed in the following lines), Unsupervised Learning (Appendix 5), and Reinforcement Learning (Appendix 6). Since it is the one used for this study, the Supervised Learning process was described. It involves a "teacher that is scholar than the ANN itself". The teacher feeds some example data about which the teacher already knows the answers. For example, in pattern recognizing field, the ANN comes up with guesses while recognizing. Then the teacher provides the ANN with the answers. The network then compares its guesses with the teacher's "correct" answers and adjusts according to errors. In the scope of the current study, only the supervised classification will be used. Figure 5 illustrates the supervised learning process.

Supervised machine learning is the search for algorithms that reason from externally supplied instances to produce general hypotheses, which then make predictions about future instances. The main purpose of supervised learning is to build a simple and unambiguous model of the allocation of class labels in terms of predictor features. The resulting classifiers are then used to classify class labels of the testing instances where the values of the predictor features are known, to the value of the class label which is unknown (Reddy & Babu, 2018). The features are the descriptive attributes, and the label is what is attempted to be predicted or forecasted. Further in Chapter 2, the labels and features in the case of our study, were emphasized.

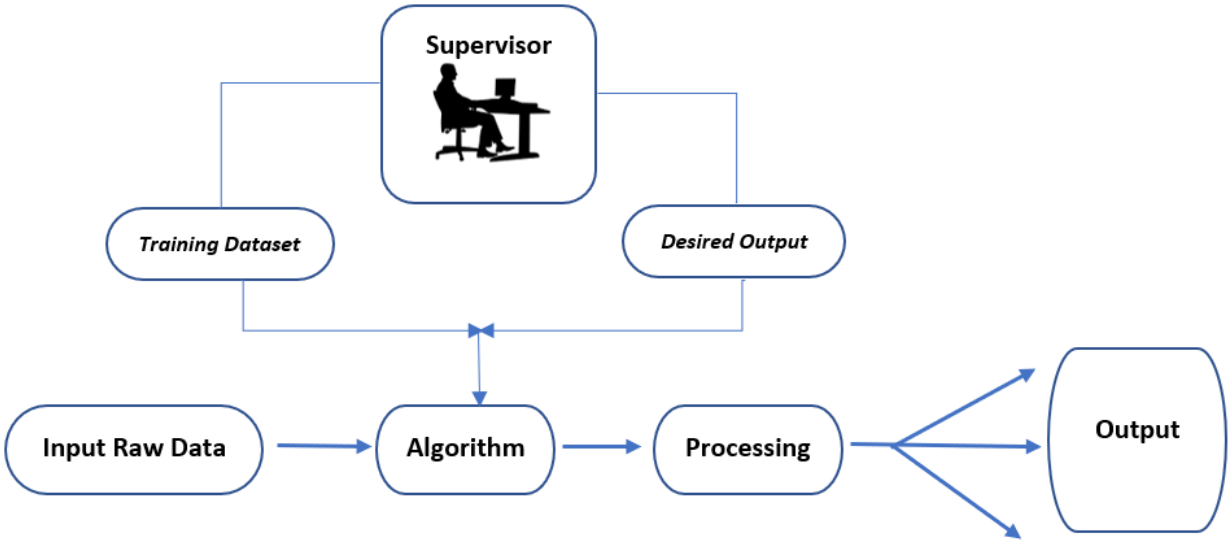

Figure 5: Supervised learning process

1.2.2. The use of AI in Remote Sensing for Earth observation

Remote Sensing (RS) is the science of obtaining information about an object, area, or phenomenon through the analysis of data acquired by a device that is not in contact with the object, area, or phenomenon under investigation (Congalton, 2015). The objective of RS is to collect large amounts of Earth images datasets. The most common RS systems measure reflected visible light, but they can also measure electromagnetic radiation that is invisible to the human eye, e.g. UltraViolet (UV), Infra Red (IR) or microwave radiation. Earth Observation (EO) means information collected from Earth observing satellites, which is obviously done by RS. Another AI field was then introduced: Computer Vision (CV). CV enables computers and systems to derive meaningful information from digital images, videos and other visual inputs, and take actions or make recommendations based on that information (IBM, 2022).

The latest innovation to capturing accurate data over large areas from satellite imagery has been the combined utilization of ML and CV. ML models succeed in many fields related to obtaining large amounts of image data to aid in pattern recognition and create algorithms through computer systems. AI can improve the analysis of large areas of interest, classify objects, detect and monitor land use, data fusion, cloud removal, and spectral analysis of environmental changes from satellite or aerial imagery. Particularly the ML Image supervised classification was used for that purpose in this study. A supervised ML classification algorithm requires a training sample for each class, that is, a collection of data points known to have come from the class of interest. The classification is thus based on how "close" a point to be classified is to each training sample. The training samples are representative of the known classes of

interest to the analyst. The three basic steps (Figure 6) involved in a typical supervised classification procedure are as follows:

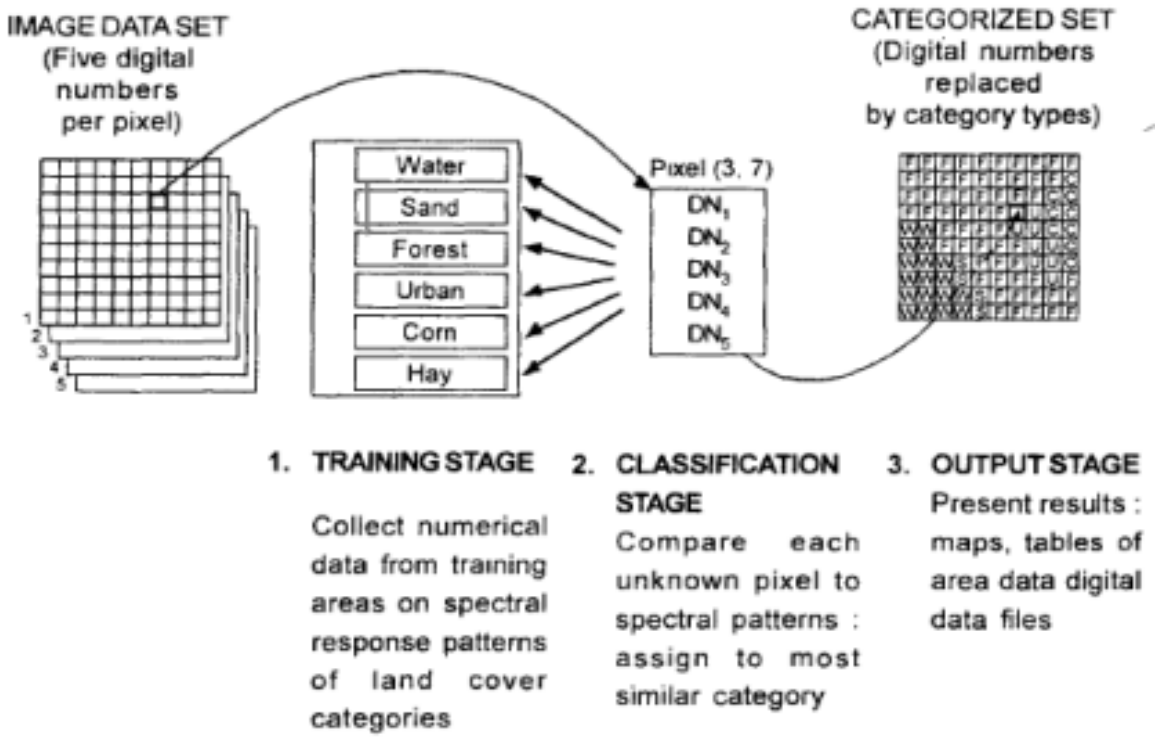

Figure 6: Supervised image classification
Source: (Lillesand et al., 2004)

1.3. State of the art

1.3.1. Previous related studies

Many authors investigated the use of RS to assess shoreline change over a certain time range. For instance, Deabes (2017) used the Model Builder in ArcGIS to design and develop an automated technique to calculate the shoreline change rates along the Nile Delta Coast in Egypt. It was sorted out from this study that the shoreline of Rosetta retreated at an average rate of 60 m/year, Burullus bulge at 6 m/year and Damietta (Ras El-Bar) at 6 m/year. This study even allows to deduce that protection structures didn't solve erosion problem. In the scope of their study, Aedla et al. (2015) developed an automatic shoreline detection method using histogram equalization and adaptive thresholding techniques, and combined it with DSAS in order to monitor shoreline dynamics along Mangalore coast (India). It was found that The Bengre spit, Northern sector of Netravati-Gurpur river mouth is under accretion with an average of 2.95 m/year and maximum accretion obtained is 8.51 m/year while on the Southern sector, the Ullal spit is under erosion with an average rate of -0.56 m/year.

Some of the existing works combined AI and RS to improve the shoreline detection and monitoring. For example, using an image processing approach and a supervised Random Forest (RF) image classification, Njutapvoui et al. (2022) showed that the Cameroon estuary is disturbed by different levels of erosion at some places, and accretion at others, and also by weak internal variations. When conducting a study on monitoring and analysis of coastline change and erosion prediction in Tabanan regency, an Indian coastal region, it was shown that this region underwent an average of 13.96 m coastline change with an average rate of coastal erosion of 1.99 m/year (Aryastana et al., 2018). These results were achieved by performing a high-resolution SPOT (5/6/7) satellite imagery analysis. Studying shoreline change since 1984, all along to 2016, (Luijendijk et al., 2018) applied pixel-based supervised classification and found out that 25% of the worldwide sand beaches have already underwent a rate of erosion of more than 0.5 m/year. The same study pointed out an area of 28,000 km^2 of land swallowed by the sea. In his PhD thesis, (Faye, 2010) analyzed the shoreline dynamics along the coast from Mauritania to Guinea Bissau, and found an erosion of over 47 km (70%) of the coast and accretion of over 20 km (30%). On another plan, in order to identify shoreline changes from 2012 to 2021 and to forecast the shoreline position after 10 years, Dey et al. (2021) used DSAS tool and multitemporal satellite images (Sentinel 2). The results showed that the pattern of the rate of change was more or less the same for the 3 chosen statistical indicators. The same study used Kalman Filter model to predict 10-year further shoreline positions. The same plugin DSAS combined with the shoreline change rate velocity formula was used to perform coastline dynamics analysis and predictions along the Dakar's region coast (Pouye et al., 2022). As results of this study, it was shown that the western and southern coasts record respectively a rate of about 0.21 and -0.11 m/year. In 2030, the average rates of retreat of -4.4, -2.1 and -1.1 m/year were estimated respectively in the northern, western and southern coasts.

Some studies were also conducted more or less on the same study area as the present one. It is the case for instance of the one conducted by Assogba (2018), which used DSAS to map the dynamics of the coastline in Cotonou between 2013 and 2018 and forecast a trend for 2025. It was found from this study that prior to the construction of the coastal defense structures in 2013, the coastline advanced at the West part of the Port and receded at the East part of the Port at a rate of more than 10 m/year. This study was only narrowed to Cotonou (18 km of coast), the capital city. Also Ozer et al. (2017) investigated coastline change trends between 2000 and 2015 in Togo and Benin Republics. They analyzed coastal dynamics using very high Google Earth resolution images to find that 34% of the coastlines are stable, while accretion is recorded

only upstream of harbor infrastructures (14%) and, the remaining 52% coastlines undergo erosive processes, sometimes up to -10 m/year. In the same vein, it was shown that the coastal sectors most threatened by erosion is the East of Cotonou with a mean velocity of approximately -9 ± 0.03 m/year at Donatin and approximately -30 ± 0.03 m/year at the East (at the level of the bridge toll), the sectors of Djondji with -2 ± 0.03 m/year and the sectors between Hillacondji and Agoué with -5 ± 0.03 m/year (Degbe et al., 2017). Another study analyzed the role of erosion and accretion in shoreline changes along the coast between Cape Coast and Sekondi in Ghana (Dadson et al., 2016). They used aerial photographs, satellite images, and topographical maps to achieve the results showing that the sea advanced inland between 1972 and 2005, which is attributed mainly to intense erosion. The study further reveals that, in the past five years, the shoreline had been retreating mainly due to increased accretion. In another study, Arjasakusuma et al. (2021) investigated shoreline changes in East Java Province Indonesia from 2000 to 2019 using Random Forest (RF) and GMO maximum entropy (GMO-Maxent) for image classification and DSAS tool to compute change rate indicators. It was mainly found that coastal erosion happened mostly in the mangrove and aquaculture areas. A different study used a methodology involving the interpretation of different RS data types between 1987 and 2012 to quantify the shoreline displacement rate. From this study, it was found that the average rate of the calculated erosion is in the order of 24 mm/year whilst extreme rates of 1 m/year were also observed in specific positions (Vassilakis et al., 2017).

In addition to the gaps of previous studies mentioned, projection or forecast regarding future shoreline dynamics is also less documented. However, some authors put an emphasis on the shoreline prediction with different methods. For instance, using the Bruun's rule, Patil & Deo (2020) found that future recession of shorelines along the Indian coastline might vary between 14.10-29.22 m and 21.05-45.40 m up to the year 2100 for RCP4.5 and RCP8.5 respectively. It is also the case of the study of Hilton et al. (2020) who developed a shoreline prediction model, forced by synthetic waves to investigate whether forecasts can be improved when the synthetic wave generation algorithm is informed by relevant climate indices. The results of this study showed that improved seasonal predictions of shoreline changes are possible if climate indices are known a priori. In the same vein, Banno & Kuriyama (2014) developed a shoreline change model considering the effects of the wave regime, sea level, and time heterogeneity in order to predict future shoreline positions along the Hasaki coast in Japan. The prediction results (from 2008 to 2095) showed that the shoreline would retreat approximately 20 m by the end of this century due to the rise in sea level.

The majority of the previous studies doesn't include neither the median of image collections nor the combination of the Automated Water Extraction Index non-shadow (AWEInsh), Normalized Difference Built-up Index (NDBI) and slope bands to improve the accuracy of the image classification. The current work will combine these features to point out, if any, improvement on the shoreline evolution prediction.

1.3.2. Existing regional projects and solutions

In terms of projects, the main one including Benin Republic is the West African Coastal Areas Management Program (WACA) involving all West African countries working together to address challenges posed by their shrinking coastline. It was developed by the World Bank Group in partnership with the program's ultimate beneficiaries. This program targets 16 West African countries (Gulf of Guinea). The WACA program provides countries with access to technical expertise and finance to manage sustainably coastal zones, dealing with erosion and hazardous flooding. It was approved by the World Bank in April 2018 with a credit of USD 120 million and a grant of USD 70 million from the World Bank's International Development Association (IDA); and a grant of USD 20.25 million from the Global Environment Facility (World Bank, 2018). The project contributes to the Sustainable Development Goal (SDG) 13 (Climate Action) by allowing climate change action, awareness-raising, and human capacity in climate change mitigation and adaptation and SDG 14 (Life Below Water) by allowing sustainable management and protection of marine and coastal ecosystems. Apart from the WACA project, in Benin Republic, there are other projects like the Early Warning System (EWS), and Gestion Intégrée de la Zone Côtière (GIZC) which contribute significantly in mitigating shoreline retreat in this country.

In terms of software solutions, there is no public open access regional application, platform or data portal helping for coastline monitoring in West Africa. On a global scale, there are some platforms like the USGS Coastal hazards portal which is an open access data portal on USA historical data on extreme storms, SLR, shoreline historical positions. Two web applications can be mentioned in this domain. "CoastSat" is an open-source Python software toolkit that enables the user to obtain time-series of shoreline position at any sandy coastline worldwide from 30+ years of publicly available satellite imagery. "CASSIE" is an open-source JavaScript web tool for automatic shoreline mapping and analysis using satellite imagery. The main limitation of the previous tools, is that they highly depend on the satellite images availability of the study area, hence the need of the proposed web application of this work.

Chapter 2: Materials and methods

In this chapter, the materials and methods used for conducting this work, were described. After a presentation of the study area, a justification of the choice of the area is done, before describing the data collection methods, techniques and justification. This chapter ends by providing details on the change rate statistics chosen for the geostatistical analysis.

2.1. Study area characteristics

2.1.1. Study area location

Located in West Africa, Benin Republic is part of the 16 coastal countries that are located along the Gulf of Guinea: Angola, Benin, Cameroon, Cote d'Ivoire, Democratic Republic of Congo, Republic of Congo, Guinea, Equatorial Guinea, Guinea-Bissau, Gabon, Nigeria, Ghana, São Tomé and Principe, Togo and Sierra Leone. The study area chosen is the Benin Republic coastal area, especially the shoreline, which is 125 km long. For the sake of easiness of illustration, the study area was circumscribed to the area between latitudes 6°09’N to 6°39’N and longitudes 1°30’E to 2°50’E as shown on Figure 7. The coastal zone of Benin Republic is the same as its southern part. This southern part comprises 05 coastal districts which are located all along the coast of Benin Republic. Right following lines are devoted to giving some important characteristics of our study area.

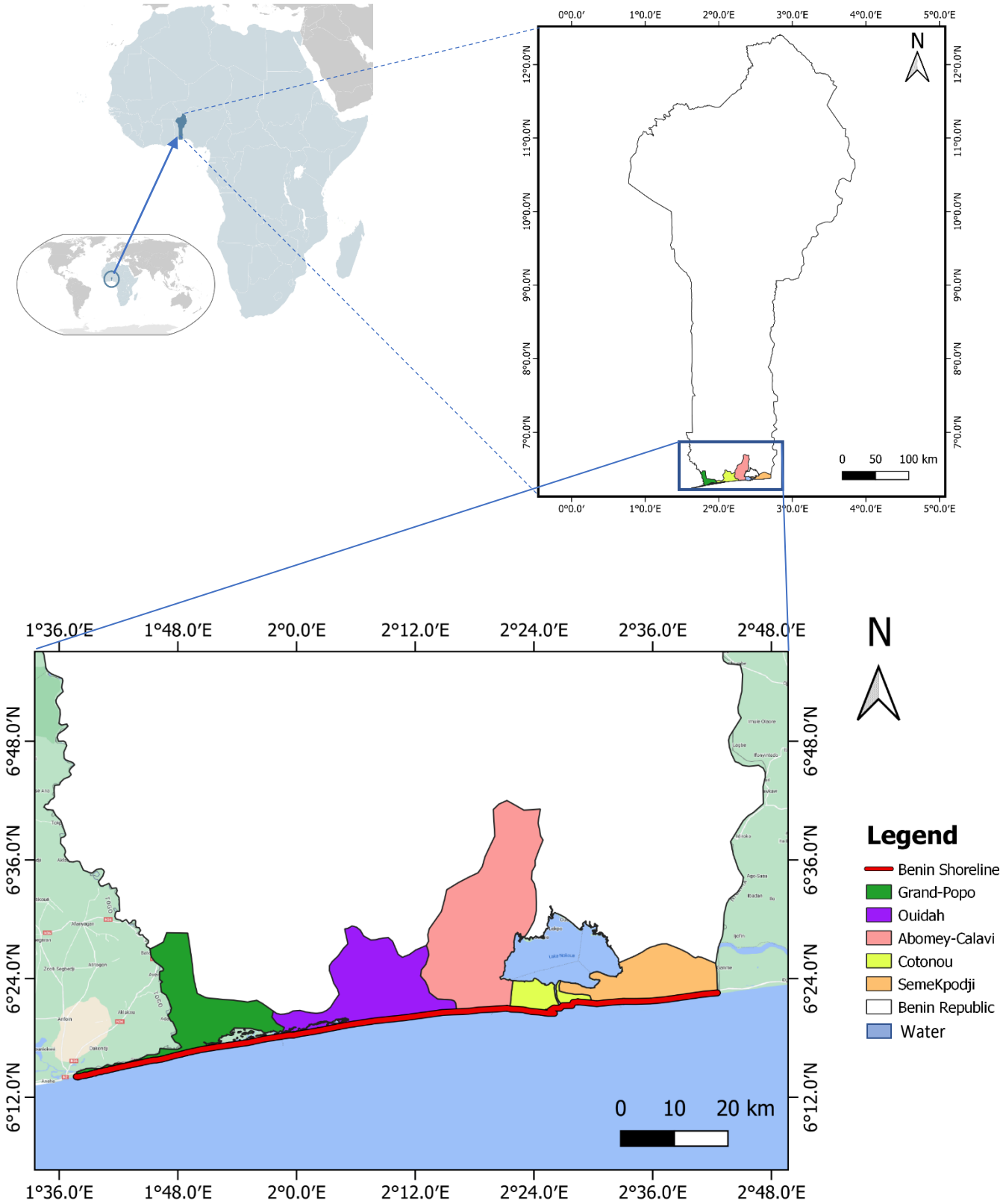

Figure 7: Study area

2.1.2. Climate and Hydrography

In terms of climate, the whole country's climate is hot and humid. But specifically, annual rainfall in the coastal area averages is 1300 mm. Benin Republic (including the coastal zone) has two rainy and two dry seasons per year (Sarr et al., 2015). The principal rainy season is from April to late July, with a shorter less intense rainy period from late September to November. The main dry season is from December to April, with a short cooler dry season from late July to early September. Temperature and humidity are high along the tropical coast. In Cotonou, the capital city located right in the south (coastal area) the average maximum temperature reaches 31°C, while the minimum is 24°C. A dry wind from the Sahara called the Harmattan blows from December to March, when grass dries up, other vegetation turns reddish brown, and a veil of fine dust hangs over the country, causing the skies to be overcast. Southern Benin experiences two wet seasons differing in duration and coinciding with the northern and southern passages of the Inter Tropical Convergence Zone (ITCZ) across the region.

Concerning water sheds, the hydrographic network of Benin is very dense. It is crossed by many rivers. The main ones are the Niger, the Volta, the Mono, the Couffo and the Ouémé. The last three ones are the inland waters which are closest to the shoreline. The Couffo communicates with the Atlantic Ocean through the lake Ahémé, the Ouémé through the Nokoué lake (via the Cotonou and Lagos channel), while the Mono flows directly in the Atlantic Ocean.

2.1.3. Flora and Fauna

Concerning plant biodiversity, in Benin in general, 03 types of vegetation are distinguished: tree savannah in the Sudanese regions of the North, savannah in the Center with trees like *Mahogany*, *Iroko* and *Samba*, and the Forest in the South. But particularly, the flora of the Beninese littoral environment is part of the plant landscape of Dahomey-Gap determined by savannah formations interspersed between the Guinean-Cameroonian-Congolese forest blocks at the East and Guinean at the West. There are many marshy formations of the submerged environments of southern Benin. In the brackish environment, these are the mangrove with *Rhizophora Racemosa* and *Avicennia africana* and the meadows with *Paspalum* and *Typha* (Tossou et al., 2008).

Three types of faunal species contribute to the functioning of Benin Republic coastal ecosystems: the aquatic fauna (crustaceans, whales, dolphins, African manatees and 04 different turtles' species), terrestrial fauna (royal pythons, cane rats, the burrowing squirrel, monkeys, bush pigs) and avian fauna (Antea Belgium nv, 2017). The terrestrial fauna is composed mainly of mammals and reptiles. As for mammals dependent on humid ecosystems, the species

identified are various: the (*Tryonomys swinderianus*), (*Cercopithecus aethiops*) and the (*Potamocherus porcus), and* the wild cat or Haret (*Felis silvestris*). The hippopotamus (*Hippopotamus amphius*) can be seen along the Mono River. As for avian fauna, according to the work of Adjakpa et al. (1996), 168 species of birds have been identified in areas wetlands of southern Benin. All this shows the richness of the coastal flora and fauna biodiversity of Benin Republic coastal area.

2.1.4. Demographics

The littoral zone of Benin is today home to around 60% of the population of Benin out of 8% of the total area of the country (Antea Belgium nv, 2017). It therefore exerts a strong attraction on the hinterland, due to the presence of the major cities of Cotonou, Porto-Novo, Abomey-Calavi, Ouidah, and major equipment and economic infrastructures of the country such as the port, the airport, the highway, the luxurious hotels, etc., are located there. These two major features are in conflict with the problematic land and coastal erosion. According to Institut National de la Statistique Appliquée et l'Analyse Economique (INSAE, 2019), the population will continue to increase, given the current high fertility rate, meaning 4.9 children per woman.

2.1.5. Socio-economic activities

The littoral zone represents the economic "lung" of the country, because sheltering the main cities, the port and airport infrastructures and many industries. The populations carry out various activities: agriculture, fishing, salt production, trade, exploitation of careers, etc.

In tourism sector, the Benin coastal area is characterized by the presence of major tourist attractions, irrationally exploited. According to (Antea Belgium nv, 2017), the number of people working in tourism is 21,935, up to 35,000 (by integrating the informal sector), supporting nearly indirectly 206,500 people.

Agriculture occupies an important place in the economy of the coastal zone. More than 80% of the surfaces sown are devoted mainly to maize and cassava. Palm crops, coconut tree and pineapple, are also important. Vegetable products, such as eggplant, melon, onion, tomato, carrot, watermelon, etc., are also grown.

Salt production is also an important economic activity for coastal populations. The area of salt marshes in the littoral zone was estimated at more than 83 ha in 2001 (Antea Belgium nv, 2017). For the preparation of the brine, the salt farmers mainly use mangrove wood because of its slow burning, even when green (Adounkpè et al., 2021).

The sector of sea transport and port tends to be the most economically worthy one. Vessel

traffic data indicates that several vessels are sailing and/or docking at the Port Autonome de Cotonou (PAC), including small fishing boats, which vary from rowing boat to those with outboard motors, as well as large vessels.

In the fishery and aquaculture sector, the traditional ponds or fish holes practiced in southern Benin and exploited by peasant-fish farmers, once represented the most important method of fish production. The production of these fish holes, generally poorly known, is estimated at 650 tons / year in some regions (Antea Belgium nv, 2017). Fishing plays a vital role given its contribution to reducing unemployment and meeting the protein needs of populations. Lake Nokoué is home to approximately 100,000 people and inland fishing on this lake contributes over 40% of animal protein consumed in Benin (Antea Belgium nv, 2017).

Concerning industrial and mining activities, the agroindustry sector includes oil mills, soap factories, breweries, industries textiles, mirror factories, pasta factories and many bakeries. The building materials industry covers cement plants and sheet metal manufacturing units wavy. Extractive activities are represented by lagoon sand quarries. Indeed, in order to curb coastal erosion, the Beninese State issued, in October 2008, the decree No. 2008-615 to prohibit the collection of beach sand, while recommending, by the same decision, the exploitation of lagoon sand.

2.1.6. Justification of the study area choice

Based on the brief previous presentation of Benin Republic characteristics, this study area was chosen mainly because it constitutes a very important and strategic source of income of the country. Indeed, through the “Port Autonome de Cotonou”, Port traffic was increased to 5,152 million tons in 2005 before modernization work in 2008-2010 (Antea Belgium nv, 2017). The port of Cotonou provides a significant part of the import-export traffic with the landlocked countries of West Africa (Mali, Burkina-Faso and Niger).

In terms of demography, the demographic and urban dynamism of the five coastal municipalities (Figure 7) is worrying. In fact, in these districts in full demographic explosion, the viable space for urbanization is at dominance constituted by low-lying coastal strips threatened by the risk of coastal erosion and flood**.** Concerning the coastal ecosystem, the richness of the Benin Republic can be sorted out from the short presentation above. It means that potential coastal erosion or flooding can lead to the loss of all the different species listed above. About all the socio-economic activities (fishery, agriculture, etc.) done by the costal population, it is obvious that coastal erosion and flood represent a major threat for them.

In sum, the main threats on Benin coastal area are erosion and flood. Considering the

variety of Benin coastal ecosystems, it appears crucial to monitor the littoral zone in order to anticipate and mitigate this biodiversity loss.

2.2. Data collection

For this work, data from two satellites sensors were used. The specifications of the image collections used are mentioned in Table 1. The acquisition was made through the Google Earth Engine (GEE) Data Catalog. GEE is currently the most popular free and open online satellite images data catalog. First, Landsat 5, 7 and 8 image collections were acquired. The data provider for our Landsat images is the USGS, the largest and open-access Landsat archive. The data from these 03 Landsat sensors are basically available between 1984 and 2022. Because of non-availability of exploitable Landsat images before 2001, the study was set to start from 2001. Surface Reflectance images were used because unlike Top of Atmosphere images, they are obtained from direct reflectance of radiations from different surface phenomena.

These images were chosen because they are a substantial improvement in the absolute geolocation accuracy of the global ground reference dataset, which improves interoperability of the Landsat archive through time.

Second, the 30-meter resolution Digital Elevation Model (DEM) data from the Shuttle Radar Topography Mission (SRTM) was used (Farr et al., 2007). The SRTM is the most complete, highest-resolution, global level digital elevation model currently available for free scientific use. The SRTM project was a joint endeavor of National Aeronautics and Space Administration (NASA), and the German and Italian Space Agencies (JPL-Caltech) and was produced in February 2000.

Table 1: Summary of Image Collections used

Satellite/ Sensor	**Acquisition period**		**Specifications / Spatial resolution**	**Temporal resolution**	**Data provider**
	Start	End			
Landsat5 TM	1984-03-16 16:18:01	2012-05-05 17:54:06	Surface Reflectance / 30 m	24 days	USGS
Landsat7 ETM+	1999-05-28 01:02:17	2022-04-06 14:30:01		16 days	
Landsat8 OLI	2013-03-18 15:58:14	-		8 days	
SRTM	2000-02-11 00:00:00	2000-02-22 00:00:00	Digital elevation / 30 m	-	NASA/USGS/ JPL-Caltech

Many of the studies in the literature, directly choose often the most exploitable image per year (Aryastana et al., 2018; Dey et al., 2021). The study area which is Benin Republic coastline is located around latitude 6°~7°N. Because of its geographic position, satellite images of this region are persistently full of cloud during the whole year. Thus, the originality of the current work is to combine all the available images (cloud contaminated) and apply the median function in order to retrieve the most representative clean and cloud-free images. It is an alternative solution in case of non-availability of clean representative single image per year, which is the case for this study. Details about the application of this function are provided in the data processing section (section 2.3). Added to that, the purpose of the choice of Landsat and SRTM was globally motivated by the extraction of some bands which are required to pursue our analysis. Details are provided about the different extracted bands, in the next lines.

2.3. Data processing and analysis

In this section, first, a general workflow of the methodology that was followed in the scope of this study was proposed (Figure 8). Then after this overall architecture, each great block has been detailed.

2.3.1. Description of the general methodology

First of all, after acquiring all types of image collections, the data was preprocessed. It is the first great block to be detailed encompassing a lot of functions. The purpose of our data preprocessing is to check the availability and exploitability of the acquired data like done by many authors (Arjasakusuma, 2021; Assogba, 2018; Hackman et al., 2017). This is a crucial step in any data analysis. It allows to have as output clean datasets, fulfilling the necessary requirements to proceed.

Thus, the output preprocessed (atmospherically and geometrically) images were now ingested in the second great block to be broken down: the supervised classification block. This block encompasses the 2 different classification algorithms used. Here a binary classification was performed. The two defined classes are: The Sea Water class (Class 1) and the Non-Sea Water class (Class 2). So, the labels are “Class 1” and “Class 2”. The outputs from this block are the classified images.

These outputs were then ingested in the third great block to be detailed: the Geographic Information System. From this last block, the different final results were obtained. The different results were now compiled and presented via a GEE web application interface.

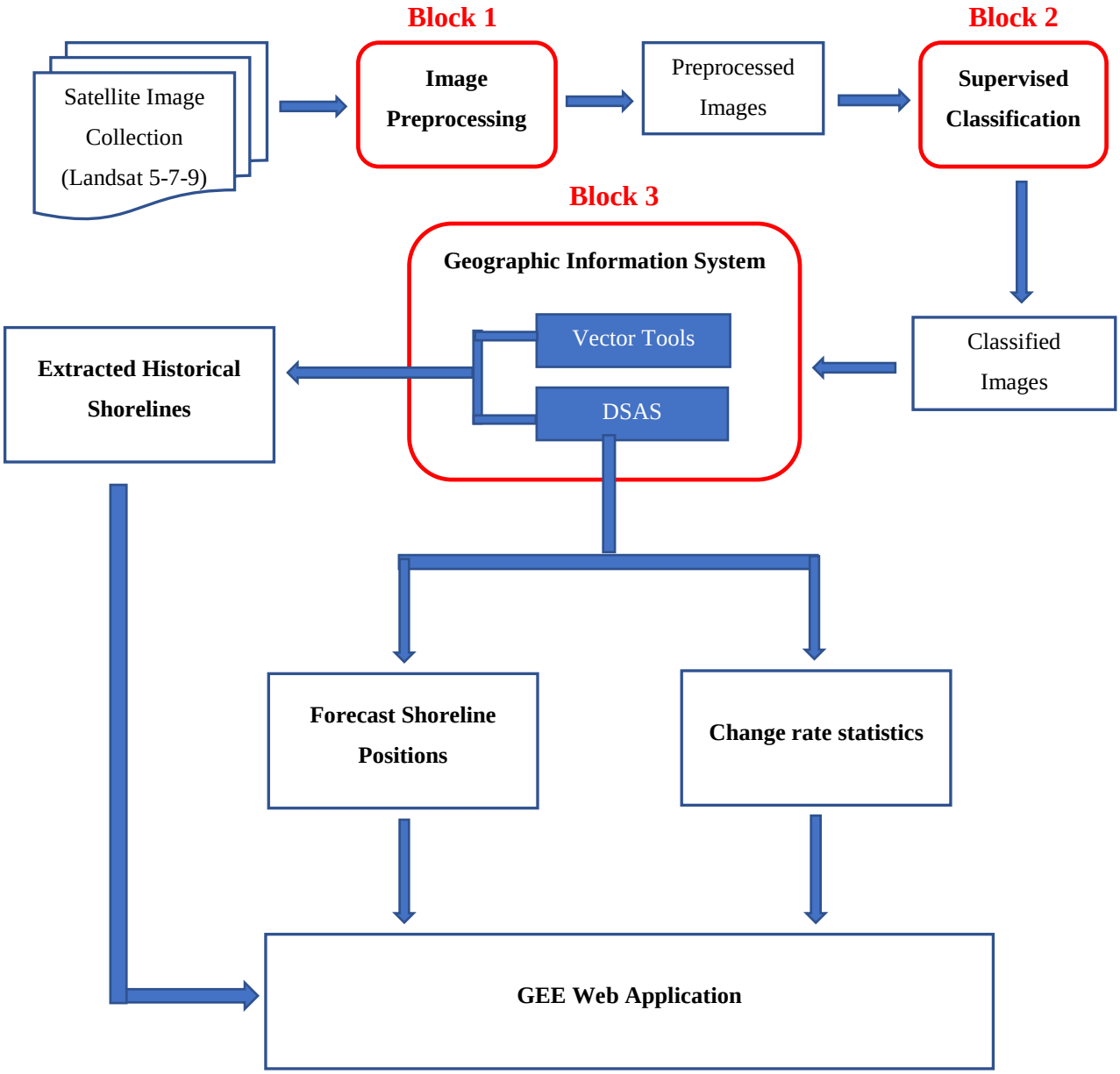

Figure 8: General workflow

In order to implement this methodology, a set of resources have been used. Table 2 mention the different resources used, the hardware infrastructure hosting each of them, as well as their respective purpose.

Table 2: Resources used

Resource	Platform location/infrastructure	Purpose
Google Earth Engine	Online (Cloud)	• Images acquisition • Images preprocessing • Web application building
QGIS	Local machine	• Random sampling • Vectorization
ArcGIS		• Shoreline extraction • Shoreline forecast
R		• Statistical Data Analysis • Data visualization
Google Earth Pro	Online	• Historical georeferenced images extraction

2.3.2. Block 1: Image preprocessing

In this section, the preprocessing block was detailed. Figure 9 shows the specific flowchart of the image preprocessing block. 09 subblocks were necessary in this block. They have been detailed in the following lines.

2.3.2.1. Cloud masking

Most of the studies directly used the USGS provided single images with the constraining cloud contamination (Arjasakusuma et al., 2021; Assogba, 2018). But for the current study, a customized cloud masking function was developed, that allowed to mask all the cloud contaminated pixels on each image of the collection. The developed function uses as arguments the QA-bands (*QA_PIXEL and QA_PIXEL Bit Mask*) to extract information about cloudy pixels and mask them (source code in Appendix 1).

2.3.2.2. Scaling factor and offset applying

A function was then designed to apply the scaling factors and the offset to each of the Landsat images within each collection. This subblock has the role to produce a much more natural brightening/darkening effect than simply adding an offset to the pixels, since it preserves the relative contrast of the image better. The scale factor of the used collection is *0.0000275* and the offset is *-0.2*.

BLOCK 1

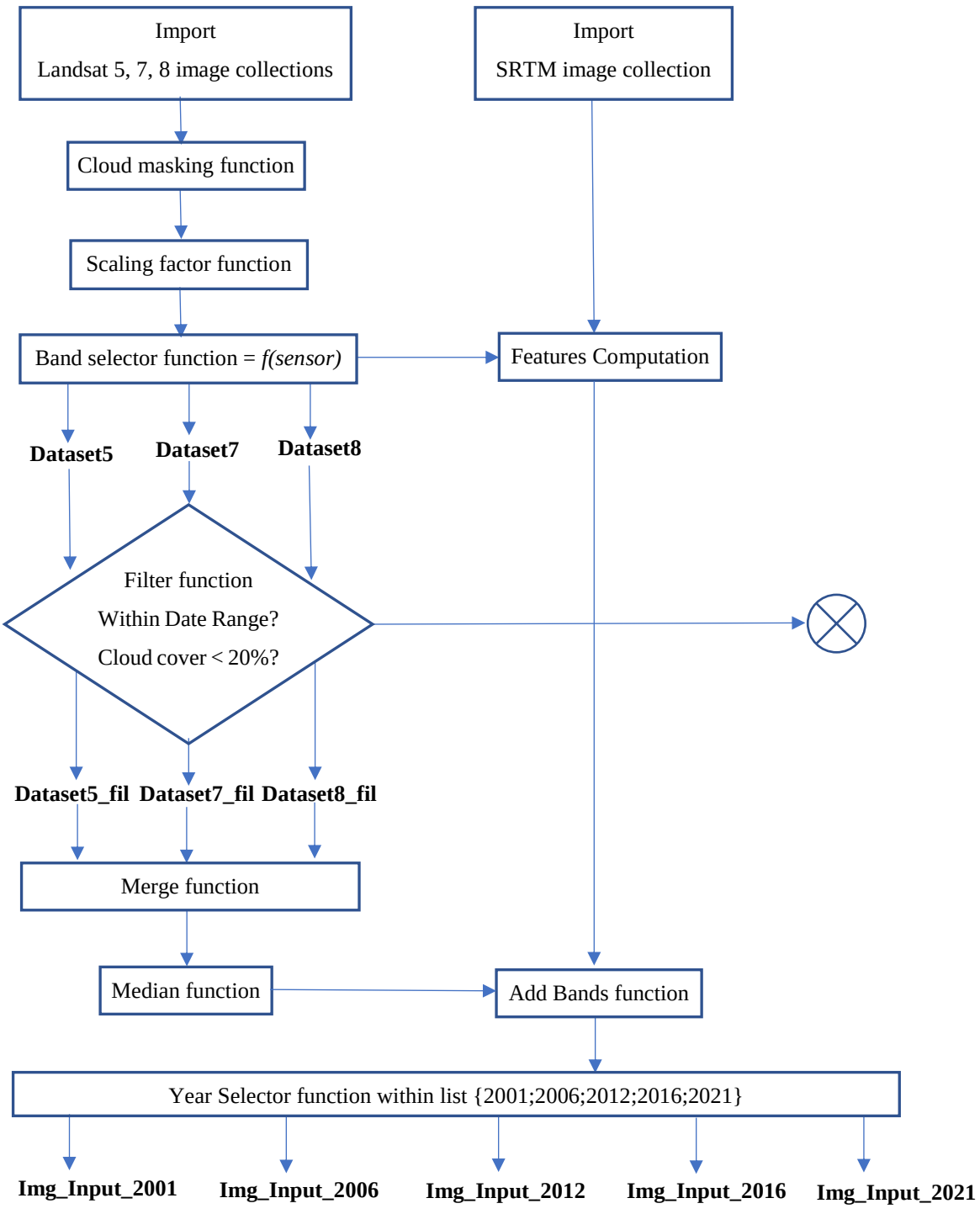

Figure 9: Images preprocessing flowchart

2.3.2.3. Band selector

This subblock is part of the critical ones in our process. Here, a function was designed to select the required optical bands in function of the satellite generation. From the Landsat images, 06 original bands were selected to proceed: Blue, Green, Red, Near Infra Red (NIR), Short-Wave Infra Red 1 (SWIR1) and Short-Wave Infra Red 2 (SWIR2). The specifications of the selected bands are reported in Table 3. The only band of the DEM collection was also selected. All the selected bands, were used to compute additional bands which are further detailed in this section. All the different selected bands (raw and computed) represent the features of our machine learning classifier. From this subblock, there are 03 lists of images datasets outputs.

2.3.2.4. Filtering and Merging

The next subblock designed is the filter function. The 03 outputs from the previous step are ingested in this subblock to be filtered considering 02 filter criteria. The block checks if the images belong to the selected time range (2001-2021) and if the cloud contamination threshold (< 20%) is reached. The outputs of this stage are 03 new filtered images datasets.

As indicated by its name, the *Merging* subblock has the role to merge the 03 last outputs into one to be able to proceed with the next stage.

2.3.2.5. Median

The median subblock function is important because it helps us to use all the available images within a certain year and to retrieve the median pixel values of the different features on each image.

2.3.2.6. Additional features computation

To proceed with our analysis, the computation of some important indices was required. Even the choice of the satellite missions depended on them. Four additional indices were computed in order to improve the accuracy of the image classification. Added to these 04 indices, the slope using the DEM raster data was also computed. Table 3 shows the computation method for each of them.

Table 3: Selected bands specifications and computation

Selected Bands	Spectral range (µm)	Computation formula	Spatial resolution
Blue (B)	0.45 - 0.52	-	30 m
Green (G)	0.52 - 0.60	-	
Red (R)	0.63 - 0.69	-	
Near Infrared (NIR)	0.77 - 0.90	-	
Short Wave Infrared 1 (SWIR1)	1.55 - 1.75	-	
Short Wave Infrared 2 (SWIR2)	2.08 - 2.35	-	
NDVI	-	$\frac{\rho_{NIR} - \rho_R}{\rho_{NIR} + \rho_R}$ (2)	
NDBI	-	$\frac{\rho_{SWIR1} - \rho_{NIR}}{\rho_{SWIR1} + \rho_{NIR}}$ (3)	
NDWI	-	$\frac{\rho_G - \rho_{NIR}}{\rho_G + \rho_{NIR}}$ (4)	
AWEInsh	-	$\frac{(4 \times (\rho_G - \rho_{SWIR1}) - (0.25 \times \rho_{NIR} + 2.75 \times \rho_{SWIR1}))}{(\rho_G + \rho_{SWIR1} + \rho_{NIR})}$ (5)	
Elevation	-	-	
Slope	-	$s = \tan^{-1}\left(\sqrt{\left(\frac{dz}{dx}\right)^2 + \left(\frac{dz}{dy}\right)^2}\right)$ (6)	

Where the ρ_i represents surface reflectance value of the band i.

For the slope computation, the rate of change in the x direction for cell e is calculated with the following algorithm:

$$\frac{dz}{dy} = \frac{\left(\frac{(g + 2h + i)}{wght1} - \frac{(a + 2b + c)}{wght2}\right)}{2 \times x_{cellsize}} \quad (7)$$

Where wght1 and wght2 are the horizontal weighted counts of valid cells (Appendix 4).

2.3.2.7. Importance of the computed indices

The computed indices and the slope band are added on images as new bands. They represent the different features to be considered by the classifier. All of them were used to stretch the presence of water over the study area.

Normalized Difference Vegetation Index (NDVI)

NDVI quantifies vegetation by measuring the difference between Near Infra Red (which vegetation strongly reflects) and Red light (which vegetation absorbs). It is a common graphical indicator used to analyze RS measurements by assessing whether or not the observed target contains live green vegetation. It can help to differentiate water from land. For example, negative values of NDVI are associated to the "Water" class (Ya'acob et al., 2014).

Normalized Difference Built-up Index (NDBI)

NDBI uses the NIR and SWIR1 bands to emphasize manufactured built-up areas. It is ratio based to mitigate the effects of terrain illumination differences as well as atmospheric effects. This index is provided as feature to train the machine learning classifier to classify pixels on which there are Built-up areas in Class 2 (Non-Sea Water). For instance, (Watik & Jaelani, 2019) proposed that pixels NDBI values comprised between -1 and -0.01 can be classified as "Water".

Normalized Difference Water Index (NDWI)

NDWI is used to highlight open water features in a satellite image, allowing a water body to "stand out" against the soil and vegetation. It is calculated using the Green-NIR combination, which allows it to detect subtle changes in water content of the water bodies. It is the index by excellence to detect water bodies on a satellite image. From the classification proposed by (Gulácsi & Kovács, 2015), if a NDWI pixel is comprised between 0.5 and 0.7, this pixel is classified in the "Water" class.

Automated Water Extraction Index non-shadow (AWEInsh)

AWEInsh was created to reduce the confusion between water and non-water pixels, as well as dark surfaces included in urban background areas. The subscript "nsh", or non-shadow, means that the index is best suited for areas where shadows are not present or pose no problems for classification. This index performance surface water detection was used as done by Worden & de Beurs (2020). As defined in the same study, positive value of AWEInsh corresponds to "Water" class pixels.

Slope computation

The slope derived from the DEM raster data was used to facilitate the elimination of confusion between water pixels and pixels containing high elevation shadows like done by (Worden & de Beurs, 2020). The function *ee.Terrain.slope()* predefined in GEE functions catalog, was used for this purpose.

2.3.2.8. Adding bands and year selection functions

Then, the preprocessing was continued by developing a function to add the different computed and extracted parameters to the filtered image datasets. After that, another function was designed to select the individual year chosen for the work. This is the last step of the preprocessing phase. The output from this subblock and thus from the preprocessing stage, is a set of 05 clean, exploitable, cloud-free median images ready for the next stage.

2.3.3. Block 2: Supervised image classification

In this section the different steps for the image classification were detailed. As stated few lines above, a binary classification was performed. The 2 classes are the Sea Water class (Class 1) and Non-Sea Water (Class 2). The features used to train the classifier are composed of the 07 original bands of the image collections and the 05 additional computed parameters (Table 3). Here, there are 05 main subblocks. But the whole process is a loop iterating for each of the 05 output images from the block 1. Figure 11 illustrates the block 2.

2.3.3.1. Random Sample points collection

This is also a critical stage for the accuracy of the classification. Our sampling was done in QGIS. A total of ***500*** random sample points over the study area was generated (Figure 10). Then, each of the random points were scrutinized to be assigned a label (Class 1 or Class 2). It is also important at this stage to have a very good knowledge of the field of the study area. If eventually, a point does not fit perfectly with one or the second class, this point is simply deleted and replaced by a new one. The purpose of this caution is to not confuse the classifier. For each year, the 500 points were overlaid on a historical Google Earth Pro image to assign a label to each of them according to respective year.

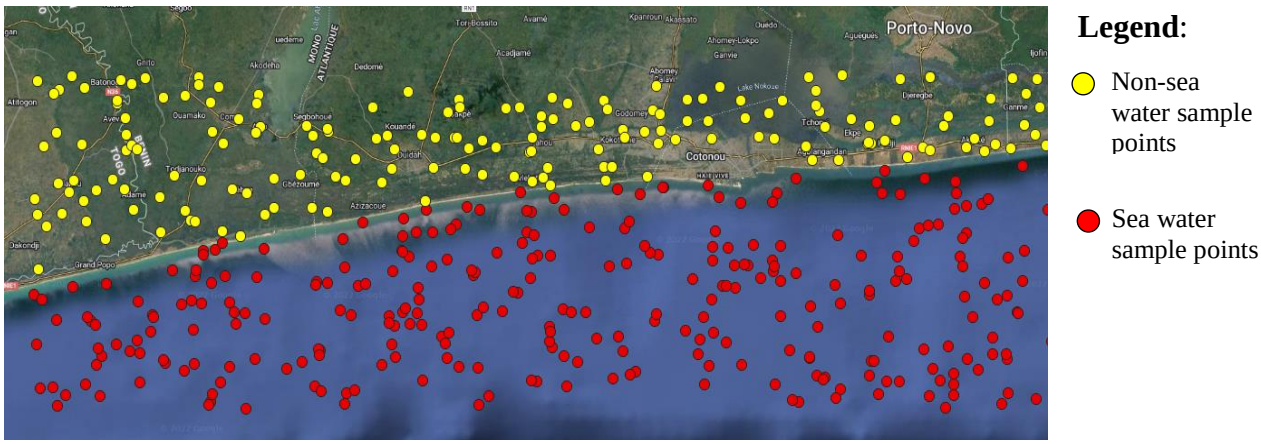

Figure 10: Sampling points for classifier training

2.3.3.2. Split function

This subblock was designed to split the random point dataset into two points datasets. The first one is the training dataset which chosen here representing 70% of the whole dataset and the remaining 30% are reserved for the model testing. The two points datasets are the outputs of this subblock.

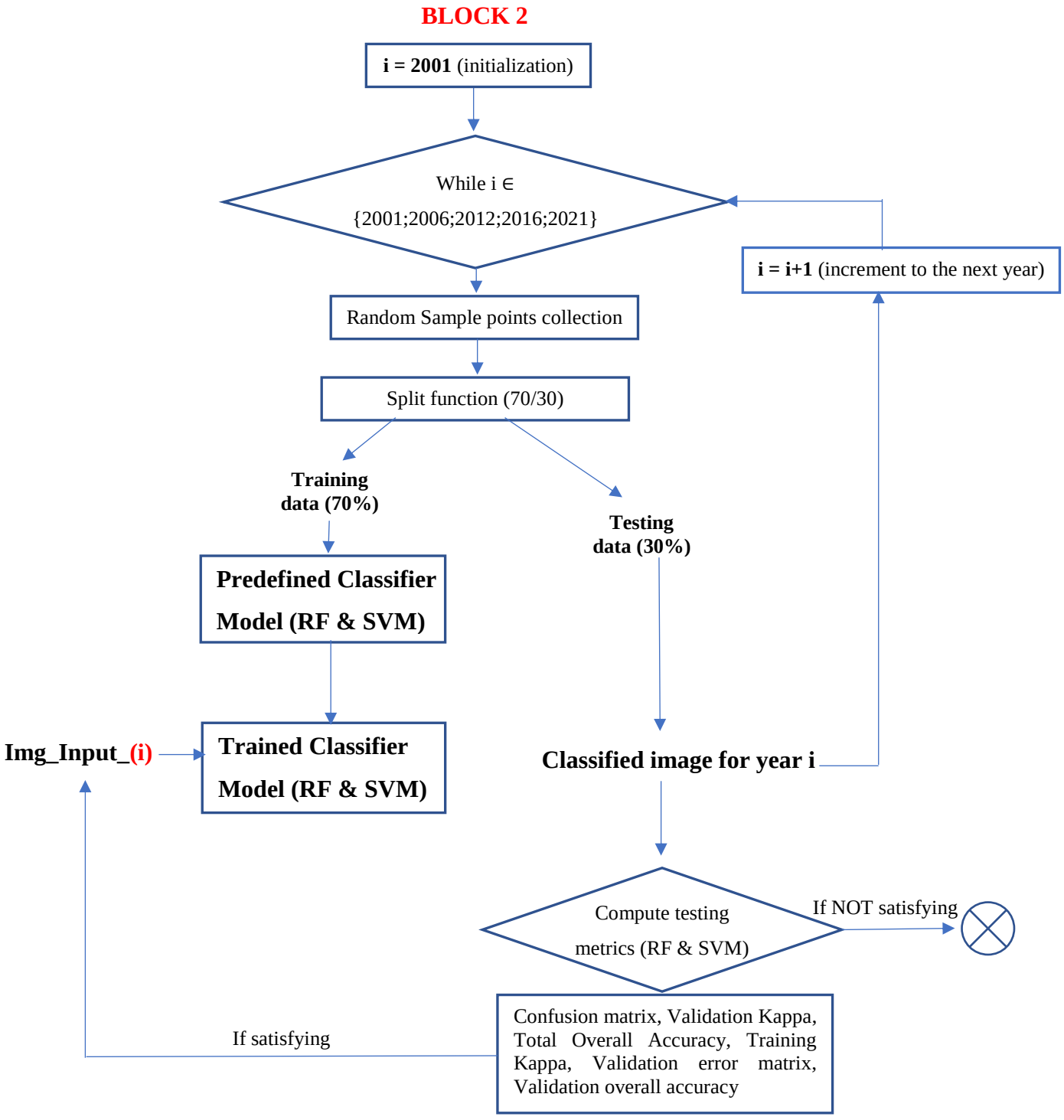

Figure 11: Supervised image classification flowchart

2.3.3.3. Predefined/Trained Classifier Model

The classifier Model is the central subblock of our work. This allowed us to generate the classified image. The used classifiers here are RF and SVM.

Principle of RF image classification

Decision trees (DT) are arguably the most intuitive classification algorithms and provide

a good entry point into the applied side of things concerning image classification. Principally, the DT is not more than a set of decision-rules which converts continuous information, such as spectral information from an image, into discrete thematic information, such as a land cover class. Each pixel will be assigned to a land cover class if its spectral information (or spectral transformations like vegetation indices) fits certain criteria. The name "Decision Tree" comes from its structure, which is organized hierarchically in simple binary (yes/no) decisions.

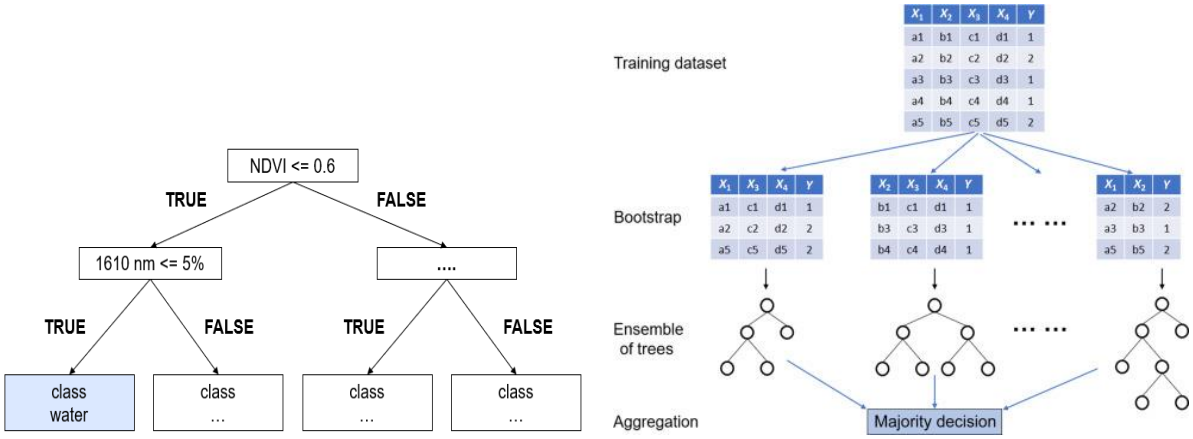

(a) DT image classification using NDVI (b) RF image pixels classification

Figure 12: RF Image classification illustration

Source: Humboldt-Universität zu Berlin, 2021

RF consists of a large number of individual decision trees that operate as an ensemble. Each individual tree in the RF spits out a class prediction and the class with the most votes becomes our model's prediction. RF takes advantage of this by allowing each individual tree to randomly sample from the dataset with replacement, resulting in different trees. This process is known as bagging. The idea behind using many decision trees (i.e. an ensemble) is that many base learners can come to one strong and robust decision compared to a single DT. RF uses self-learning decision trees. These trees automatically define rules at each node based on a training dataset. RF seeks to minimize the heterogeneity of the two resulting subsets of the data created by the respective rule. Many trees may produce different class labels for the same data point. The final class assignment of each image pixel is thus based on the majority vote.

Principle of SVM image classification

SVM constructs a hyperplane in multidimensional space to separate different classes. SVM generates optimal hyperplane in an iterative manner, which is used to minimize an error. The core idea of SVM is to find a maximum marginal hyperplane that best divides the dataset into classes. SVM classification is essentially a binary (two-class) classification technique,

which has to be modified to handle the multiclass tasks in real world situations for instance the derivation of land cover information from satellite images (Anthony et al., 2007). The 1AA approach represents the earliest and most common SVM multiclass approach (Melgani & Bruzzone, 2004) and involves the division of an N class dataset into N two-class cases. If say the classes of interest in a satellite image include water, vegetation and built up areas, classification would be affected by classifying water against non-water areas i.e. (vegetation and built up areas) or vegetation against non-vegetative areas i.e. (water and built up areas). This approach is the one implemented in GEE and is the one used for our work.

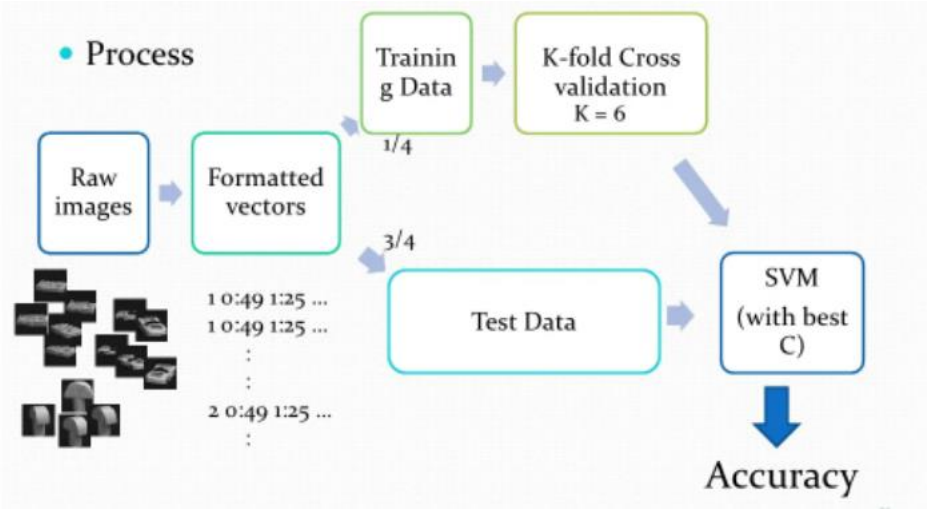

Figure 13: Image classification by SVM

In this subblock the two classification algorithms were performed. The output of this stage is a set of 05 study area classified images for each model (RF and SVM). The results classified images are illustrated on Figure 16 further in chapter 3. Then, to proceed with the shoreline extraction, choosing one model was compulsory. That is the purpose of the next subblock.

2.3.3.4. Classification accuracy metrics computation

In this subblock, the accuracy metrics for the comparison between the two classifiers RF and SVM were computed in the case of our study. A total of 06 accuracy metrics were computed for this purpose: Confusion matrix, Validation Kappa, Total Overall Accuracy, Training Kappa, Validation overall accuracy, to be compared to each other for both classifiers (Table 5).

2.3.4. Block 3: Geographic Information System (GIS) processing

In this block, the different steps to achieve the final results were detailed. Figure 14 illustrates the different subblocks composing the third block. Here is their detailed description.

2.3.4.1. GIS vectorization toolbox

At this step, two of the vectorization tools of the GIS toolbox were first used. The first one is the *Raster to Polygon* tool. Each of the classified image is ingested in this tool. The idea is to transform the raster data into a polygon shapefile retrieving only the contours derived from the different pixels' colors geometrical limit. This gives us a set of polygons. The second tool used is the *Polygons to Polylines* tool. This one allowed us to derive only lines from the polygon shapefile. After a manual cleaning of the result polylines file, each of the 05 historical shorelines could now be isolated by overlaying the result file on a Google Earth Pro historical image of the study area. The output of this stage is a set of 05 (2001, 2006, 2012, 2016, 2021) historical shorelines over the chosen study area.

2.3.4.2. Digital Shoreline Analysis System (DSAS) plugin

The DSAS (version 5) software is a plugin added to ArcGIS Desktop (version 10.7) enabling the end user to calculate rate-of-change statistics from a time series of vector shoreline positions. It provides an automated method for establishing measurement locations, performs rate calculations, provides the statistical data necessary to assess the reliability of the rates, and includes a beta model for forecasting shoreline position.

Before using it, DSAS requires a first step of default setting where many default settings are provided. The most important ones are the metadata (General information, contact informations of the author and the institution, etc.) and the default uncertainty for the shoreline change rate computation. It was set here at **± *10 m***. The uncertainty setting step is very important and is highly dependent on the reliability of our historical shorelines. the level of uncertainty was set at ***10 m*** in this study.

BLOCK 3

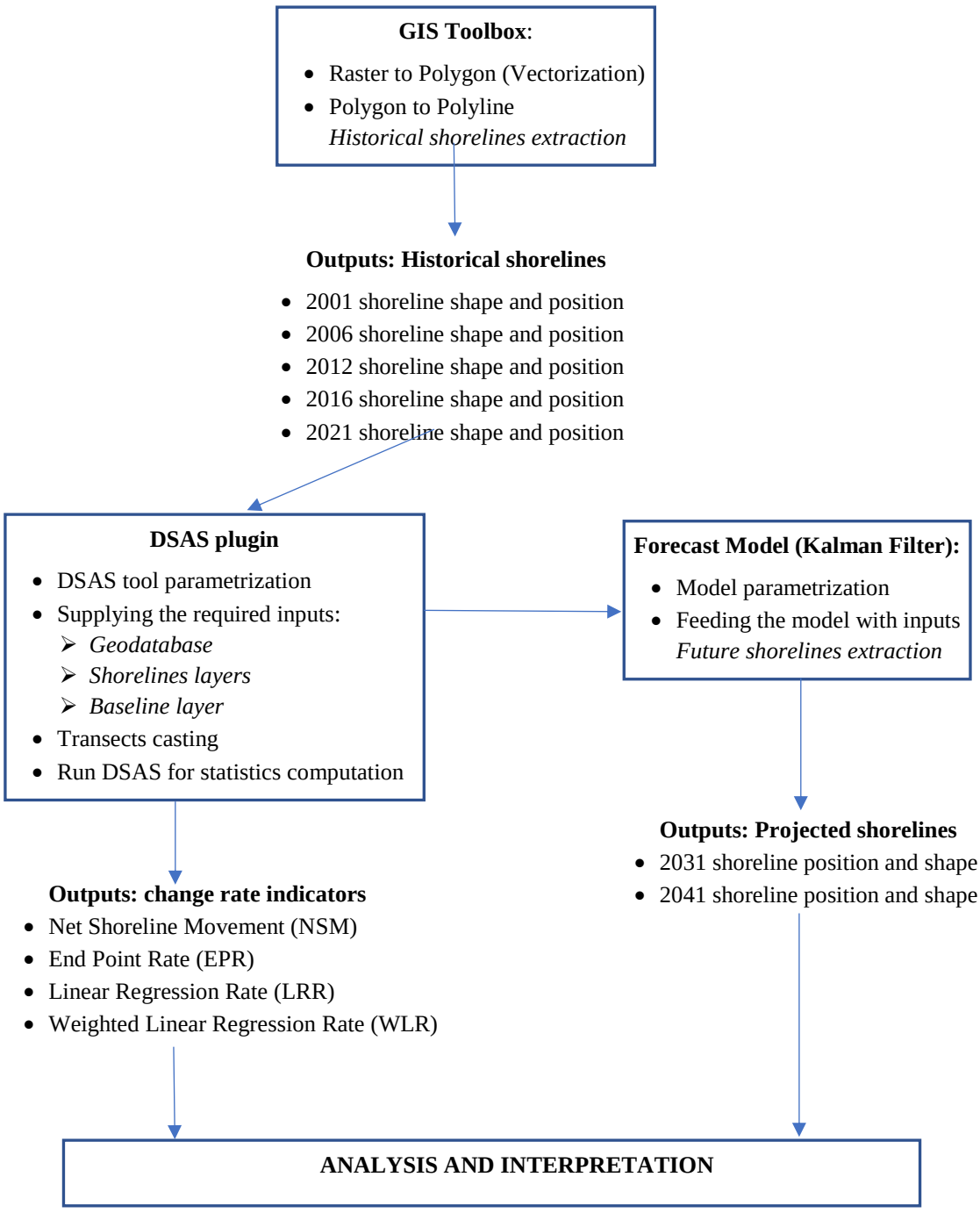

Figure 14: GIS use flowchart

The second step of the DSAS tool consists in supplying the required inputs. A personal geodatabase and the different fields are noted in the DSAS user's guide (Himmelstoss et al., 2021). Then the different shoreline layers (to be mandatory merged in one single shoreline shapefile) and the baseline layer were specified. In our case, to run DSAS, the 2001 shoreline

was chosen as a baseline since it is really adjacent to all the extracted historical shorelines and given that 2001 is an ideal starting point for our analysis.

The next step is the transects casting. At this step many parameters are provided to the tool. But the most important are highlighted:

Maximum search distance: This value (in meters) is set by the user to establish a single search distance for all baseline segments. This value was set at ***50 m*** in our case

Transect space: This value allows the user to specify distance (in meters) between transects along the baseline. Spacing depends on the scale of the data and the intended scale of the output rate information. Since the study area is the whole Benin Republic shoreline, for the sake of fast computing and analysis, it was found appropriated to set this value at ***1000 m***.

Smoothing distance: The user-specified smoothing value can facilitate an orthogonal transect/shoreline intersect by creating a supplemental baseline (not visible to the user) at the provided smoothing length, with the transect location at the midpoint. The intent of smoothing is to prevent transects from intersecting one another when the baseline has a curve. In our case, it was specified at ***500 m***.

Confidence Interval: The user specifies the confidence interval representing the degree of confidence up to which the rate computation is reliable. Here, ***90%*** was selected for that.

After providing all the needed information for the DSAS default settings, its parametrization and the transects casting, the next step was to run the change rate indicators computation. In the scope of our analysis, 04 shorelines change rate indicators has been selected. The summary of the DSAS tool parametrization for change statistics computation is recorded in Table 4.

Table 4: Summary report of DSAS parametrization

Shoreline dates used	• 1/1/2006 • 1/1/2012 • 1/1/2016 • 1/1/2021
Baseline layer	2001 shoreline
Shoreline layer	2006, 2012, 2016, 2021 merged shoreline layers
Rate types run	• Net Shoreline Movement (NSM) • End Point Rate (EPR) • Linear Regression Rate (LRR) • Weighted Linear regression Rate (WLR)
Confidence Interval (CI) selected	90 %

Uncertainty	10 m
Transect spacing length (m)	1000 m
Smoothing distance (m)	500 m
Coordinate system	WGS_1984_UTM_Zone_31N

2.3.4.3. Chosen change indicators

In order to evaluate the dynamics of historical shorelines, 04 significant indicators were picked:

- **Net Shoreline Movement (NSM)**

The NSM is defined as the distance between the oldest and the youngest shorelines for each transect. This statistic was chosen to highlight the extent of change in the shoreline shape between 2001 and 2021 regardless the in-between (or intra time range) fluctuation. This gives an idea especially of the net distance of beach lost during the last 20 years.

- **End Point Rate (EPR)**

The EPR is calculated by dividing the distance of shoreline movement by the time elapsed between the oldest and the most recent shoreline. The major advantages of the EPR are the ease of computation and minimal requirement of only two shoreline dates. It is a very great advantage in our case regarding the scarcity of satellite images over the chosen study area. This gives a rough idea of the average rate of which beach was swallowed during the last 20 years.

- **Linear Regression Rate (LRR)**

LRR is determined by fitting a least-squares regression line to all shoreline points for a transect (Figure 15.a). The regression line is placed so that the sum of the squared residuals (determined by squaring the offset distance of each data point from the regression line and adding the squared residuals together) is minimized. The LRR is the slope of this line. (Dolan et al., 1991; Crowell et al., 1997).

- **Weighted Linear regression Rate (WLR)**

For shorelines rate-of-change statistics, greater emphasis is placed on data points for which the position uncertainty is smaller. The Figure 15.b shows an example of the WLR calculation. The weight (w) is defined as a function of the variance in the uncertainty of the measurement (e) (Genz et al., 2007) and is given by the formula:

$$w = \frac{1}{e^2} \tag{8}$$

where e is the shoreline uncertainty value.

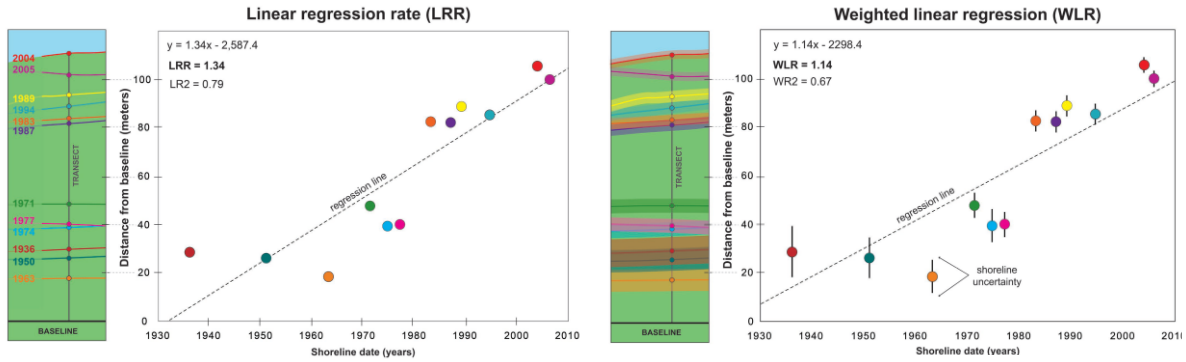

(a) (b)

Figure 15: LRR and WLR illustrations
Source: (Himmelstoss et al., 2021)

2.3.4.4. Shoreline forecast

The last subblock of the third block is the forecast block. The model used here to forecast the shorelines is the Kalman Filter (section 1.1.4.2.). This model is implemented in DSAS tool. The assumption here is the Business-as-Usual scenario. It means that the model assumes that the rates of shoreline change (derived few lines above) will be the same in the future. So, no special infrastructure is installed to prevent erosion or shoreline retreat.

The first step is the model parametrization. Then 10-year and 20-year forecast options were selected. In our case, both checkboxes were checked so both terms forecasts were performed to enable a very careful decision making.

The next step is to provide the forecast model inputs. The Kalman Filter is initialized by using the LRR calculated previously by DSAS. It is mandatory to have already run rate calculations that include a Linear Regression as one of the rate metrics computed. From this subblock, 2031 and 2041 shoreline positions and shape were then extracted. All the results were now compiled for further analysis and interpretation detailed in chapter 3.

2.3.4.5. Web application GEE

In order to develop the GEE application, the platform code editor was used to write a JavaScript code to define the interface, the buttons, widgets and actions (events) to perform when each button is clicked on. The result interfaces are presented in the chapter 3 (Results and discussion).

Chapter 3: Results and discussion

After applying the general methodology workflow and all its components, many results were obtained. In this chapter, the different results issued from the previous data processing described, were presented. The results are presented in a chronological order in such a way that they match with the different steps presented in the previous chapter. The results presentation is followed by a discussion section to highlight the interpretation of the main results.

Results

3.1.1. Testing models results

3.1.1.1. Performance testing of the 2 classifiers RF and SVM

The first result achieved was the comparative table of the accuracy indicators of the two classifiers (Table 5). Then the RF classifier was selected over the SVM one. RF was found to be more suitable than SVM for this binary Class1/Class2 classification using the features specified above. The choice was based on an analysis of Table 5. The choice is based also the comparative analysis of the result classified images (Figure 16). Details are provided about the choice in the discussion section (section 3.2.1.)

Table 5: Accuracy indicators for both RF & SVM

	Inputs (numbers)			Testing Indicators							
				TOA		TK		VOA		VK	
	Sample n	Training n	Testing n	RF	SVM	RF	SVM	RF	SVM	RF	SVM
2021	497	356	141	1.000	0.988	1.000	0.973	0.993	0.974	0.986	0.943
2016	500	360	140	1.000	0.997	1.000	0.993	0.993	0.993	0.984	0.984
2012	462	324	138	0.997	0.988	0.992	0.970	0.993	0.993	0.984	0.984
2006	487	346	141	1.000	0.991	1.000	0.980	0.993	0.993	0.984	0.984
2001	499	353	146	0.994	0.907	0.987	0.794	0.945	0.959	0.862	0.898

Where: TOA = Training Overall Accuracy; TK = Training Kappa; VOA = Validation Overall Accuracy; VK = Validation Kappa

3.1.1.2. Classification testing of the chosen RF Model

In this section, testing metrics were computed to assess the performance of the selected RF classifier model itself. The results are reported in Table 6. An Overall Accuracy of 63.16% and a kappa coefficient of 53.26% for year 2021, were obtained. This means that the RF classification performed globally well. The difference between the Overall Accuracy and the kappa coefficient was not too big. It means that few pixels were successfully classified due to chance factor.

Table 6: Accuracy assessment of the RF classifier (2021)

		Reference Values				
		Class 1	Class 2	Total	User's accuracy	
Classification Values	Class 1	**42**	25	67	62.69%	44.08%
	Class 2	31	**54**	85	63.53%	55.92%
	Total	73	79	152		
	Producers' Accuracy	57.53%	68.35%			
		48.03%	51.97%			
ACCURACY METRICS						
OA	63.16%					
CA	21.17%					
kappa	53.26%					

Where OA = Overall Accuracy; CA = Chance Agreement

3.1.2. Classified images

Using AI classification algorithms (RF and SVM classifier), the classified images were obtained for each of the selected 05 years (Figure 16). The choice of the RF algorithm (over the SVM one) to proceed with the methodology was also based on these classified images.

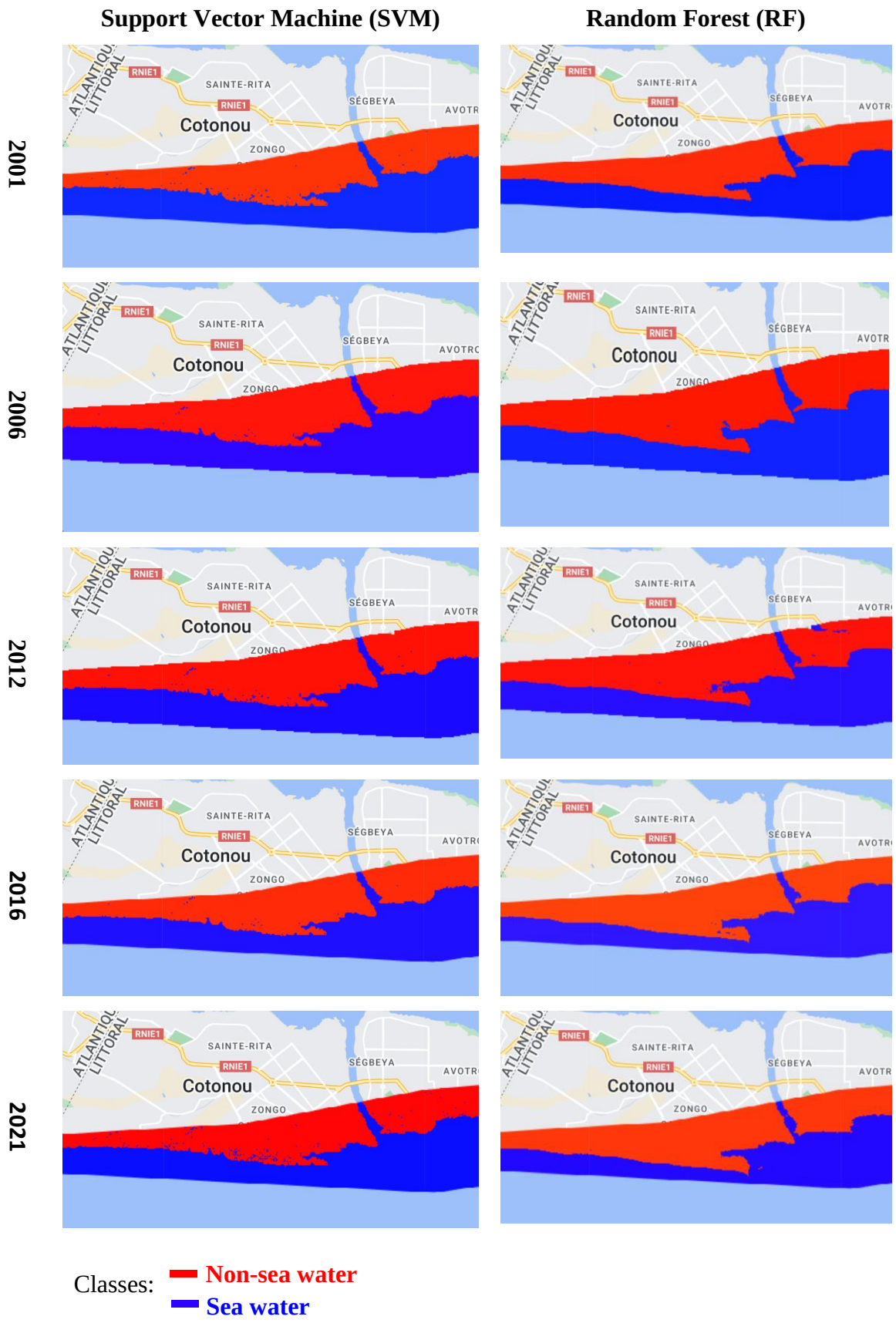

Figure 16: Classified images for both SVM and RF algorithms

It is important to notice that images of the year 2011 were either inexistent or unexploitable. They were replaced by the year 2012 which is most useable. Even 2012 images originally presented some gaps. It is due to a common error related to the dysfunction of the Sky Line Corrector (SLC) which occurred on the satellite Landsat 7 from 31st of May 2003. For this purpose, a gap correction using the ***focal_mean*** function in GEE, was developed in our code. This function applies a morphological mean filter to each band of an image using a named or custom kernel. Figure 17 shows for RF in 2012 classified images respectively at the top, the classified image without the fill-gap function (17.a) and at the bottom the classified image with applied fill-gap function (17.b).

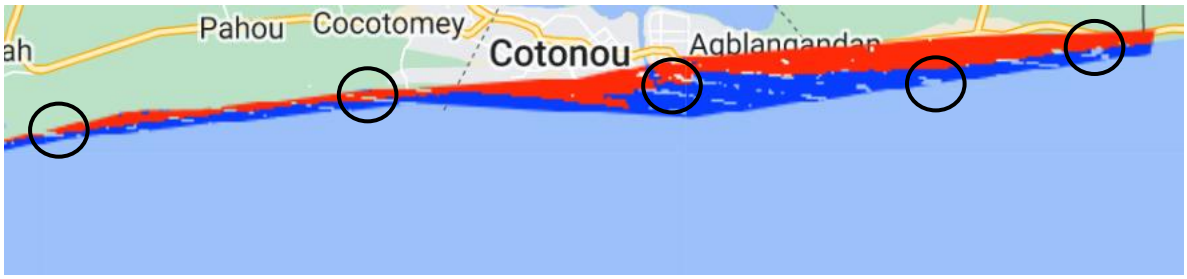

(a) 2012 classified image without correction

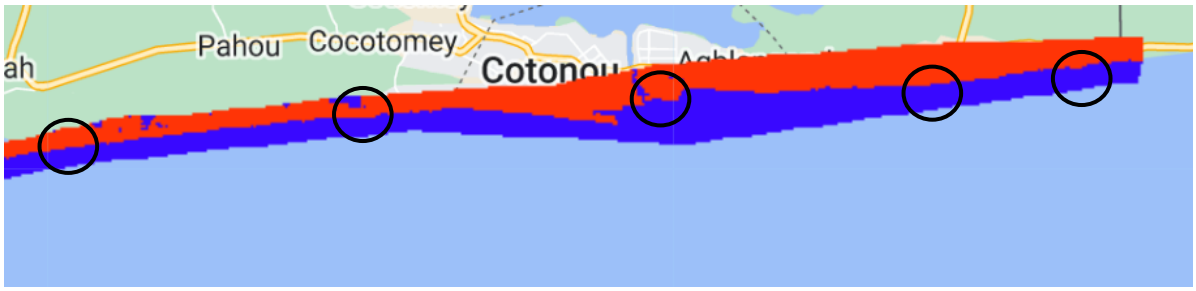

(b) 2012 classified image with correction

Figure 17: Applying fill_gap corrector function to 2012 image

3.1.3. Extracted historical shorelines

Through the proposed methodology, the historical shorelines respectively for the years 2001, 2006, 2012, 2016, and 2021, were reconstituted. Figure 18 shows the various shorelines for the corresponding years. The image was zoomed over the region located between the latitudes 7°4’23.16”N and 7°4’54.48”N on one hand and the longitudes 2°38’47.759”E and 2°39’59.072”E on the other, to make it more visible. At a larger scale the shorelines are confused.

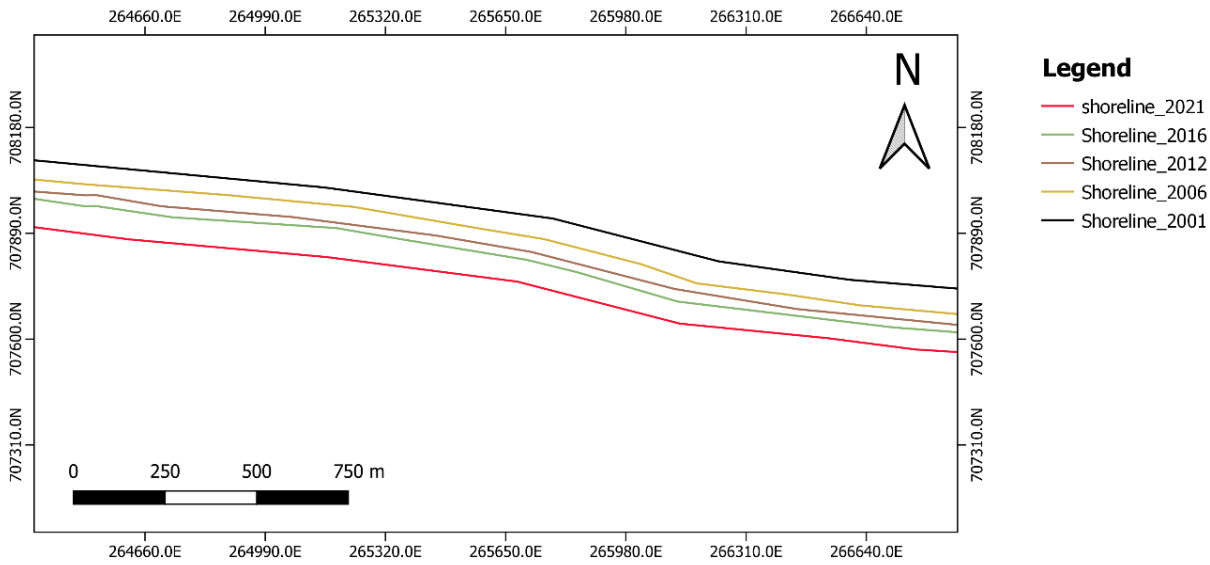

Figure 18: Extracted historical shorelines

3.1.4. Casted transects

After obtaining the 05 historical shorelines, the change rate indicators were computed. For that purpose, transects were casted all along the Benin Republic coast (Figure 19). The parametrization gives us a total of 132 casted transects. The background image used is a *hillshade* shapefile to emphasize the contrast with the transects. As specified above, the transects are spaced *1000 m* between each other. The image was zoomed out to cover a region between latitudes 6°52'47.64"N and 7°14'45.6"N on one hand and longitudes 1°45'18.0"E and 2°58'12"E on the other, to make all the study area transects visible.

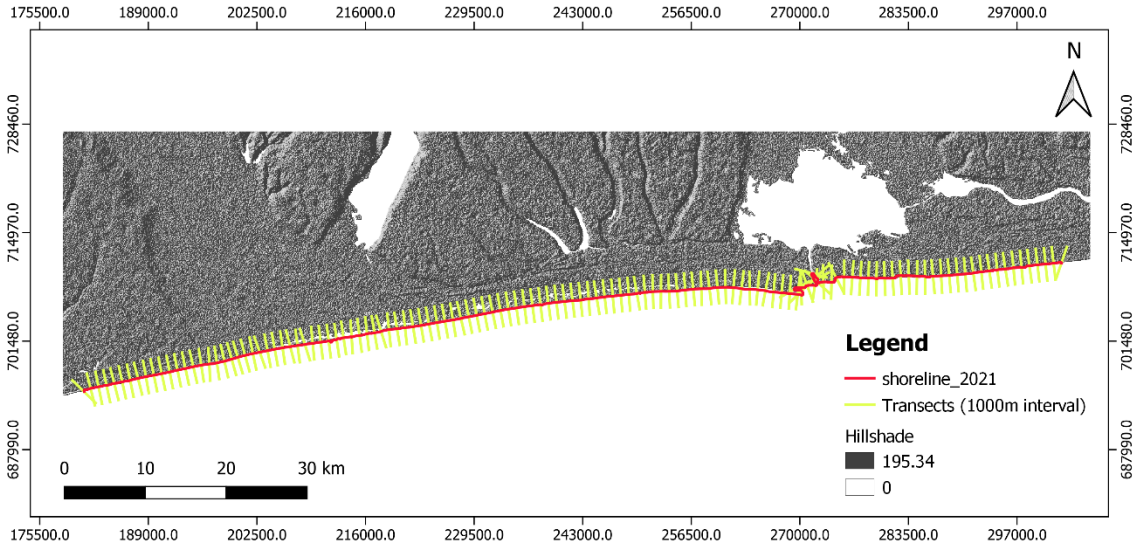

Figure 19: Transects applied on the whole study area

3.1.5. Computed change rate statistical indicators values

After casting transects, and running the DSAS tool, the different values of the change rate indicators were computed. In Appendix 3, the whole table for all indicators was provided and also the summary reported provided by DSAS. Two types of statistical indicators are computed. The first one is NSM, which is a net value. Details concerning the NSM indicator were provided some lines above (section 2.3.4.3). Table 6 gives the summary of the main values of the NSM statistical indicators.

Table 7: NSM statistics summary

Rate indicator	**NSM**
Total Number of transects	**132**
Average Distance (m)	**-31.41**
Percentage of transects with negative distance (%)	**62.88**
Maximum negative distance (m)	**-1997.2**
Maximum negative distance Transect ID	**97**
Average of all negative distances (m)	**-63.21**
Percentage of transects with positive distance (%)	**37.12**
Maximum positive distance (m)	**167.05**
Maximum positive distance Transect ID	**112**
Average of all positive distances (m)	**22.45**

EPR, LRR, and WLR, which are rates (% values), were also computed as well. The main statistics of these 3 indicators, were chosen to be reported. The summary of the results of the 03 change rate statistics is reported in Table 7. Table 7 is analyzed further in discussion paragraph. All the statistical indicators values were subset from the great change rate datasets and the summary report provided directly by DSAS after running.

Table 8: EPR, LRR and WLR statistics

Rate indicator	**EPR**	**LRR**	**WLR**
Total Number of transects	**132**	**132**	**132**
Average rate ± reduced n uncertainty (m/yr)	**-2.17±0.28**	**-1.51±1.68**	**-2.73±8.68**
Percentage of erosional transects (%)	**62.88**	**54.96**	**66.41**
Maximum value erosion (m/yr)	**-133.15**	**-120.06**	**-201.65**
Maximum value erosion Transect ID	**97**	**97**	**97**
Average of all erosional rates (m/yr)	**-4.34**	**-4.31**	**-5.71**
Percentage of accretional transects (%)	**37.12**	**45.04**	**33.59**
Maximum value accretion (m/yr)	**11.14**	**20.38**	**44.53**
Maximum value accretion Transect ID	**112**	**92**	**92**
Average of all accretional rates (m/yr)	**1.5**	**1.92**	**3.17**

3.1.6. Shoreline forecasts

The obtained shoreline horizon forecasts (10 and 20 years) are displayed as a polyline feature class. They represent the forecasted location of the shoreline at the selected time frame. The forecasted shoreline horizon line is displayed with the associated shoreline forecast uncertainty. The shoreline forecast uncertainty (10 and 20 years) displayed as a transparent polygon feature class, can be considered as the band of uncertainty for the forecasted shoreline horizon line. The 10-year (Figure 19.a) and 20-year (Figure 19.b) forecast were individually illustrated in order to highlight in a suitable way the same confidence interval (90%) respectively associated with each one of them.

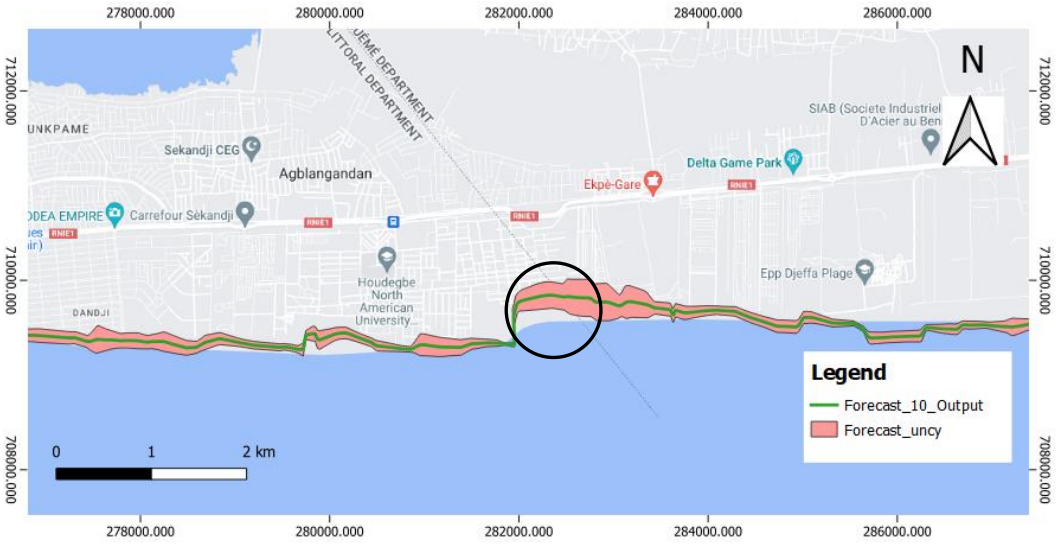

(a)

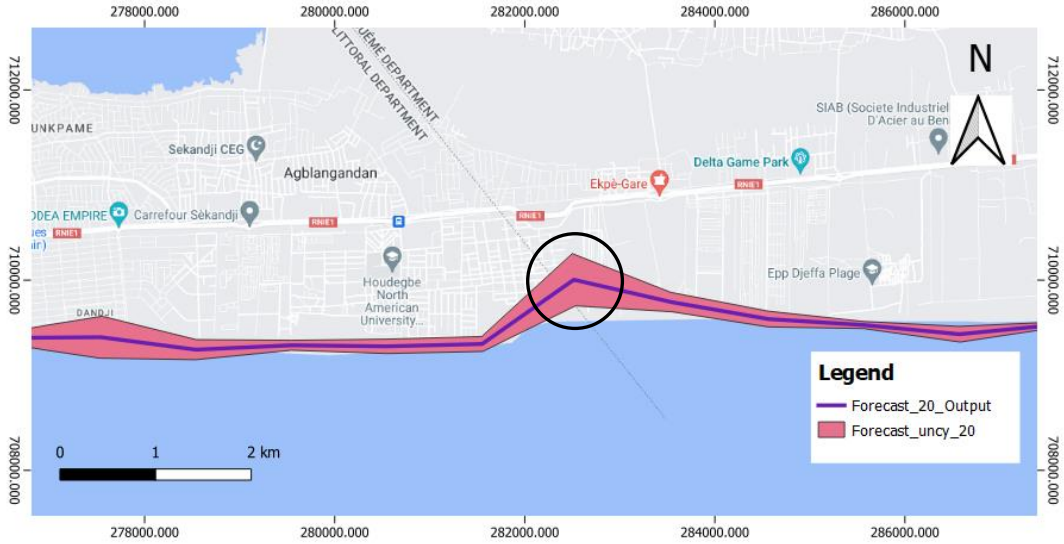

(b)

Figure 20: Obtained forecast of shorelines

3.1.7. The Web application: BenShoreApp

In order to provide an easy access and visualization of our results, a GEE web application was designed and implemented. The solution was named "BenShoreApp" and is available on URL: https://david91.users.earthengine.app/view/benshoreapp. This solution is meant to help decision makers and non-expert targets to be aware of the severe erosion impacts caused by Climate Change along Benin Republic coast, and to take anticipatory measures. In this section, the main functionalities of the application are described.

3.1.7.1. Homepage

When the user types the required URL, he is automatically redirected to the home page of the application (Figure 21). The homepage presents 06 buttons. Each button was labeled explicitly such a way that the label corresponds to a specific functionality. The *Zoom*, *Places Search* and *Plan/Satellite View* original functionalities of GEE are conserved in the application.

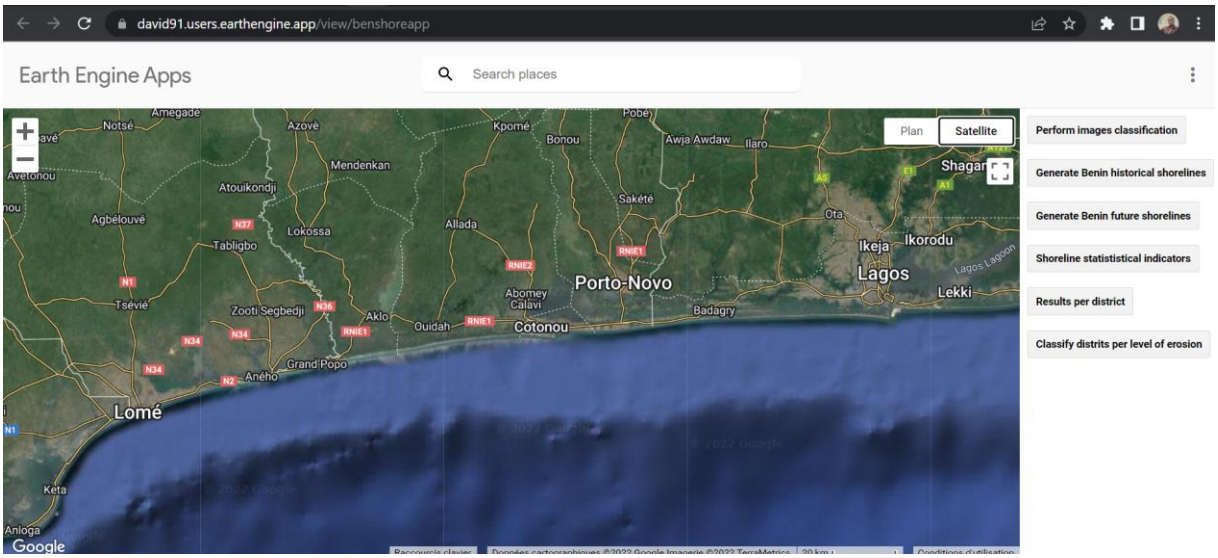

Figure 21: Homepage of the web application

3.1.7.2. "Perform images classification" button

When the user clicks on the "Perform images classification" button, the system runs the RF image classifier model background (importing all the required assets for the computation) and automatically shows finally the RF classified image of each of the 5 years of the study period. Figure 22 shows an example of "Perform images classification" use case.

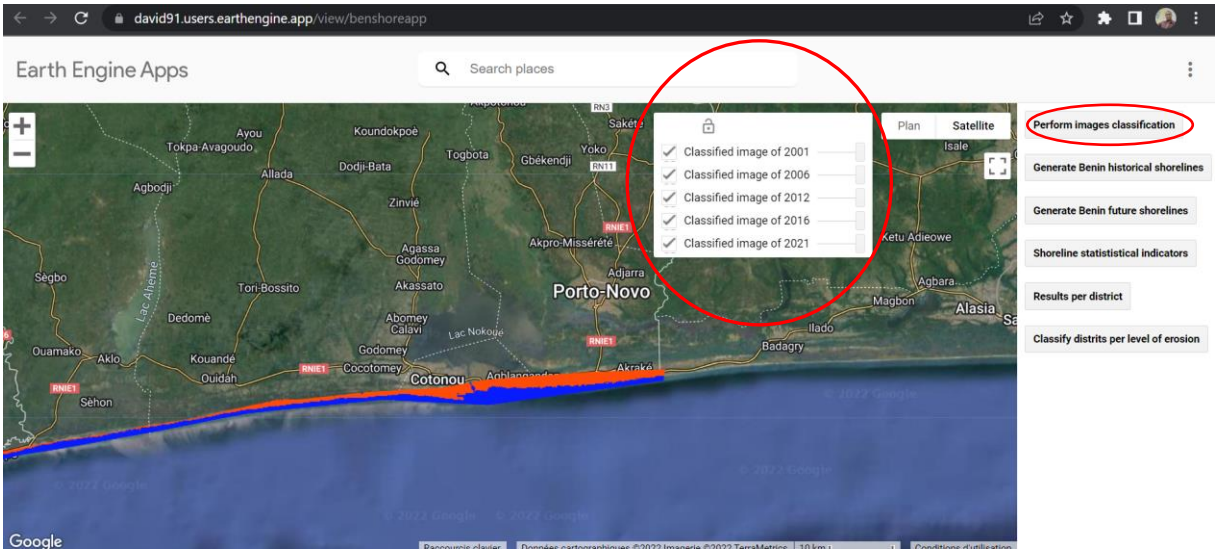

Figure 22: "Perform images classification" button results interface

3.1.7.3. "Generate Benin historical shorelines" button

When the user clicks on the "Generate Benin historical shorelines" button, the system automatically displays the 05 historical shorelines extracted from the 05 classified images obtained with the previous button. Figure 23 shows an example of the "Generate Benin historical shorelines" use case. Different colors are arbitrary assigned to the different shorelines to distinguish them: dark green (2001), yellow (2006), black (2012), purple (2016), and pink (2021).

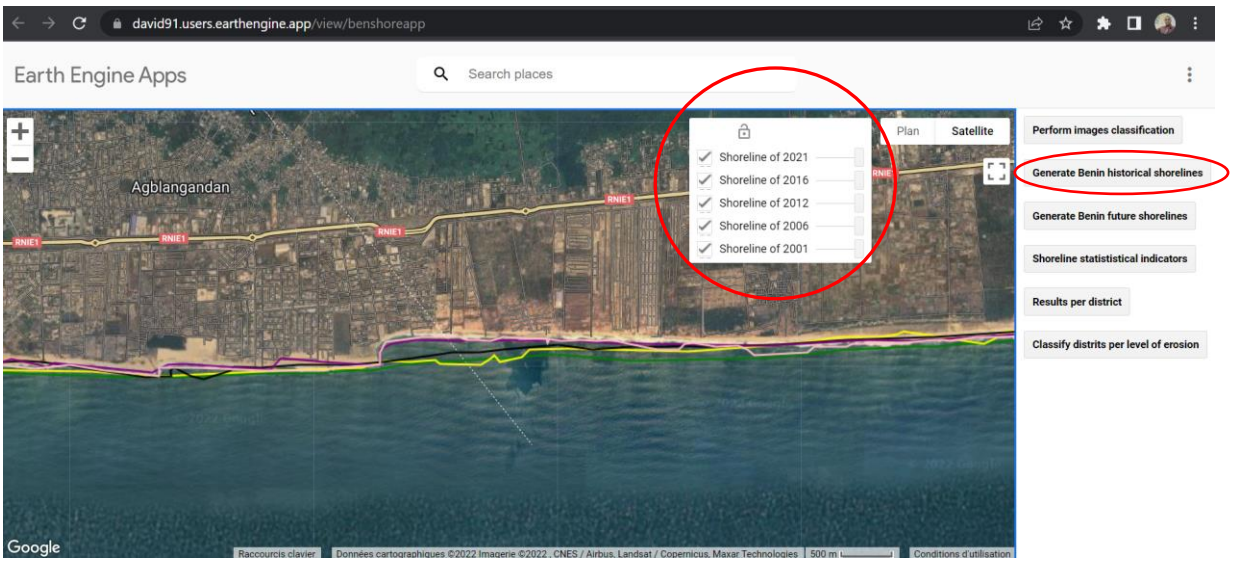

Figure 23: "Generate Benin historical shorelines" results interface

3.1.7.4. "Generate Benin future shorelines" button

When the user clicks on the "Generate Benin future shorelines" button, the system automatically displays the 02 future shorelines forecasted previously with DSAS plugin. Figure 24 shows an example of the "Generate Benin future shorelines" use case. 02 different colors are arbitrary assigned to the different shorelines to distinguish them: blue (2031), red (2041).

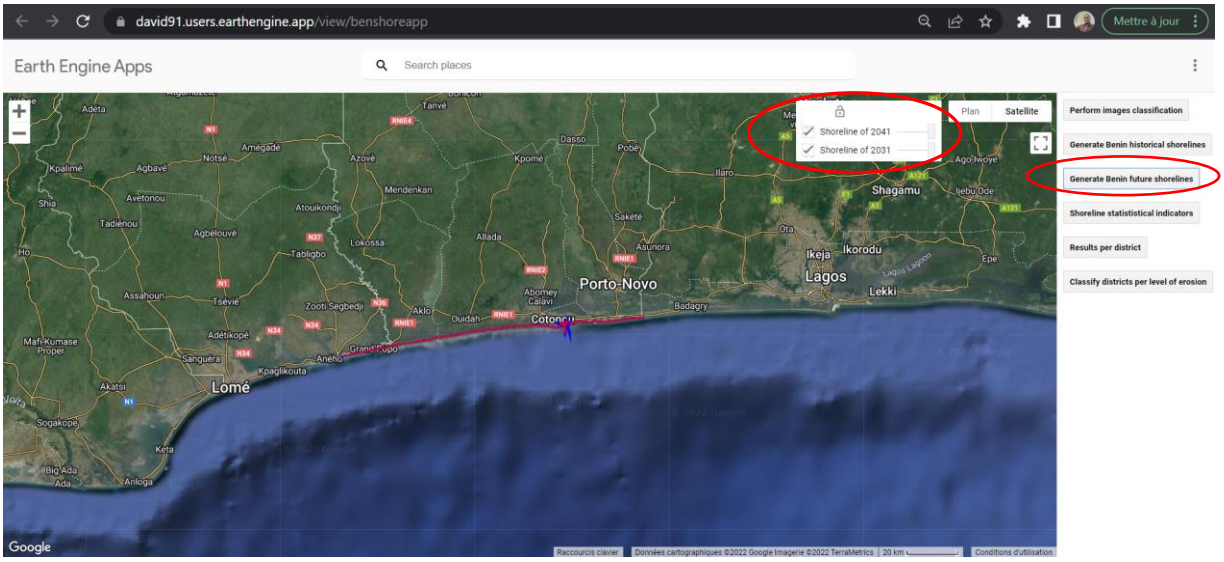

Figure 24: "Generate Benin future shorelines" results interface

3.1.7.5. "Shoreline statistical indicators"

When the user clicks on the "Shoreline statistical indicators" button, the system automatically creates and displays a left panel, allowing him to choose the type of indicator he wants to display the charts. Figure 25 shows an example of the use case of the EPR statistical indicator plots display. All the displayed plots are zoomable and interactive. Each of the transect can be selected to see the value of the indicator and the number of the transect. It allows the user to identify at glance, the extreme values and the outliers of the series.

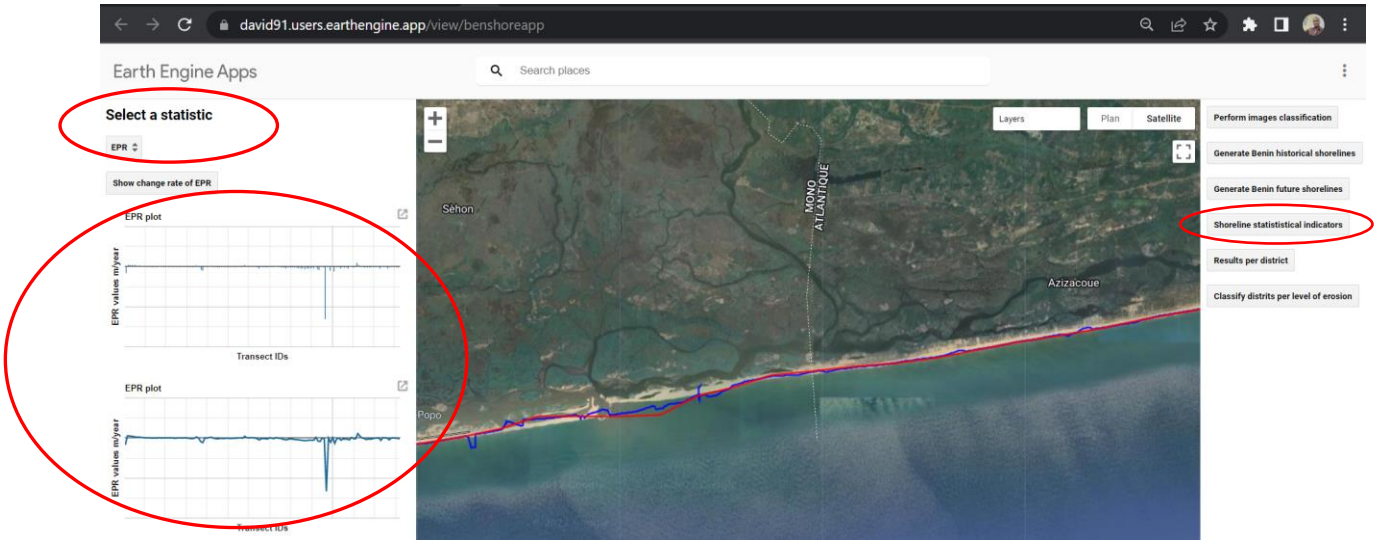

Figure 25: "Shoreline statistical indicators" results interface

3.1.7.6. "Results per district" button

The "Results per district" button allows the user to zoom automatically to one of the 05 coastal districts of Benin Republic. It helps the decision maker or the non-expert to focus directly visualize the erosion and accretion change on a particular district on the coast of Benin.

3.1.7.7. "Classify district per level of erosion" button

When the user clicks on the "Classify district per level of erosion" button, the system automatically displays a classification of the 05 coastal districts in a growing order of erosion impact, from the least to the most affected district (Figure 26). The district classification prompts with a legend box to distinguish the different classes of erosion impacts: dark green (Least eroded), light green (Fairly eroded), yellow (Eroded), orange (Strongly eroded), red (Most eroded).

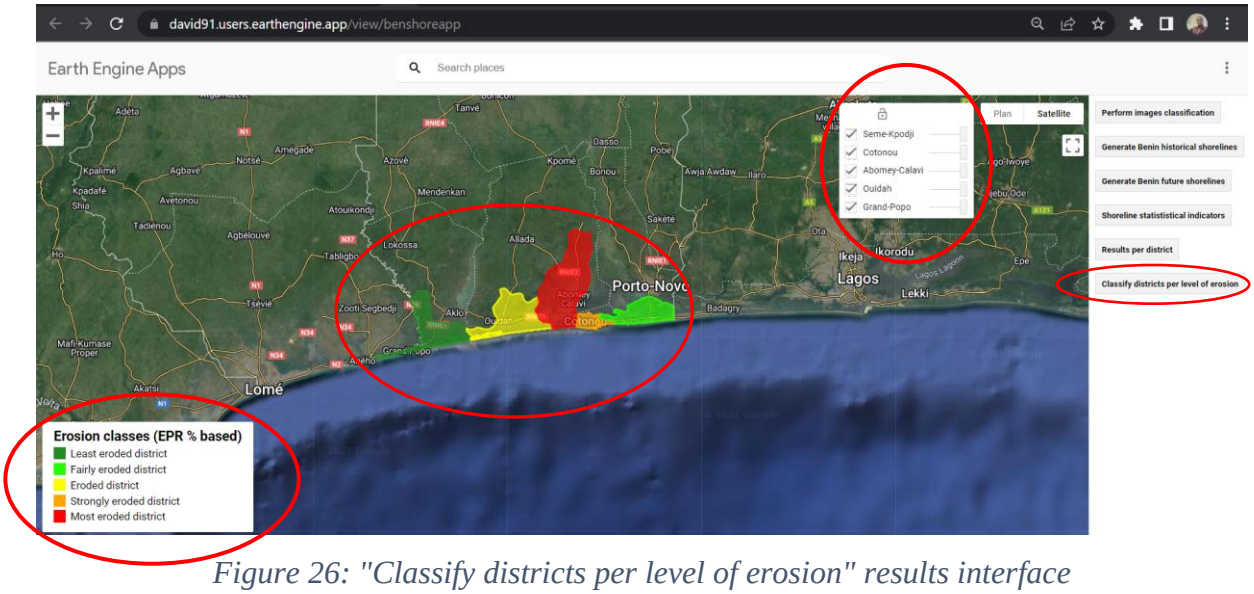

Figure 26: "Classify districts per level of erosion" results interface

Analysis and Discussion

In this section, the main results previously presented are analyzed and then discussed. The discussion is also presented in a chronological order.

3.1.8. Choice of RF classifier

Some reasons led us to choose RF classifier over SVM one. The first one is the validation indicators assessment. Indeed, Table 5 retraces the different validation indicators for the two classifiers. For all the years, it is visible that the TOA is greater for RF than for SVM, meaning that the Training Overall Accuracy is better in the RF classifier case. For the years 2021 and 2016, the TOA is up to 1 (approximately). In terms of TK, the remark is also the same. This means that RF classifier was better trained (with more samples considered) than the SVM one. Considering VOA and VK, none of the values of VOA and VK are up to 1. However, only for year 2001, SVM values of VOA and values of VK are greater than RF ones. In all the other cases, RF values are still better (closer to 1 than SVM ones).

The second reason is the quick visual analysis of the classified images from the two classifiers. In fact, the analysis was pursued up to display the classified images from the two algorithms (Figure 16). It appears that the RF result images are most exploitable than SVM ones. The two previous listed reasons, added to the fact that RF is widely used in the literature in terms of image classification, were our motivations to choose RF over SVM to proceed in the work.

Our results are in the same vein with those of (Adugna et al., 2022) who found that RF outperformed SVM yielding 0.86 (Overall Accuracy) and 0.83 (Validation kappa), which are 1-2% and 3% higher than the best SVM model, respectively. These also confirm the findings of (Sheykhmousa et al., 2020) which is that the maximum average accuracy is achieved with RF for Land Use Land Cover (LULC) with approximately 95.5% and change detection with about 93.5% for SVM classification.

3.1.9. Analysis of the change rate statistical indicators

Our analysis was based on the summary table (Table 8), and 03 kinds of data visualizations: the bar plot, the trend curve and the indicator mapping over the whole study area. The analysis was done per indicator.

3.1.9.1. NSM results analysis

The first indicator addressed is the NSM. At a first glance, for a total of 132 generated transects, the average distance of which the shoreline has moved over the past 20 years is -31

m. The minus sign is to emphasize that it is an inland movement. This is an average over the whole study area. The maximum negative distance is obtained at transect no 97 and is up to -1997.2 m, almost 2 km. This is quickly highlighted on Figure 27 which shows the NSM bar diagram over the whole study area. This value caught our attention. Then by overlaying a base map (Google maps), this transect was identified as located in the Port of Cotonou.

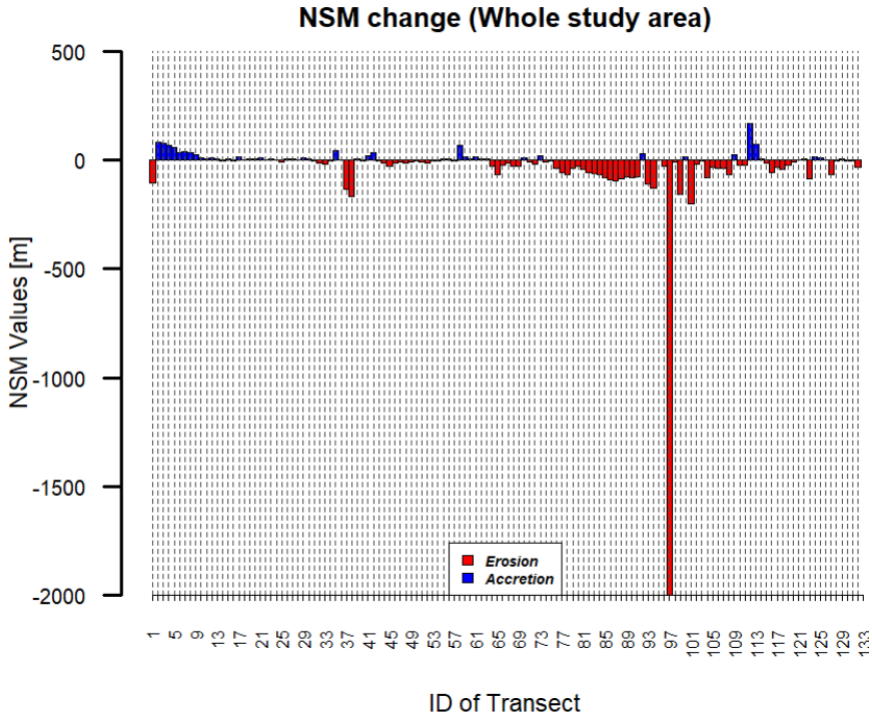

Figure 27: NSM histogram on the whole study area

Due to the complexity of this zone (artificial shoreline, man-made activities), to deepen the analysis, the study area was (longitudinally) split in two cells excluding Transect no. 97. This methodology was based on the study of (Assogba, 2018). Cell 1 covers the Benin Republic Coast line between latitudes 1°37'32"E and 2°26'36"E while Cell 2 covers it from 2°26'55"E to 2°42'44"E. The further analysis for all the indicators, are performed on the whole study area, and both on Cells 1 and 2. In the case of the NSM indicator, Figure 28 shows the bar diagrams for Cell 1 (resp. (a)) and Cell 2 (resp. (b)).

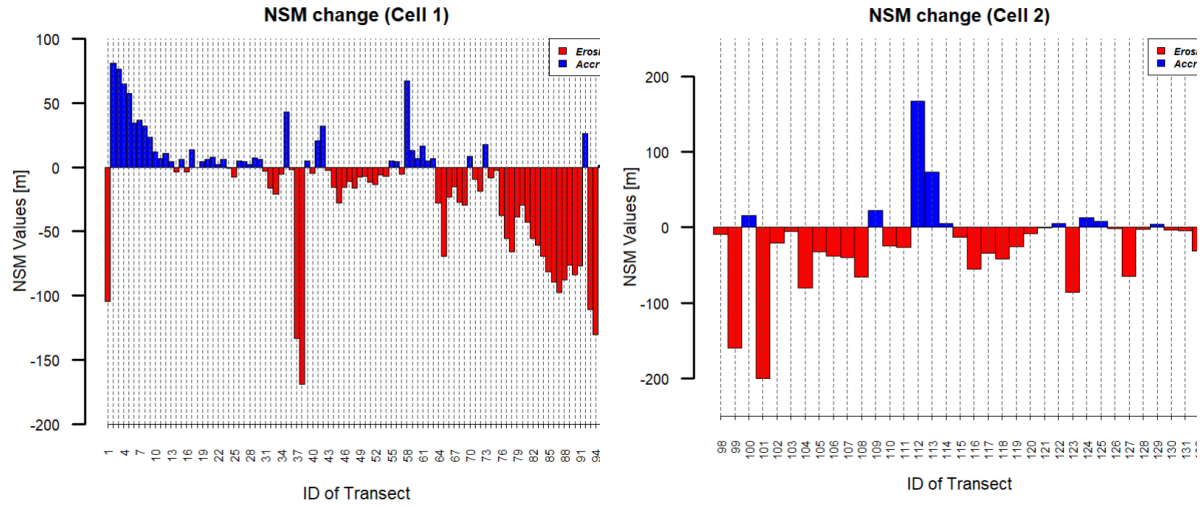

(a) (b)

Figure 28: NSM histogram on cell 1 and on cell 2

Then, the new highest negative value (which is not in the area of the Port of Cotonou) of NSM of both Cell 1 and Cell 2 is -169.94 ± 10 m, located in Cell 1 at Transect no. 38. This transect is located in the department of Mono, the district of Grand Popo, in the sector of Avloh and the locality "Nakoue plage", more exactly 3.78 km far before the famous beach place called "Embouchure du Roy", coming from the district of Ouidah (Figure 29). It means that this location is the most affected by erosion in terms of NSM.

The highest positive value of NSM was 167.05 m, at the Transect no. 112. It falls in the department of Oueme, precisely in the town of Ekpe.

Next, all the NSM values were plotted on the whole study area to do a mapping of how NSM is spatially distributed over it. This led us to Figure 30. 09 classes of NSM were identified. The NSM values vary from the highest negative NSM (red color) to the highest positive ones (blue color). It appears from Figure 30 that the district of Littoral is the one which underwent a high NSM spatial density over the last 20 years.

Figure 29: Localization of the highest NSM erosion

On Figure 30, 03 important red color transects are identified there especially in the sector of Fidjrosse around the airport. It is followed by the district of Abomey-Calavi, especially in the sector of Godomey where 03 orange transects were found. Some little parts of the town of Grand Popo are also affected by NSM especially 02 red transects (among which the highest NSM previously discussed).

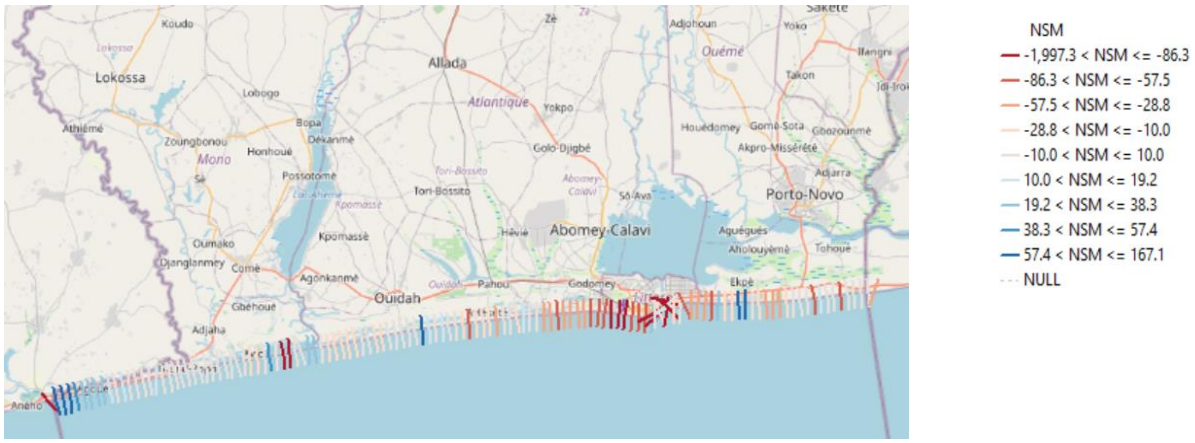

Figure 30: NSM mapping over Benin Republic coast

In terms of backward shoreline retreat, Hillacondji, and Ekpe are the locations where an important density of “blue” transects was found with around 04 “blue” transects. It means that these locations experience high Net Shoreline backward movement (accretion) over the last 20 years.

3.1.9.2. EPR results analysis

The second indicator addressed is the EPR. At a first glance, for a total of 132 generated transects, the average EPR of which the shoreline has changed over the last 20 years is -2.17 m/year with an uncertainty of ±0.28 m/year. The uncertainty here is relatively weak showing that the EPR was calculated with a high accuracy. The minus sign is to emphasize that it is a forward inland movement over the whole study area. The maximum negative EPR is obtained at transect no. 97 and is up to -133.15 m/year. Thus, for the same reasons as for NSM, the same methodology of analysis was conducted here. Figure 31 shows the EPR bar diagram over the whole study area.

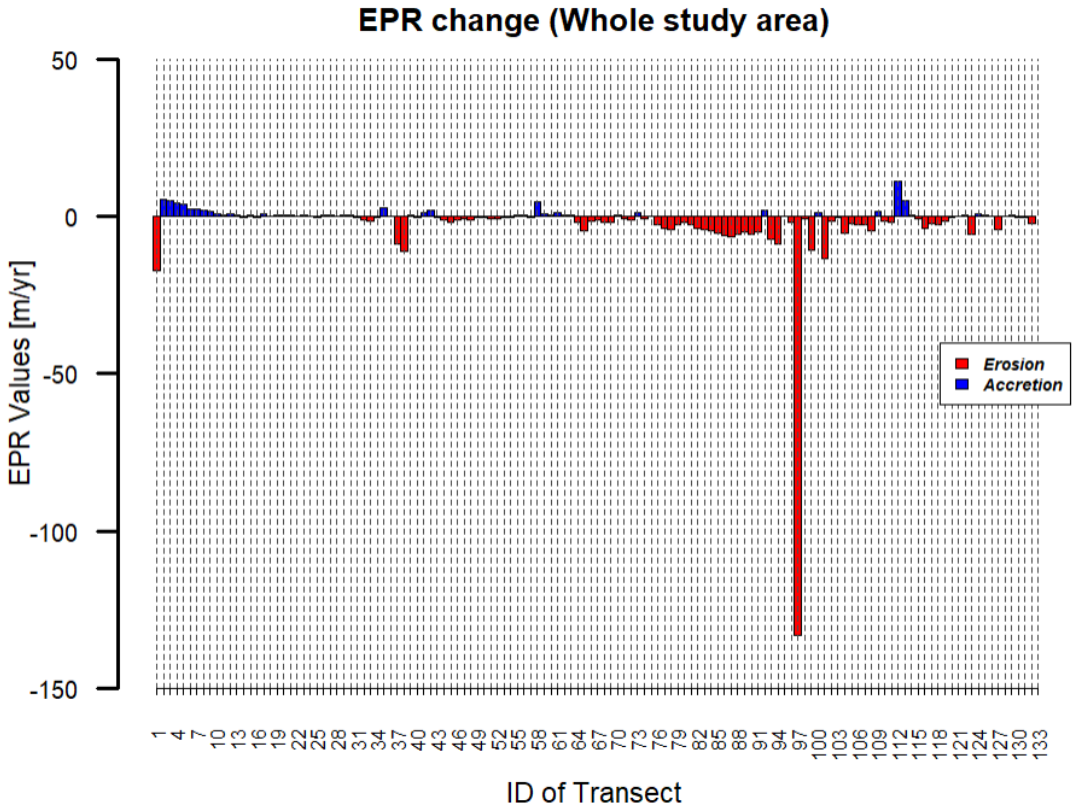

Figure 31: EPR histogram on the whole study area

Globally, it can be observed more eroded transects (~63%) than the accreted ones (~37%) on the whole study area clearly showing an erosion trend. In the case of the EPR indicator, Figure 32 shows the bar diagrams for Cell 1 (resp. (a)) and Cell 2 (resp. (b)).

The highest negative value (which is not in the area of the Port of Cotonou) of EPR of both Cell 1 and Cell 2 is -17.40 m/year, located in Cell 1 at Transect no. 1. This transect is located in the department of Mono, the district of Grand Popo, in the sector of Agoue and the locality Hillacondji, more precisely at the border Benin-Togo.

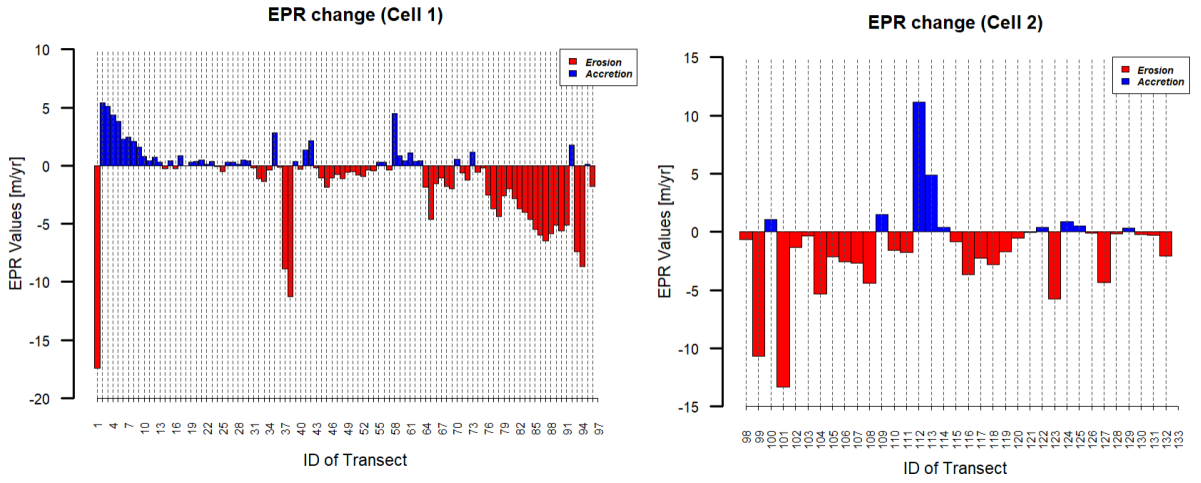

(a) (b)

Figure 32: EPR histogram on Cell 1 and on Cell 2

This locality is followed by the locality of Fidjrosse (Transect 37) around the airport of Cotonou which also experienced a high EPR.

The highest positive value of EPR is 11.14 m/year at the Transect no. 112. This transect location has already been discussed above. It means that in terms of EPR, the locality of Ekpe is also the one experiencing the highest accretion.

Next, all the EPR values were plotted on the whole study area to do the mapping of how EPR is spatially distributed over it. This led us to Figure 33. 09 classes of EPR were identified. The EPR values vary from the highest negative EPR (red color) to the highest positive ones (blue color). It appears from Figure 33 that the department of Littoral is the one which underwent a high EPR spatial density over the last 20 years.

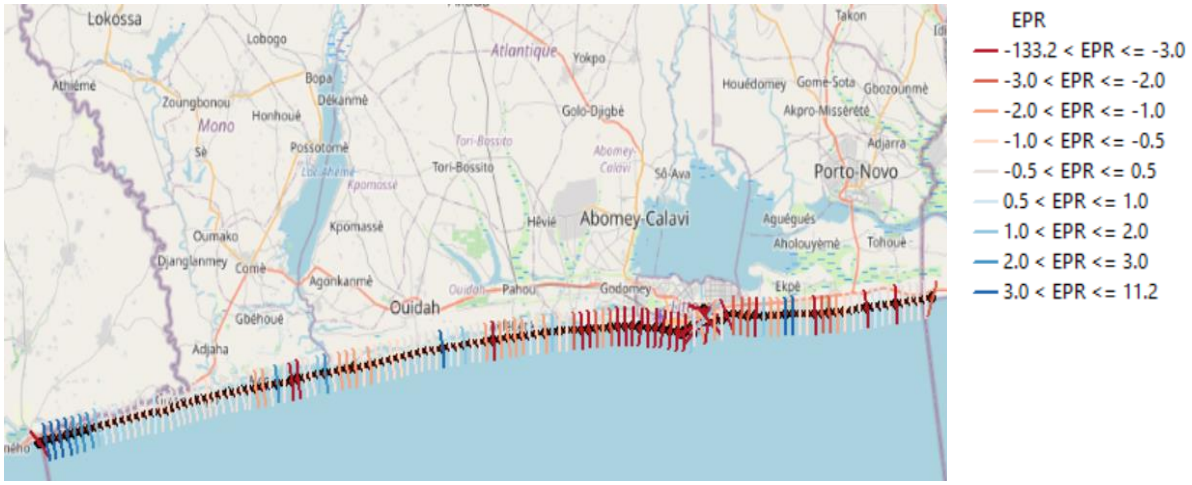

Figure 33: EPR mapping over Benin Republic coast

On Figure 33, 03 important red color transects are also identified there especially in the sector of Fidjrosse around the airport. It is followed by the district of Abomey-Calavi, especially

in the sector of Godomey where 03 "orange" transects can be found. This transects distribution is similar to the NSM ones in terms of erosion. However, in terms of accretion, there are some significant differences. A higher density of EPR can be observed in the locality of Djondji in the district of Ouidah and most at in the Benin -Togo border localities Hillacondji and Agoue, in the district of Grand-Popo. A minimum of 07 "blue" transects was recorded in this area, meaning that these two locations experience high accretion in terms of EPR from 2001 to 2021.

3.1.9.3. LRR results analysis

The third indicator used was the LRR. For a total of 132 generated transects by DSAS, the average LRR of which the shoreline has changed for the study time range is -1.51 m/year. with an uncertainty of ±1.68 m/year. The uncertainty here is still weak but more important than the EPR one. So, the calculation was made with an acceptable accuracy. The maximum negative LRR is obtained at Transect no. 97 as expected, and is up to -120.06 m/year. Figure 34 shows the LRR bar diagram over the whole study area.

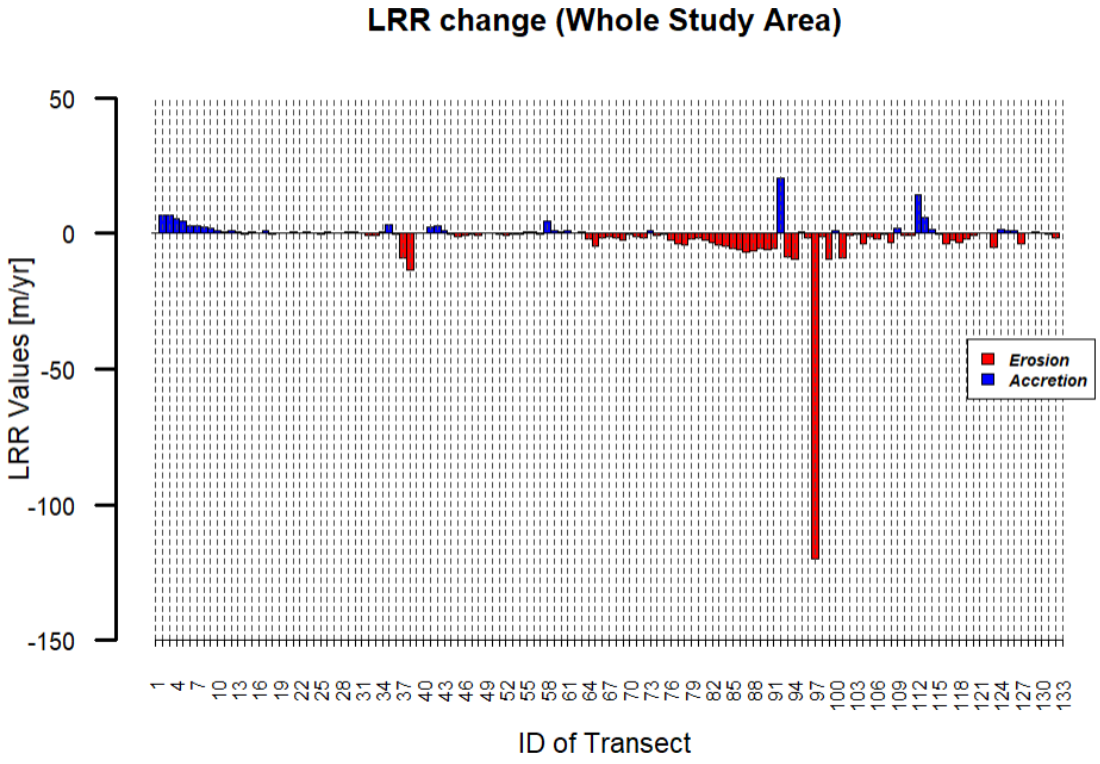

Figure 34: LRR histogram on the whole study area

Globally, it can be observed more erosion erosional (~55%) transects than accretional ones (~45%), but the percentage is more balanced than EPR's one. In this case again, the study area was split in two. Figure 35 shows the LRR bar diagrams for Cell 1 (resp. (a)) and Cell 2 (resp. (b)).

The highest negative value (which is not in the area of the Port of Cotonou) of LRR of both Cell 1 and Cell 2 is -13.65 m/year, located in Cell 1 at Transect no. 38. This transect has already be discussed previously (section 3.2.2.1). It means that the locality of Fidjrosse, around the airport of Cotonou, also experienced a high LRR over time.

The highest positive value of LRR is 14.09 m/year at the Transect no. 112. This transect has already be discussed previously. It means that in terms of LRR, the locality of Ekpe is also experiencing the highest accretion.

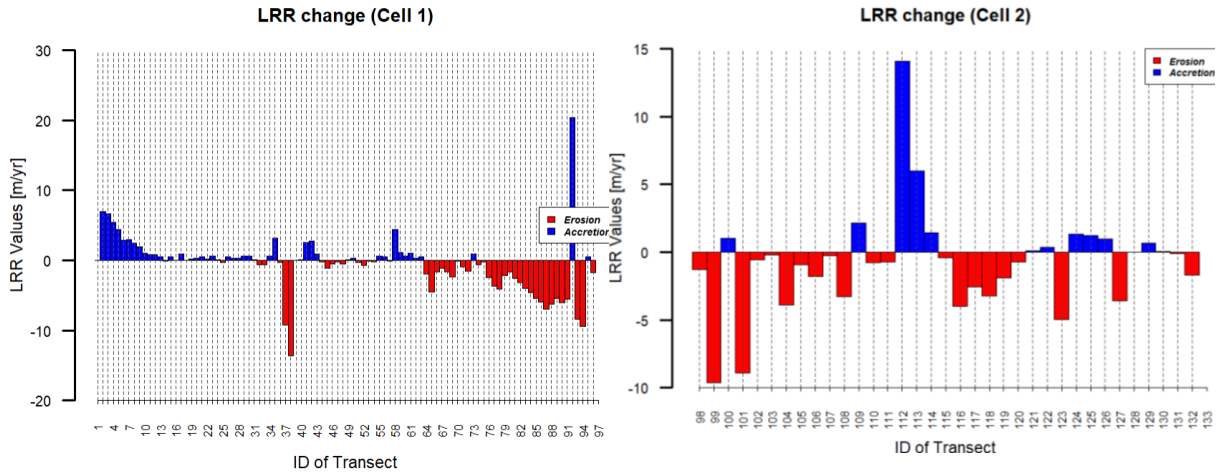

(a) (b)

Figure 35: LRR histogram on Cell 1 and on Cell 2

Next, all the LRR values were plotted on the whole study area to do a mapping of how LRR is spatially distributed over it. This led us to Figure 36. 09 classes of LRR were also identified according to some thresholds. It appears from Figure 36 that the department of Littoral is the one which underwent a high LRR spatial density over the last 20 years. Here, in the same sector of Fidjrosse around the airport, only 02 “red” transects were identified. But the difference here is that it is followed by the district of Grand Popo, especially in the sector of Avloh where 02 other “red” transects can be found. This transects distribution is slightly different from the 02 first ones.

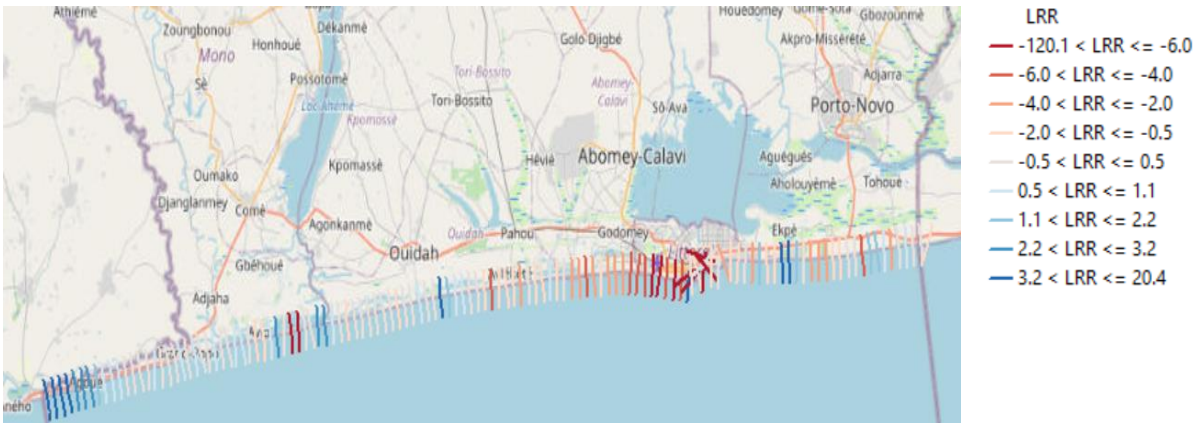

Figure 36: LRR mapping over Benin Republic coast

Considering accretion, the same high "blue" LRR transects density can be observed in the localities of Hillacondji (Grand-Popo) and Ekpe (Seme-Kpodji). It was recorded a minimum of 07 "blue" transects in the first locality and 02 in the second one, meaning that these two locations underwent high accretion in terms of LRR from 2001 to 2021.

3.1.9.4. WLR results analysis

The last indicator computed was the WLR. It is the Weighted LRR as explained in the previous chapter (section 2.3.4.3). For a total of 132 generated transects by DSAS, the average WLR of which the shoreline has changed for the study time range, is -2.73 m/year. with an uncertainty of ±8.68 m/year. The uncertainty here is now enough important than the LRR one. It can be explained by the fact that the LRR uncertainty has been also weighted to calculate the WLR. So, the calculation was made with more or less, a weak accuracy. The maximum negative WLR is to -201.65 m/year (Transect no. 97). Figure 37 shows the WLR bar diagram over the whole study area. Globally, more erosion erosional (~66%) transects than accretional ones (~34%) was observed. Here, the difference between erosion and accretion rates has been accentuated again as for EPR. This confirms the erosion trend.

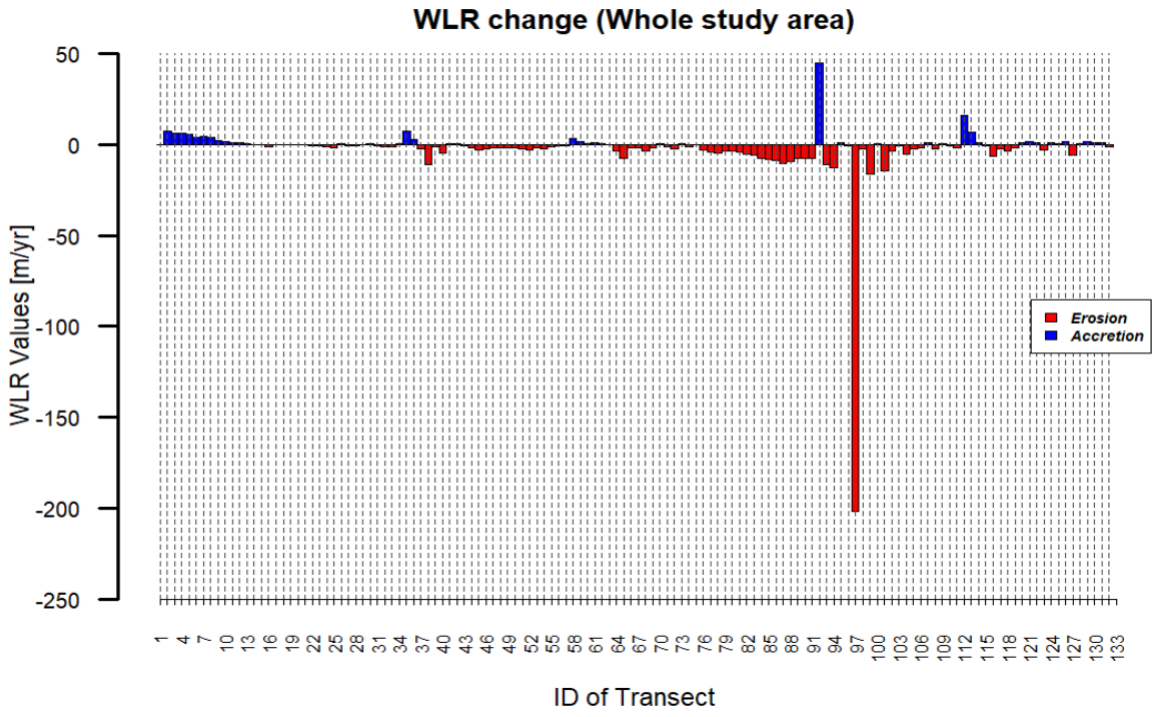

Figure 37: WLR histogram on the whole study area

In this case again, the study area was split in two. Figure 38 shows the WLR bar diagrams for Cell 1 (resp. (a)) and Cell 2 (resp. (b)).

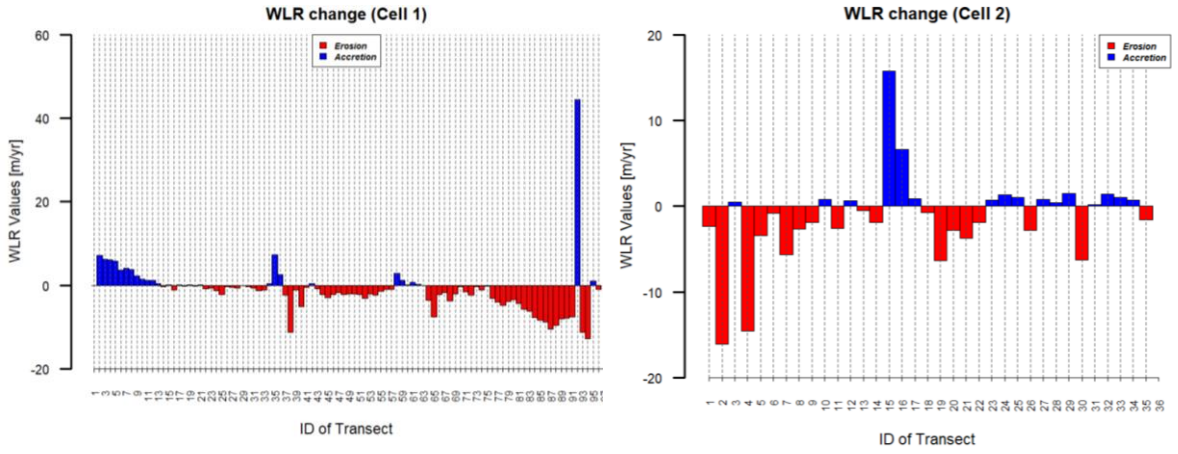

(a) (b)

Figure 38: WLR histogram on Cell 1 and on Cell 2

The highest negative value (which is not in the area of the Port of Cotonou) of WLR of both Cell 1 and Cell 2 is -11.19 m/year, located in Cell 1 at Transect no. 38. This transect has already be discussed previously (section 3.2.2.1). It means that the locality of Fidjrosse, around the airport of Cotonou which also experienced a high WLR over the study period.

The highest positive value of LRR is 15.79 m/year at the Transect no. 112. This transect has already be discussed previously. It means that in terms of WLR, the locality of Ekpe is also

the one experiencing the highest accretion.

Next, all the WLR values were plotted on the whole study area to do a mapping of how WLR is spatially distributed over it. This led us to Figure 39. 09 classes of WLR were also identified according to some thresholds. It appears from Figure 39 that the department of Littoral is the one which underwent a high WLR spatial density for the study period. Here, in the same sector of Fidjrosse around the airport, 06 "red" transects were identified. This highlights the fact that this area is dangerously eroded. The difference here is that it is not followed by any second district undergoing the same kind of erosion rate. This transects spatial distribution is different from the 03 first ones.

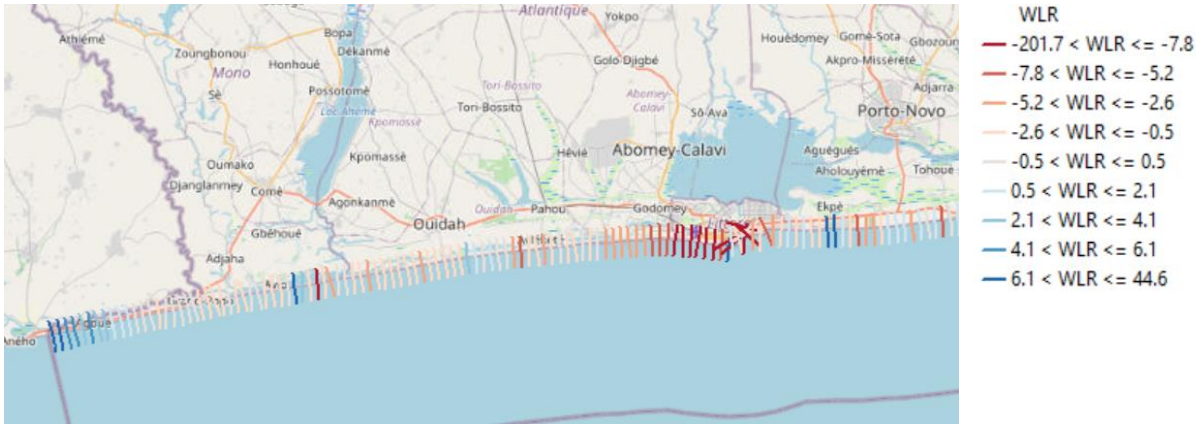

Figure 39: WLR mapping over Benin Republic coast

Considering WLR accretion, the high "blue" LRR transects density can be observed in the localities of Hillacondji (Grand-Popo) and Ekpe (Seme-Kpodji). But the difference here, is that 05 "blue" transects were recorded in the first locality and only 02 in the second, meaning that these 02 locations underwent high accretion in terms of WLR from 2001 to 2021. Finally, the study area split allowed us to examine the shoreline dynamics per Cell. The maximum rates per cell, are summarized in Table 9.

Table 9: Shoreline dynamics comparison between Cell 1 and Cell 2

	Cell 1				Cell 2			
	Erosion		***Accretion***		***Erosion***		***Accretion***	
	Max	Percent	Max	Percent	Max	Percent	Max	Percent
NSM [m]	-169.02	58.33%	81.07	**41.67%**	-199.94	**74.29%**	167.05	25.71%
EPR [m/year]	-17.40	57.29%	5.40	**42.71%**	-2.15	**71.43%**	11.14	28.57%
LRR [m/year]	-13.65	51.04%	20.38	**48.96%**	-9.66	**62.86%**	14.09	37.14%
WLR [m/year]	-12.74	67.71%	44.53	32.29%	-16.07	54.29%	15.69	45.71%

A quick analysis of Table 9 shows that over the last 20 years, Cell 2 has been more affected by shoreline retreat than Cell 1 while in terms of accretion, Cell 1 was more concerned than Cell 2. This result is in line with the results of (Assogba, 2018; Degbe, 2017) who both found that the erosion is more accentuated at the East side of the Port infrastructure. These results are also in concordance with those of (Yang et al., 2021) which revealed that shoreline in Cell 1 showing accretion by recovering 1.20 km^2 of surface area and in contrast, 3.67 km2 of Cell 2 disappeared due to coastal erosion, although it has groynes for protection against erosion.

Concerning the localities, Hillacondji (Grand-Popo) is the locality experiencing more accretion in Cell 1 and the localities of Fidjrosse (Cotonou), Ganhi (Cotonou) are the ones experiencing more erosion in Cell 1. This can be explained by the inefficiency of the infrastructure installed against erosion since 1962 at the East side of the Port (known as the groynes of Siafato) by the government of Benin Republic and which has been rehabilitated recently in 2017 (Antea Belgium nv, 2017) via the project WACA.

But in terms of rate of changes, few authors investigated erosion rate all along the Benin Republic coast, due to the scarcity of exploitable data over this region. Many of them either investigated only some critical coastal area like South West (Balle et al., 2021; Degbe et al., 2017). Thus, the average erosion on Cell 1 is -2.21 ±3.55 m/year which is slightly different from the results of (Balle et al., 2021) who found an average erosion of -0.75 m/year. At the East side (Cell 2), a rate of -2.17 ± 0.28 m (at the sector of Ganhi) was found and it contrasts with the findings of Degbe et al. (2017), which show that the maximum erosion at the East was -30 ± 0.03 m (at the sector of Ekpe).

3.1.9.5. Trend of the 3 rates

A trend analysis was performed in order to see the general evolution trend of the different rates which were previously computed. This is shown in Figure 40. As it can be seen, EPR, LRR and WLR are following the same trend globally both in erosion (negative values) and accretion (positive values) domains. This same rates trend finding is concordant with (Dey et al., 2021). However, while EPR and LRR are more or less in the same proportion, WLR is changing in a higher proportion. This is explained by the "Weight" applied to this indicator.

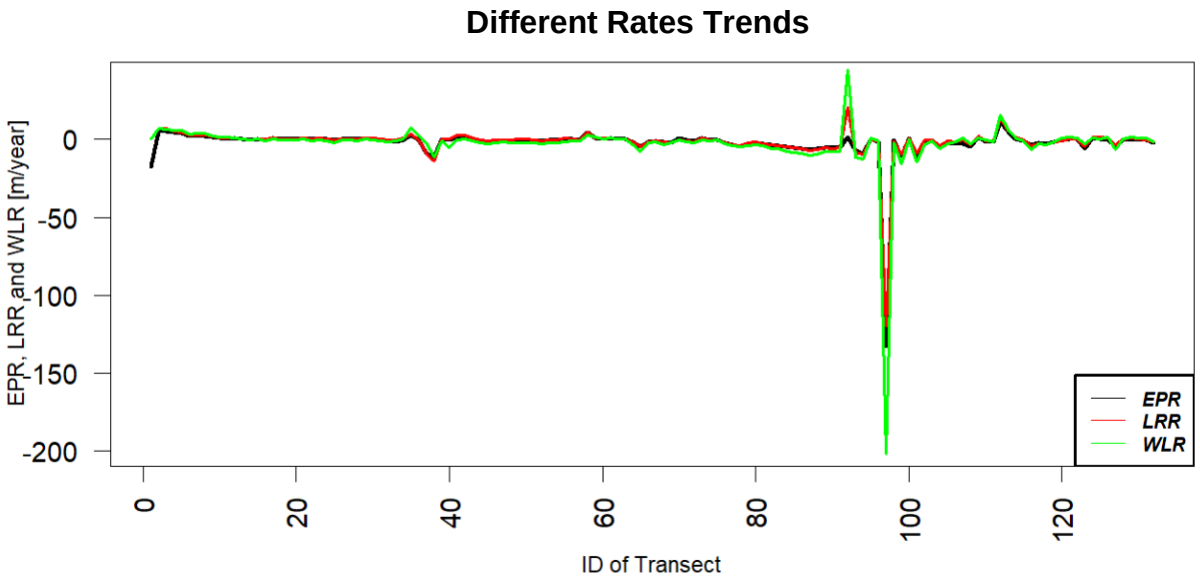

Figure 40: EPR, LRR and WLR trends over the whole study area

3.1.9.6. Uncertainty and accuracy measurement for LRR and WLR

Our methodology to measure the uncertainty and accuracy of LRR and WLR, was based on the one of Dey et al. (2021). As stated previously, the uncertainty value given to DSAS in general is 10m. Then, the r-square statistical method and Standard error method were used to evaluate respectively the accuracy and the error estimation of these two indicators. For the first purpose (accuracy measurement), Linear Regression Rate square (LR2) and Weighted Linear Regression Rate square (WR2) were extracted from the statistical indicators table (Appendix 3). However, for the second purpose (error estimation), Linear Square Error (LSE) and Weighted Linear Square Error (WSE) were extracted from the same table.

04 classes were defined to classify the r-square values in order to finally measure the accuracy of these two indicators computation. Table 10 reports the results of accuracy classification of the transects.

Table 10: LRR and WLR Accuracy assessment

Accuracy Class	R-square values interval	Change Rates indicators Number of Transects (Percentage)	
		LR2	WR2
High accuracy	$r^2 \epsilon$ [0.6; 1]	72 (54.55%)	70 (53.03%)
Moderate accuracy	$r^2 \epsilon$]0.4; 0.6[	13 (9.85%)	16 (12.12%)
Low accuracy	$r^2 \epsilon$]0; 0.4]	33 (25.00%)	31 (23.48%)
No Relationship	$r^2 = 0$	14 (10.60%)	15 (11.37%)

For the LR2 method, ~55% of the LRR transects are measured with a high accuracy while ~11% of them have their value equal to 0. For the WR2 method, ~53% of the transects are measured with a high accuracy and ~11% have their r-square values equal to 0.

3.1.10. Shorelines forecast results analysis

The obtained 10-year and 20-year shorelines vector shapefiles were overlaid on GEE base map. This map is actually the 2022 most recent open georeferenced satellite image available (provided by CNES, Airbus/Landsat, Copernicus/Maxar Technologies). The idea is to identify the regions which are effectively threatened by erosion by 2031 and by 2041 if nothing is done (BaU scenario). Three main regions are identified as potentially highly eroded by the two horizons fixed (Figure 41). The forecast shoreline for 2031 is in green color and the one for 2041 is in red color.

First, the coastal town of Hillacondji is the locality which undergoes the most future erosion (Figure 41.c). The red line is “ahead” of the green one meaning that the erosion is getting worse from 2031 to 2041. The region covered by the erosion is very large (almost all along the coastal town). The maximum erosion is estimated to be 68.11 m (2031) and 182.55 m (2041).

The second coastal town which is projected to experience a very high future erosion is the locality of Avloh plage (Figure 41.b). Here an heterogenous configuration can be observed. The red is “ahead” of the green one in some places, “behind” in some other places and “confused” in some places again. The maximum erosion is estimated to be 226.42 m (2031) and 146.14 m (2041).

The last coastal town which is projected to undergo a high future erosion is the locality of Agblangandan in the department of Littoral (Figure 41.a). At this level, an heterogenous configuration can be also observed. It means that the red line is “ahead” of the green one in some places, “behind” in some other places and “confused” in some places again. The maximum erosion is estimated to be 146.14 m (2031) and 307.30 m (2041).

During our research period, no previous study related to the Benin Republic shoreline forecast could be found. We believe our study will serve as one of the pioneer studies in matter Benin Republic future shorelines forecast.

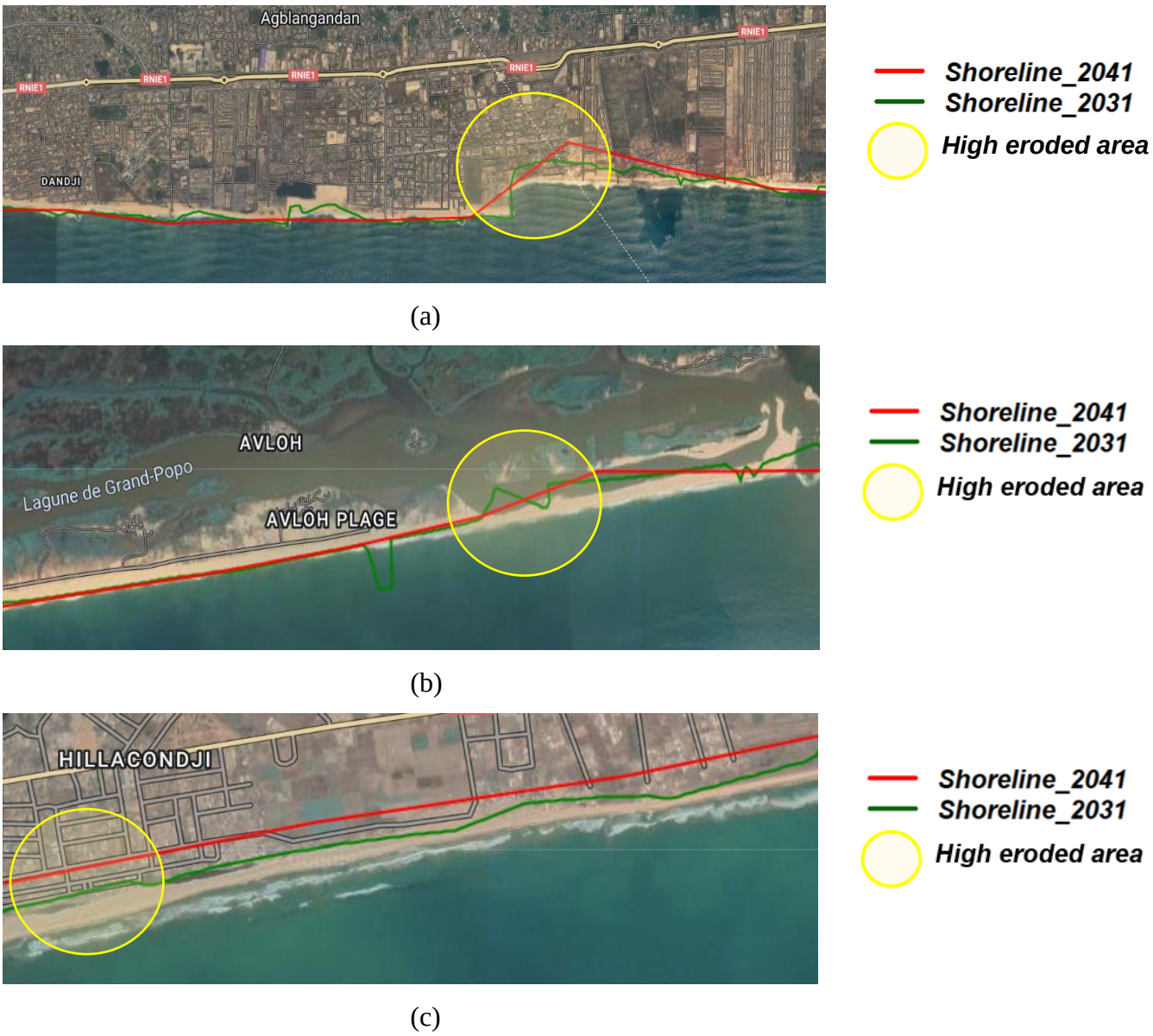

Figure 41: Projected high eroded areas (2031 and 2041)

Conclusion, perspectives and recommendations

Spatiotemporal assessment of shoreline change plays a key role in efforts to build coastal climate resilience. In this study, the combined use of AI and RS allowed us to accurately assess past and projected shoreline dynamics of Benin Republic from 2001 to 2021. The potentiality and the usefulness of satellite geo-spatiotemporal images was demonstrated as an alternative to aerial photographs in scientific studies. 02 supervised image classification algorithms (RF and SVM) were implemented and, based on a comparative analysis of their results, RF emerged the best with better overall accuracies for each of the selected 5 years (Table 5). The RF classified images for the years 2001, 2006, 2012, 2016, and 2021 were used to extract the historical shoreline positions for the respective years. An in-depth multitemporal analysis of these historical data revealed a net erosion trend over the Benin coast. It was found that Sea water (Atlantic Ocean) has moved inland of 169.94 m landward the country during the 20 years study period, at a rate of -2.17 m (EPR) and -1.51 m (LRR). Cumulatively, the shoreline part located before the Port infrastructure was less affected by erosion than the part located after. Therefore, our first hypothesis is confirmed. Then, the shorelines respectively for years 2031 and 2041 were forecasted and revealed complex dynamics (erosion and accretion) all along the Benin coastline. Then, our second hypothesis is confirmed. This projection showed that the localities of Hillacondji, Agblangandan and Avloh plage were expected to be the most vulnerable to coastal erosion under the Business-as-Usual scenario. All the results achieved in this study were compiled in a single source code to be displayed via a free and open access web application to enhance coastal management decision making and climate change impacts education purposes. The easiness in the use of the web application facilitates the communication of our results to decision makers and non-experts. Therefore, our third objective is also confirmed.

Due to the restricted dedicated budget and time constraints, this work has some limitations. First, we could not have access to images from satellites such as SPOT and QuickBird which have very high spatial resolution. This problem, coupled with the problem of persistent thick clouds in the available Landsat images, resulted in classified images with lower accuracies than expected. Second, the study was severely limited by the non-availability of adequate oceanographic data (e.g., sea level, wave, tides) covering the study region over the study period to enable the identification of correlations between the shoreline retreat and the SLR. The third constraint encountered was the non-availability of free and open access satellite data over the study region before the year 2000. As a result, our analysis was limited to the last two decades

with no possibility for extension.

The perspectives from our work are that, in studies that consider coastline changes over the short-term, it is best to use the 10 m resolution Sentinel 2 optical images (from 2015) instead of Landsat images for better accuracy if very high-resolution images are not available. However, for studies that require high temporal accuracy, high-resolution aerial photographs (before the year 2000) is the only available option. Such long-term studies will help to identify the Sea Level critical threshold at which severe erosion impacts were observed.

In the current context of the increase of the occurrences of coastal floods, and coastal erosion events in West Africa, we highly recommend making use of the results and methodologies of this study in the implementation of the Early Warning System to allow decision makers and coastal populations to be aware of the future effects of climate change on coastal zones based on different scenarios. We encourage the use of the web application developed to help in the preservation of biodiversity and socioeconomics activities such as fishery and vegetable gardening from coastal hazards. We also strongly recommend a continuous (monthly) erosion monitoring along the coast of Benin. Concretely, we suggest the installation of tides, sea level, and waves measurements equipments and the acquisition of multispectral drones for a permanent monitoring of the phenomenon.

References

Bibliography

Abdelhady, H. U., Troy, C. D., Habib, A., & Manish, R. (2022). A Simple, Fully Automated Shoreline Detection Algorithm for High-Resolution Multi-Spectral Imagery. *In Remote Sensing* (Vol. 14, Issue 3). https://doi.org/10.3390/rs14030557

Adounkpè, J., Agboton, C., Hounkpatin, W., Kounouhewa, B., Ahouannou, C., & Sinsin, B. (2021). Qualitative Assessment of Table Salt Production Techniques in Southern Benin Republic, and Related Mangrove Destruction and Health Issues. *Food and Nutrition*, *12*, 759–773. https://doi.org/10.4236/fns.2021.127057

Adugna, T., Xu, W., & Fan, J. (2022). Comparison of Random Forest and Support Vector Machine Classifiers for Regional Land Cover Mapping Using Coarse Resolution FY-3C Images. *Remote Sensing*, *14*(3), 1–22. https://doi.org/10.3390/rs14030574

Adjakpa J., Coubeou P., et M. Hagemeier., 1996. Programme d'Aménagement des Zones Humides du sud-Bénin (Ambassade Royale des Pays-Bas à Cotonou): Inventaire de la faune aviaire des zones humides du sud-Bénin, 70 pp.

Aedla, R., Dwarakish, G. S., & Reddy, D. V. (2015). Automatic Shoreline Detection and Change Detection Analysis of Netravati-GurpurRivermouth Using Histogram Equalization and Adaptive Thresholding Techniques. *Aquatic Procedia*, *4*(Icwrcoe), 563–570. https://doi.org/10.1016/j.aqpro.2015.02.073

Alicandro, M., Baiocchi, V., Brigante, R., & Radicioni, F. (2019). Automatic Shoreline Detection from Eight-Band VHR Satellite Imagery. *In Journal of Marine Science and Engineering* (Vol. 7, Issue 12). https://doi.org/10.3390/jmse7120459

Antea Belgium nv. (2017). Plan d ' investissement multisectoriel pour l ' adaptation aux ris ques cotiers face aux changements climatiques au Benin. *Rapport final*. 271. https://documents1.worldbank.org/curated/en/799851527676178019/text/Plan-d-investissement-multisectoriel-pour-l-adaptation-aux-risques-cotiers-face-aux-changements-climatiques-au-Benin.txt

Anthony, G., Greg, H., & Tshilidzi, M. (2007). *Classification of Images Using Support Vector Machines*. http://arxiv.org/abs/0709.3967

Arjasakusuma, S., Kusuma, S. S., Saringatin, S., & Wicaksono, P. (2021). *Shoreline Dynamics*

in East Java Province , Indonesia , from 2000. 1–17.

Aryastana, P., Ardantha, I. M., & Candrayana, K. W. (2018). Coastline change analysis and erosion prediction using satellite images. *MATEC Web of Conferences*, *197*, 1–5. https://doi.org/10.1051/matecconf/201819713003

Assogba L. P . (2018). Étude de la dynamique du trait de côte et des stratégies de gestion du risque d'érosion côtière : cas de Cotonou au Bénin de 1955 à 2018. 1–47.

Balle, G. R. A., Ahouansou, D. M. M., Sintondji, L. C. O., & Agbossou, E. K. (2021). Analyses of short- and long-term shoreline trends of the southwest Benin coast. *Journal of Coastal Research*, 37(2), 316–325. Coconut Creek (Florida), ISSN 0749-0208.

Banno, M., & Kuriyama, Y. (2014). Prediction of Future Shoreline Change With Sea-Level Rise and Wave Climate Change At Hasaki, Japan. *Coastal Engineering Proceedings*, *1*(34), 56. https://doi.org/10.9753/icce.v34.sediment.56

Boak, E. H., & Turner, I. L. (2005). Shoreline definition and detection: A review. *Journal of Coastal Research*, *21*(4), 688–703. https://doi.org/10.2112/03-0071.1

Cazenave, A., & Le Cozannet, G. (2013). Sea level rise and its coastal impacts. *Earth's Future*, *2*, 15–34.

Church, J. A. (2001). Sea level rise: History and consequences. In *Eos, Transactions American Geophysical Union* (Vol. 82, Issue 34). https://doi.org/10.1029/01eo00232

Church, J. A., & Gregory, J. M. (2019). Sea level change. In *Encyclopedia of Ocean Sciences* (pp. 493–499). https://doi.org/10.1016/B978-0-12-409548-9.10820-6

Congalton, R. G. (2015). Remote Sensing and Image Interpretation. 7th Edition. In *Photogrammetric Engineering & Remote Sensing* (Vol. 81, Issue 8). https://doi.org/10.14358/pers.81.8.615

Cracknell, A. P. (1999). Remote sensing techniques in estuaries and coastal zones an update. *International Journal of Remote Sensing*, *20*(3), 485–496. https://doi.org/10.1080/014311699213280

Croitoru, L., Miranda, J. J., & Sarraf, M. (2019). The Cost of Coastal Zone Degradation in West Africa: Benin, Côte D'Ivoire, Senegal and Togo. *World Bank Group*, *March*, 52.

Crowell, M., Douglas, B. C., & Leatherman, S. P. (1997). On forecasting future U.S. Shoreline positions: A test of algorithms. *Journal of Coastal Research*, *13*(4), 1245–1255.

Dadson, I. Y., Owusu, A. B., & Adams, O. (2016). Analysis of Shoreline Change along Cape Coast-Sekondi Coast, Ghana. *Geography Journal*, *2016*, 1–9. https://doi.org/10.1155/2016/1868936

Deabes, E. A. M. (2017). Applying ArcGIS to Estimate the Rates of Shoreline and Back-Shore Area Changes along the Nile Delta Coast, Egypt. *International Journal of Geosciences*, *08*(03), 332–348. https://doi.org/10.4236/ijg.2017.83017

Dey, M., Sakthivel, S. P., & Jena, B. (2021). A Shoreline Change Detection (2012-2021) and forecasting Using Digital Shoreline Analysis System (DSAS) Tool: A Case Study of Dahej Coast, Gulf of Khambhat, Gujarat, India. *Indonesian Journal of Geography*, *53*. https://doi.org/10.22146/ijg.56297

Dolan, R., Fenster, M. S., & Holme, S. J. (1991). Temporal analysis of shoreline recession and accretion. *Journal of Coastal Research*, 7(3), 723–744

Dolan, R., Hayden, B. P., May, P., & May, S. K. (1980). The reliability of shoreline change measurements from aerial photographs. *Shore and Beach*. 48(4), 22–29.

Farr, T. G., Rosen, P. A., Caro, E., Crippen, R., Duren, R., Hensley, S., Kobrick, M., Paller, M., Rodriguez, E., Roth, L., Seal, D., Shaffer, S., Shimada, J., Umland, J., Werner, M., Oskin, M., Burbank, D., & Alsdorf, D. (2007). The Shuttle Radar Topography Mission. *Reviews of Geophysics*, *45*(2). https://doi.org/https://doi.org/10.1029/2005RG000183

Genz, A. S., Fletcher, C. H., Dunn, R. A., Frazer, L. N., & Rooney, J. J. (2007). The Predictive Accuracy of Shoreline Change Rate Methods and Alongshore Beach Variation on Maui, Hawaii. *Journal of Coastal Research*, *23*(1 (231)), 87–105. https://doi.org/10.2112/05-0521.1

Gulácsi, A., & Kovács, F. (2015). Drought Monitoring With Spectral Indices Calculated From MODIS Satellite Images In Hungary. *Journal of Environmental Geography*, *8*, 11–20. https://doi.org/10.1515/jengeo-2015-0008

Hackman, K. O., Gong, P., & Wang, J. (2017). New land-cover maps of Ghana for 2015 using landsat 8 and three popular classifiers for biodiversity assessment. *International Journal of Remote Sensing*, *38*(14), 4008–4021. https://doi.org/10.1080/01431161.2017.1312619

Hilton, D., Davidson, M., & Scott, T. (2020). Seasonal predictions of shoreline change, informed by climate indices. *Journal of Marine Science and Engineering*, *8*(8). https://doi.org/10.3390/JMSE8080616

Himmelstoss, E. A., Henderson, R. E., Kratzmann, M. G., & Farris, A. S. (2021). Digital Shoreline Analysis System (DSAS) Version 5.1 User Guide: U.S. Geological Survey Open-File Report 2021–1091. *U.S. Geological Survey*, 104.

Holman, R., Sallenger, A., Lippmann, T., & Haines, J. (1993). The Application of Video Image Processing to the Study of Nearshore Processes. *Oceanography*, *6*(3), 78–85. https://doi.org/10.5670/oceanog.1993.02

Institut National de la Statistique et de l'Analyse Économique (INSAE). 2019. Enquête Démographique et de Santé au Bénin, 2017-2018. *Cotonou, Bénin et Rockville, Maryland, USA* : INSAE et ICF.

IPCC, 2018: Annex I: Glossary [Matthews, J.B.R. (ed.)]. In: Global Warming of 1.5°C. An IPCC Special Report on the impacts of global warming of 1.5°C above pre-industrial levels and related global greenhouse gas emission pathways, in the context of strengthening the global response to the threat of climate change, sustainable development, and efforts to eradicate poverty [Masson-Delmotte, V., P. Zhai, H.-O. Pörtner, D. Roberts, J. Skea, P.R. Shukla, A. Pirani, W. Moufouma-Okia, C. Péan, R. Pidcock, S. Connors, J.B.R. Matthews, Y. Chen, X. Zhou, M.I. Gomis, E. Lonnoy, T. Maycock, M. Tignor, and T. Waterfield (eds.)]. Cambridge University Press, Cambridge, UK and New York, NY, USA, pp. 541-562, doi:10.1017/9781009157940.008.

Leatherman, S., Zhang, K., & Douglas, B. (2000). Sea level rise shown to drive coastal erosion. *EOS Transactions*, *81*, 55–57. https://doi.org/10.1029/00EO00034

Lillesand, T. M., Kiefer, R. W., & Chipman, J. W. (2004). *Remote Sensing and Image Interpretation*. Wiley. https://books.google.bf/books?id=XiydAAAAMAAJ

Liu, Q., Trinder, J., & Turner, I. L. (2017). Automatic super-resolution shoreline change monitoring using Landsat archival data: a case study at Narrabeen–Collaroy Beach, Australia. *Journal of Applied Remote Sensing*, *11*(1), 016036. https://doi.org/10.1117/1.jrs.11.016036

Long, J., & Plant, N. G. (2012). Extended Kalman Filter framework for forecasting shoreline evolution. *Geophysical Research Letters*, *39*(13). https://doi.org/10.1029/2012GL052180

Luijendijk, A., Hagenaars, G., Ranasinghe, R., Baart, F., Donchyts, G., & Aarninkhof, S. (2018). The State of the World's Beaches. *Scientific Reports*, *8*(1), 1–11. https://doi.org/10.1038/s41598-018-24630-6

McCarthy, J. (1989). Artificial Intelligence, Logic and Formalizing Common Sense. *Philosophical Logic and Artificial Intelligence*, 161–190. https://doi.org/10.1007/978-94-009-2448-2_6

McGuire, C. J. (2017). Adapting to sea level rise in the coastal zone: Law and policy considerations. In *Adapting to Sea Level Rise in the Coastal Zone: Law and Policy Considerations*. https://doi.org/10.4324/9781315097572

Morton, R. A. (1991). *Accurate Shoreline Mapping: Past, Present, and Future*.

Nerem, R. S., Beckley, B. D., Fasullo, J. T., Hamlington, B. D., Masters, D., & Mitchum, G. T. (2018). Climate-change–driven accelerated sea-level rise detected in the altimeter era. *Proceedings of the National Academy of Sciences of the United States of America*, *115*(9), 2022–2025. https://doi.org/10.1073/pnas.1717312115

Njutapvoui, N., Onguene, R., & Rudant, J. P. (2022). Evaluation du potentiel des series d'images multi-temporelles optique et radar des satellites SENTINEL 1 & 2 pour le suivi d'une zone côtière en contexte tropical: cas de l'estuaire du Cameroun pour la période 2015-2020. *Revue Française de Photogrammétrie et de Télédétection*, 223, 88–103. https://doi.org/10.52638/rfpt.2021.586

Ozer, P., Hountondji, Y.-C., & De Longueville, F. (2017). Recent evolution of the coastline in the bight of Benin. Example of Togo and Benin | Evolution récente du trait de côte dans le golfe du Bénin. Exemples du Togo et du Bénin. *Geo-Eco-Trop*, *41*(3), 529–541.

Patil, R. G., & Deo, M. C. (2020). Sea Level Rise and Shoreline Change under Changing Climate Along the Indian Coastline. *Journal of Waterway, Port, Coastal, and Ocean Engineering*, *146*(5), 05020002. https://doi.org/10.1061/(asce)ww.1943-5460.0000586

Pouye, I., Adjoussi, D. P., Ndione, J. A., Sall, A., Adjaho, K. D., Leroy, M., & Gomez, A. (2022). *Coastline Dynamics Analysis in Dakar Region , Senegal from 1990 to 2040*. 23–36. https://doi.org/10.4236/ajcc.2022.112002

Reddy, R. V. K., & Babu, U. R. (2018). A Review on Classification Techniques in Machine Learning. *International Journal of Advance Research in Science and Engineering*, *7*(30), 40–47. http://www.ijarse.com/images/fullpdf/1521195654_Vedant612ijarse.pdf

Richards, J. A., & Jia, X. (1999). Remote Sensing Digital Image Analysis. In *Remote Sensing Digital Image Analysis*. https://doi.org/10.1007/978-3-662-03978-6

Sarr, B., Ly, M., Salack, S., & Agali, A. (2015). Atlas agroclimatique sur la variabilité et le changement climatique au Benin. 1–37.

Sheykhmousa, M., Mahdianpari, M., Ghanbari, H., Mohammadimanesh, F., Ghamisi, P., & Homayouni, S. (2020). Support Vector Machine Versus Random Forest for Remote Sensing Image Classification: A Meta-Analysis and Systematic Review. *IEEE Journal of Selected Topics in Applied Earth Observations and Remote Sensing*, *13*, 6308–6325. https://doi.org/10.1109/JSTARS.2020.3026724

Stockdon, H. F., Sallenger, A. H., List, J. H., & Holman, R. A. (2002). Estimation of shoreline position and change using airborne topographic lidar data. *Journal of Coastal Research*, *18*(3), 502–513.

Tossou, M. G., Akoègninou, A., Ballouche, A., Sowunmi, M. A., & Akpagana, K. (2008). The history of the mangrove vegetation in Bénin during the Holocene: A palynological study. *Journal of African Earth Sciences*, *52*(4–5), 167–174. https://doi.org/10.1016/j.jafrearsci.2008.07.007

Toure, S., Diop, O., Kpalma, K., & Amadou, S. M. (2019). Shoreline Detection using Optical Remote Sensing: A Review. ISPRS *International Journal of Geo-Information*, 8, 75. https://doi.org/10.3390/ijgi8020075

Tsyban, A., Everett, J., Titus, J., Agnew, T., Berry, M., Chernyak, S., Etkin, D., Glantz, M., Glebov, B., Griffiths, C., Kaplin, P., Krovnin, A., Laroe, E., Lukin, A., Meehan, J., Nishioka, S., Pershina, I., Rees, M., Rodionov, S., … Zeeman, S. (1990). IPCC: Chapter 6 World oceans and coastal zones. *Climate Change: The IPCC Impacts Assessment*. http://www.ipcc.ch/ipccreports/far/wg_II/ipcc_far_wg_II_chapter_06.pdf

Vassilakis, E., Tsokos, A., & Kotsi, E. (2017). Shoreline Change Detection and Coastal Erosion Monitoring Using Digital Processing of a Time Series of High Spatial Resolution Remote Sensing Data. *Bulletin of the Geological Society of Greece*, *50*(3), 1747. https://doi.org/10.12681/bgsg.11898

Vousdoukas, M. I., Ranasinghe, R., Mentaschi, L., Plomaritis, T. A., Athanasiou, P., Luijendijk, A., & Feyen, L. (2020). Sandy coastlines under threat of erosion. *Nature Climate Change*, *10*(3), 260–263. https://doi.org/10.1038/s41558-020-0697-0

Watik, N., & Jaelani, L. (2019). Flood evacuation routes mapping based on derived- flood impact analysis from landsat 8 imagery using network analyst method. *Isprs* -

International Archives of the Photogrammetry, Remote Sensing and Spatial Information Sciences, *XLII-3/W8*, 455–460. https://doi.org/10.5194/isprs-archives-XLII-3-W8-455-2019

Worden, J., & de Beurs, K. M. (2020). Surface water detection in the Caucasus. *International Journal of Applied Earth Observation and Geoinformation*, *91*, 102159. https://doi.org/https://doi.org/10.1016/j.jag.2020.102159

Ya'acob, N., Azize, A., Mahmon, N., Yusof, A., Azmi, N., & Mustafa, N. (2014). Temporal Forest Change Detection and Forest Health Assessment using Remote Sensing. *IOP Conference Series: Earth and Environmental Science*, *19*. https://doi.org/10.1088/1755-1315/19/1/012017

Yang, C. S., Shin, D. W., Kim, M. J., Choi, W. J., & Jeon, H. K. (2021). Shoreline changes and erosion protection effects in Cotonou of Benin in the Gulf of Guinea. *Korean Journal of Remote Sensing*, *37*(4), 803–813. https://doi.org/10.7780/kjrs.2021.37.4.10

Theses (master or doctoral)

Aarninkhof, S. J. C. (2003). Nearshore bathymetry derived from video imagery. *PhD thesis*. Delft University of Technology (Faculty of Civil Engineering and Geosciences). DUP Science. ISBN 90-407-2439-3.

Assogba, L.P. (2018). Étude de la dynamique du trait de côte et des stratégies de gestion du risque d'érosion côtière : cas de Cotonou au Bénin de 1955 à 2018. *Master thesis*. University of Liege (Science faculty). Belgium. 1 - 47.

Badji, O. (2021). Assessment of the impacts of climate change on the Grand Saloum transboundary Wetland Complex (Senegal-Gambia). *Master thesis.* Universidade técnica do atlântico (Instituto de engenharia e ciências do mar). Cape Verde. 1 - 35.

Degbe, C. G. E. (2017). Analyse de la dynamique du trait de côte du littoral béninois de 1984 à 2014. *PhD thesis*. University of Abomey-Calavi (International Chair in Mathematical Physics and Applications). Benin. 1 - 117.

Faye, I. B. N. (2010). Dynamique du trait de côte sur les littoraux sableux de la Mauritanie à la Guinée-Bissau (Afrique de l'Ouest) : Approches régionale et locale par photo-interprétation, traitement d'images et analyse de cartes anciennes (Volume 1). *PhD thesis.* University of Western Brittany (Doctoral School of Marine Sciences). France. 1 – 315.

Web sites

Author	URL	Consulted on
Humboldt-Universität zu Berlin. Department of Geography	https://pages.cms.hu-berlin.de/EOL/geo_rs/S09_Image_classification2.html	04/06/2022
International Business Machines (IBM)	https://www.ibm.com/topics/computer-vision	02/10/2022
Ronald van Loon	https://bigdata-madesimple.com/machine-learning-explained-understanding-supervised-unsupervised-and-reinforcement-learning/	04/06/2022
World Bank	https://www.worldbank.org/en/results/2017/12/01/resilient-coasts	03/18/2022

Appendices

Appendix 1: URL link towards the project source code

https://code.earthengine.google.com/?scriptPath=users%2Fdavid91%2FICC_THESIS%3ALUC_Cotonou

Appendix 2: URL link towards the GEE Web Application

https://david91.users.earthengine.app/view/benshoreapp

Appendix 3: DSAS statistical indicators table

Table 11: Complete table of DSAS statistical indicators

TransectID	EPR	LRR	WLR	NSM	LR2	LSE	WR2	WSE
1	-17.40	0.00	0.00	-104.40	0.52	790.77	0.71	376.37
2	5.40	6.99	7.10	81.07	0.54	127.00	0.73	57.80
3	5.10	6.71	6.27	76.46	0.05	68.90	0.23	30.27
4	4.33	5.45	6.09	64.96	0.53	62.19	0.72	29.51
5	3.82	4.41	5.80	57.34	0.05	70.35	0.22	29.35
6	2.30	2.83	3.59	34.45	0.52	51.79	0.71	16.82
7	2.45	2.92	4.12	36.80	0.52	55.64	0.69	17.68
8	2.11	2.49	3.75	31.65	0.00	0.00	0.00	0.00
9	1.57	1.95	2.33	23.53	0.48	48.26	0.65	16.25
10	0.77	1.02	1.48	11.55	0.47	30.07	0.64	11.89
11	0.43	0.82	1.20	6.38	0.49	44.81	0.65	15.06
12	0.71	0.86	1.14	10.58	0.71	42.05	0.86	13.36
13	0.28	0.47	0.42	4.22	0.51	30.40	0.67	9.73
14	-0.26	-0.13	-0.28	-3.86	0.46	30.95	0.64	12.12
15	0.40	0.46	0.04	5.96	0.56	41.35	0.75	18.72
16	-0.24	0.01	-1.11	-3.65	0.51	30.89	0.67	10.05
17	0.88	0.89	0.05	13.25	0.49	34.08	0.65	11.57
18	0.00	-0.04	-0.15	-0.06	0.27	32.16	0.38	13.41
19	0.28	0.17	-0.08	4.14	0.44	34.45	0.62	13.29
20	0.39	0.34	-0.20	5.85	0.58	40.63	0.77	13.97
21	0.50	0.55	0.05	7.48	0.41	8.34	0.52	4.22
22	0.14	0.24	-0.87	2.06	0.80	27.57	0.88	14.09
23	0.39	0.58	-0.62	5.87	0.44	23.00	0.60	9.16
24	-0.06	0.11	-1.19	-0.83	0.40	3.61	0.50	1.74
25	-0.52	-0.34	-2.14	-7.75	0.66	31.72	0.82	10.80
26	0.32	0.52	-0.39	4.79	0.43	23.73	0.60	11.62
27	0.28	0.31	-0.55	4.15	0.43	16.47	0.58	7.80
28	0.12	0.35	-0.69	1.80	0.67	16.83	0.83	5.52
29	0.48	0.62	0.01	7.13	0.58	85.10	0.76	29.89
30	0.41	0.64	-0.30	6.21	0.42	16.06	0.53	8.10
31	-0.22	0.06	-0.70	-3.34	0.57	24.07	0.76	9.05

32	-1.10	-0.63	-1.31	-16.53	0.39	5.86	0.50	2.49
33	-1.38	-0.65	-1.15	-20.74	0.66	10.90	0.82	3.73
34	-0.36	0.66	0.41	-5.43	0.56	35.01	0.75	16.29
35	2.85	3.18	7.34	42.82	0.98	14.62	0.98	5.31
36	-0.14	-0.36	2.59	-2.08	0.32	12.21	0.41	5.12
37	-8.86	-9.24	-2.39	-132.96	0.43	18.05	0.56	8.92
38	-11.27	-13.65	-11.19	-169.02	0.25	18.43	0.37	7.02
39	0.34	-0.02	-1.10	5.09	0.07	23.95	0.26	12.19
40	-0.31	0.11	-5.09	-4.67	0.31	20.48	0.41	9.12
41	1.35	2.53	-0.44	20.30	0.52	9.41	0.71	3.30
42	2.12	2.76	0.40	31.81	0.60	30.10	0.79	13.43
43	-0.19	0.89	-0.88	-2.78	0.69	6.05	0.83	2.28
44	-1.05	-0.23	-2.17	-15.72	0.59	28.99	0.78	10.39
45	-1.85	-1.08	-3.03	-27.68	0.28	7.69	0.38	2.46
46	-1.07	-0.48	-2.25	-16.07	0.04	21.67	0.19	8.99
47	-0.74	-0.17	-1.72	-11.13	0.54	29.99	0.73	15.32
48	-1.10	-0.48	-2.19	-16.45	0.36	15.05	0.43	4.80
49	-0.53	0.07	-2.07	-7.99	0.04	13.63	0.18	6.34
50	-0.48	0.35	-2.09	-7.25	0.11	19.96	0.28	10.21
51	-0.79	-0.34	-2.25	-11.82	0.08	19.83	0.27	10.17
52	-0.90	-0.77	-3.14	-13.52	0.07	25.02	0.26	12.64
53	-0.40	-0.12	-1.97	-5.95	0.28	7.72	0.38	2.70
54	-0.46	-0.24	-2.34	-6.93	0.12	24.37	0.31	10.14
55	0.33	0.59	-1.42	4.94	0.66	13.87	0.82	5.80
56	0.29	0.48	-0.99	4.42	0.11	19.12	0.30	9.62
57	-0.36	-0.13	-1.03	-5.39	0.11	18.36	0.27	9.38
58	4.47	4.40	2.95	67.04	0.53	27.89	0.72	8.97
59	0.88	1.12	1.24	13.22	0.35	14.64	0.42	4.66
60	0.43	0.59	0.11	6.46	0.38	7.38	0.45	2.46
61	1.08	1.07	0.68	16.26	0.70	13.70	0.84	6.27
62	0.34	0.29	0.27	5.05	0.11	22.47	0.28	11.49
63	0.45	0.50	0.02	6.81	0.02	17.85	0.12	7.89
64	-1.88	-1.90	-3.55	-28.17	0.11	27.76	0.29	14.23
65	-4.64	-4.47	-7.60	-69.62	0.13	20.70	0.32	9.26
66	-1.56	-1.69	-2.13	-23.41	0.13	18.02	0.32	8.50
67	-1.03	-1.08	-1.69	-15.38	0.54	6.23	0.74	3.18
68	-1.82	-1.60	-3.68	-27.27	0.05	31.92	0.20	12.31
69	-1.98	-2.39	-2.08	-29.67	0.17	9.18	0.33	4.67
70	0.56	-0.10	-0.31	8.38	0.06	52.16	0.24	22.53
71	-0.62	-0.92	-1.57	-9.23	0.94	12.86	0.96	4.17
72	-1.26	-1.51	-2.36	-18.88	0.00	3.65	0.02	1.64
73	1.15	0.90	-0.42	17.32	0.01	11.03	0.04	5.52
74	-0.56	-0.64	-1.16	-8.34	0.94	16.83	0.94	5.38
75	-0.17	-0.17	-0.20	-2.55	0.04	9.12	0.17	4.66
76	-2.51	-2.47	-3.05	-37.71	0.07	30.94	0.26	14.77
77	-3.71	-3.65	-4.02	-55.64	0.85	7.37	0.89	2.47

78	-4.39	-4.12	-4.77	-65.89	0.39	0.32	0.48	0.14
79	-2.59	-2.20	-3.80	-38.82	0.05	29.71	0.20	12.71
80	-1.97	-1.60	-3.44	-29.62	0.78	36.89	0.88	12.82
81	-2.85	-2.59	-4.29	-42.78	0.70	17.46	0.84	5.85
82	-3.68	-3.22	-5.65	-55.25	0.02	12.67	0.08	5.81
83	-4.03	-3.99	-6.14	-60.51	0.01	2.12	0.04	0.67
84	-4.64	-4.65	-7.77	-69.62	0.52	16.04	0.71	5.19
85	-5.45	-5.42	-8.27	-81.69	0.03	10.28	0.15	5.14
86	-5.96	-5.91	-8.71	-89.33	0.02	11.05	0.07	4.85
87	-6.49	-6.99	-10.50	-97.40	0.01	5.35	0.04	1.70
88	-5.83	-6.30	-9.54	-87.46	0.03	8.97	0.13	3.66
89	-5.10	-5.43	-7.95	-76.52	0.00	5.94	0.02	2.31
90	-5.58	-6.07	-7.83	-83.70	0.15	14.38	0.32	6.60
91	-5.12	-5.54	-7.54	-76.83	0.91	17.48	0.93	5.57
92	1.76	20.38	44.53	26.45	0.03	9.01	0.12	4.50
93	-7.38	-8.43	-11.24	-110.77	0.14	19.56	0.32	8.99
94	-8.70	-9.42	-12.74	-130.52	0.22	1.62	0.36	0.56
95	0.09	0.46	1.02	1.33	0.06	20.16	0.24	6.42
96	-1.77	-1.70	-0.95	-26.49	0.70	7.37	0.86	2.96
97	-133.15	-120.06	-201.65	-1997.23	0.65	31.67	0.81	12.80
98	-0.64	-1.27	-2.32	-9.63	0.01	6.86	0.05	2.40
99	-10.67	-9.66	-16.07	-160.00	0.02	11.63	0.07	5.53
100	1.05	1.00	0.46	15.76	0.01	4.09	0.03	1.93
101	-13.33	-8.91	-14.52	-199.94	0.04	9.50	0.16	4.80
102	-1.37	-0.57	-3.45	-20.51	0.00	15.30	0.02	5.10
103	-0.37	-0.20	-0.80	-5.51	0.19	5.46	0.35	2.80
104	-5.32	-3.88	-5.65	-79.74	0.23	4.74	0.36	2.07
105	-2.15	-0.93	-2.67	-32.22	0.03	6.10	0.16	3.08
106	-2.54	-1.79	-1.85	-38.10	0.02	4.99	0.07	2.23
107	-2.68	-0.25	0.80	-40.16	0.77	20.41	0.86	9.10
108	-4.41	-3.29	-2.59	-66.08	0.33	22.57	0.41	8.03
109	1.49	2.14	0.63	22.40	0.00	6.95	0.02	2.22
110	-1.60	-0.75	-0.52	-24.07	0.00	11.36	0.01	3.63
111	-1.76	-0.71	-1.90	-26.34	0.74	12.94	0.86	5.85
112	11.14	14.09	15.79	167.05	0.19	8.33	0.35	2.89
113	4.89	5.97	6.62	73.37	0.01	9.18	0.04	3.60
114	0.37	1.41	0.86	5.51	0.53	6.84	0.73	2.40
115	-0.87	-0.40	-0.75	-13.09	0.22	4.47	0.36	1.68
116	-3.69	-3.98	-6.35	-55.29	0.38	19.79	0.43	6.49
117	-2.28	-2.58	-2.78	-34.23	0.06	36.74	0.25	18.68
118	-2.81	-3.22	-3.73	-42.15	0.59	19.81	0.77	9.99
119	-1.69	-1.88	-1.86	-25.32	0.00	14.76	0.01	4.91
120	-0.54	-0.72	0.69	-8.10	0.51	767.26	0.68	250.61
121	-0.07	0.12	1.37	-1.04	0.00	22.49	0.01	7.18
122	0.36	0.34	1.04	5.44	0.06	24.45	0.25	12.47
123	-5.75	-4.96	-2.84	-86.22	0.00	22.55	0.00	7.32

124	0.87	1.32	0.77	13.01	0.00	24.27	0.01	7.71
125	0.51	1.21	0.41	7.60	0.05	51.55	0.20	18.25
126	-0.09	0.95	1.49	-1.34	0.00	29.60	0.00	9.41
127	-4.35	-3.61	-6.25	-65.26	0.00	40.16	0.00	13.87
128	-0.17	0.02	0.20	-2.59	0.18	17.14	0.34	6.24
129	0.31	0.67	1.44	4.62	0.64	39.05	0.81	13.47
130	-0.23	0.04	1.01	-3.48	0.00	50.46	0.00	19.57
131	-0.29	-0.11	0.71	-4.31	0.00	52.26	0.00	19.23
132	-2.10	-1.67	-1.60	-31.56	0.60	106.17	0.79	36.68

Appendix 4: Computation of the slope in a digital image

https://pro.arcgis.com/en/pro-app/latest/tool-reference/3d-analyst/how-slope-works.htm

Appendix 5: Unsupervised Learning

It is required when there is no example data set with known answers. For example, searching for a hidden pattern. In this case, clustering i.e. dividing a set of elements into groups according to some unknown pattern is carried out based on the existing data sets present.

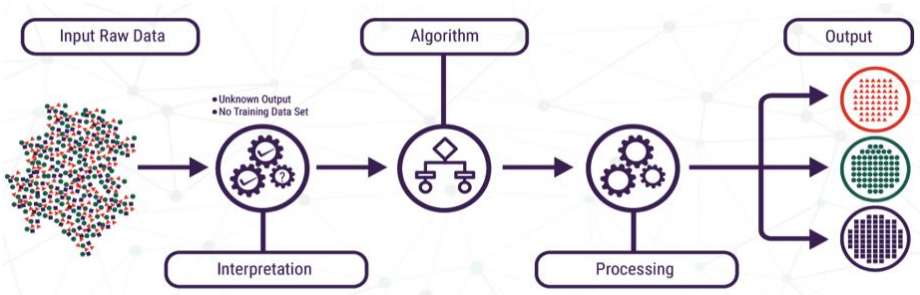

Figure 42: Unsupervised Learning illustration
Source: Van Loon, 2018

Appendix 6: Reinforcement Learning

This strategy built on observation. The ANN decides by observing its environment. If the observation is negative, the network adjusts its weights to be able to make a different required decision the next time.

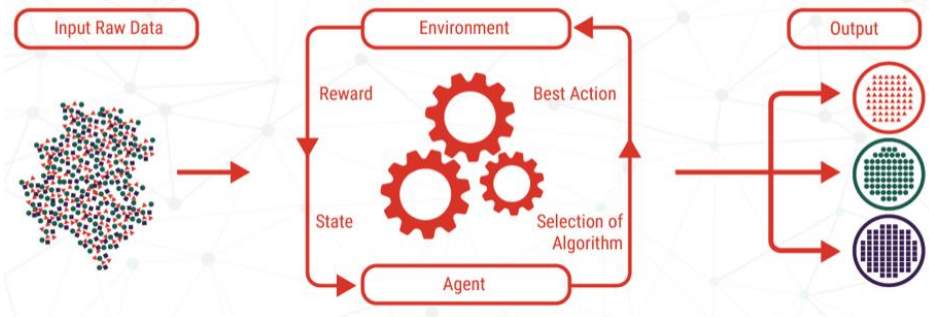

Figure 43: Reinforcement Learning illustration
Source: Van Loon, 2018

Table of Contents